Geofísica Internacional

Revista Trimestral Publicada por el Instituto de Geofísica de la
Universidad Nacional Autónoma de México

— Geofísica Internacional —

Contents

Geological Differentiation of Groundwater Threshold Concentrations of Arsenic, Vanadium and Fluorine in El Bajio Guanajuatense, Mexico

Ramiro Rodríguez[*†], Iván Morales-Arredondo and Isaías Rodríguez

Resumen

Los valores de fondo del agua subterránea, BGV (por sus siglas en ingles), de elementos riesgosos, pueden ser integrados como componentes en las políticas de manejo del agua subterránea. Variaciones de los BGV en áreas rurales con actividad agrícola y en áreas urbanas con desarrollo industrial pueden ser referidas a procesos de contaminación del agua. Métodos para calcular los BGV fueron aplicados en una comunidad agrícola en el centro de México. Un tratamiento estadístico para rechazar valores anómalos fue usado (Prueba de Dixon). Los valores de fondo fueron calculados usando el método de Grubb. Variaciones en los valores de fondo de arsénico y vanadio son explicados en términos de fuentes potenciales de contaminación y mecanismos de migración. El arsénico y el vanadio estaban contenidos en particulado emitido por una planta termoeléctrica. El particulado fue depositado sobre áreas vulnerables lo que facilitó su migración hacia acuíferos someros locales. Diferencia en los valores de fondo de fluoruros son explicados en términos del marco geológico.

Palabras clave: arsénico, valores de fondo, El Bajío México, fluoruros, agua subterránea.

Abstract

Groundwater background values, (GBV), of risky elements can be integrated as a component in groundwater management policies. Variations of GBV in rural areas with agricultural activity and in urban areas with industrial development can be related to contamination processes. Methods to calculate GBV were applied in Salamanca and Juventino Rosas, an industrial city and a farming community located in Central Mexico. A statistical treatment for rejection of deviant values was used for outliers (Dixon's Q test). GBV were calculated using the Grubb test. Variations in arsenic and vanadium GBV are explained in terms of potential contamination sources and migration mechanisms. Arsenic and vanadium are contained in particulate emitted by a thermoelectric plant. Particulate was deposited over vulnerable areas that facilitate its migration to local aquifers. Differences in fluoride GBV are explained in terms of the geological framework.

Key words: arsenic, background values, El Bajio Mexico, fluorine, groundwater.

R. Rodríguez[*]
I. Rodríguez
Instituto de Geofísica
Universidad Nacional Autónoma de México
Circuito de la Investigación Científica s/n
Ciudad Universitaria
Delegación Coyoacán, 04510
México D.F., México
*Corresponding autor: ramiro@geofisica.unam.mx
          negusa_negast@yahoo.com.mx

I. Morales-Arredondo
Programa de Posgrado en Ciencias de la Tierra
Universidad Nacional Autónoma de México

Introduction

In areas with potential sources of contamination and crossed processes of soil and groundwater contamination, it is necessary to implement planning and management tools that allow sustainable policies of exploitation water resources. If there are not surface water bodies and agriculture and industrial processes require great volumes of water, groundwater becomes a valuable resource.

In Guanajuato State, Central Mexico aquifer vulnerability assessments were promoted as additional criterion to prevent and/or to avoid groundwater quality alterations because groundwater is the only source of urban and rural water supply of many cities, like Juventino Rosas and Salamanca, an important industrial centre (SEMARNAT 2013) (Figure 1). Guanajuato is the only Mexican State with vulnerability assessments, mathematical flow models and monitoring well networks in each regional aquifer (Marañón 2010).

Salamanca uses only groundwater for all uses. There is an industrial zone; a refinery, a thermoelectric plant and until 2008 an agrochemical plant that produced DDT generated contaminants (Rodríguez *et al.*, 2000; Rodríguez *et al.*, 2001; Rodríguez *et al.*, 2002). In Salamanca, arsenic, (As), and vanadium, (V), concentrations from natural origin and locally from anthropogenic origin have been reported in the local aquifer system (Rodriguez *et al.*, 2000; Rodriguez *et al.*, 2001; Rodriguez *et al.*, 2015). Vanadium does not represent considerable environmental concern. In the study area groundwater V is originated by infiltrations that carry V contained in particulate emitted by industries using fuel oil number 6 (locally called combustoleo), when the electrostatic precipitators do not work. This fuel has high vanadium contents of 290 to 500 ppm (Salinas *et al.*, 2001). Late 2004, particulate emissions deposited on soils were analyzed. High V concentrations were detected, 2.09 g/Kg (LAQUIMIA 2004). During combustoleo combustion V is released to the atmosphere as V_2O_5 in fine ashes suspended in the air. The V content in these emissions varies from 1 to 18 % (WHO 2000). Other authors have measured similar values (Mendoza 1999; Mata, 206; Hernandez *et al.*, 2007). Particulate is deposited over vulnerable areas and then migrates to the shallow aquifer (Mejía *et al.*, 2007).

In Salamanca, the intense extraction regime results in subsidence, being its mean velocity 6-7 cm/year (Rodríguez *et al.*, 2002). The subsidence produces two faults; one of them crosses the urban area and refinery lands affecting the urban infrastructure (Rodríguez and Rodríguez, 2006). The faults can facilitate the migration of surface contaminants.

In Juventino Rosas, an agricultural community with some additional incomes from goat cheese production, high concentrations of arsenic and fluorine has been detected in the regional aquifer (Rodriguez *et al.*, 2001; Mendoza 1999). Vanadium concentrations are lower than the detection limit. The origin of them is geogenic and related to the geological framework and to the geothermal activity observed in some parts of the aquifer (Morales *et al.*, 2015). Groundwater temperature varies from 25.5°C to 50°C. The highest temperatures are located near faults and fractures. High temperatures match with the highest groundwater concentrations of As and F concentrations. In hydrothermal systems the solubility of some minerals increases (Eugster, 1986).

The main environmental risks associated to arsenic and fluorides are health affectations of the exposed population. The more risky exposition route is water ingestion, even more than ingestion of food with higher As and F concentrations. Arsenic health affectations include skin alterations, cardiovascular problems and cancer in different organs, and for fluoride, dental fluorosis and/or skeletal fluorosis.

The origin of some risky elements can be proposed through the knowledge of local and regional groundwater background values, GBV (Reimann and Garret 2005). Concentrations in pristine areas can define the natural, geogenic levels of some element while higher concentrations could be related to anthropogenic interventions. Anomalous concentrations allow the identification of potential contaminant sources and even contaminant migration mechanisms. The determination of GBV in Salamanca can help to define the extension of the zones affected by anthropogenic contamination sources like particulate and/or to know when an urban well is being contaminated. In Juventino Rosas GBV can be used to define if falls are contributing with ascendant flows rich in elements like arsenic altering the local hydrochemistry, as occurred in Rancho Nuevo, Apaseo El Alto, no far away from J. Rosas where suddenly appears a geothermal manifestation with water rich in arsenic and temperature greater than 65° C.
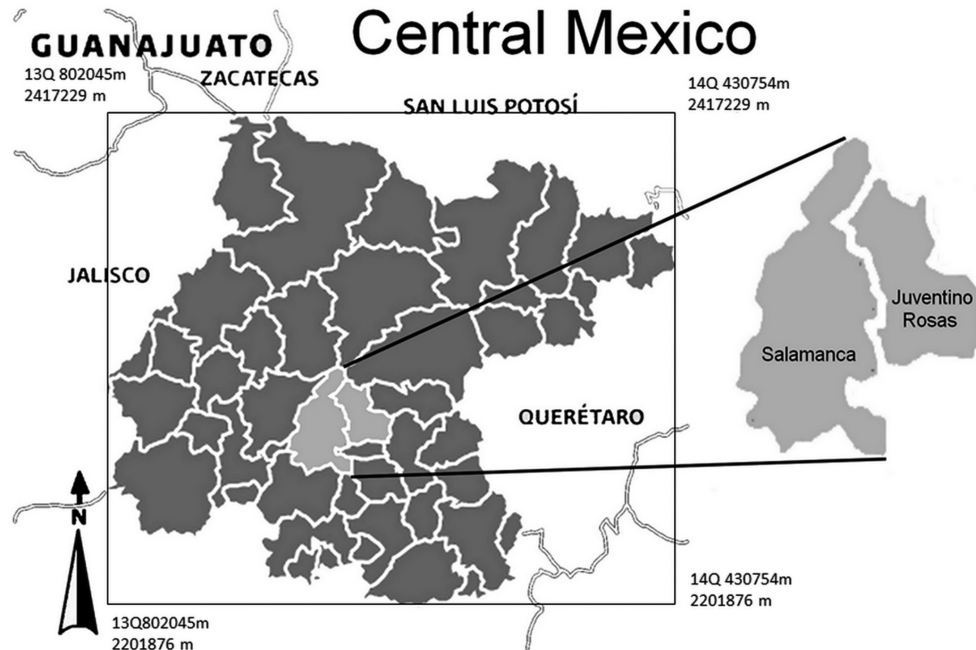
Figure 1. Localization.

Two tectonic events affected the whole area. The first one is related to the Laramide Orogeny, whereas the second was an extensional phase with intense magmatism (Ferrari 2000; Cerca-Martínez *et al*., 2000). Both events originated faults and fractures in the area. These faults allow ascendant geothermal flow that can contain elements like fluorine, lithium and radon (Morales *et al*., 2015; Rodríguez *et al*., 2015). In Guadalupe, a neighborhood located 4 km SW of J. Rosas, there are subsidence manifestations. A subsidence fault due to the abstraction of a local well produced a differential terrain displacement of 3.6 m in 6 years, one of the highest in Central Mexico (Rodríguez *et al*., 2002).

Methodology

A monitoring sampling was carried out in both study areas, Salamanca and Juventino Rosas. In Salamanca groundwater samplings were carried out in Jul 2003, Feb 2004, Jun 2004 , Apr 2005, Aug 2005, Nov 2005, Aug 2006 and Sep 2006. In J. Rosas sampling were collected in May 2010, August, 2011, October 2012, March 2013 and June 2013. Samples were collected as described by Mexican standard (NMX-AA-132-SCFI-2006). Groundwater samples were analyzed in the Chemical Analytical lab of the Geophysics Institute of the National University of Mexico, UNAM. Formal EPA and CNA (Mexican National Commission of Water) protocols for sampling and analytical procedures were applied (APHA-AWWA, 2005). Arsenic was measured by atomic absorption spectrometry with hydride generation, Fluorine by potentiometry with selective electrods and vanadium was analyzed in the water colorimetrically by measuring the extent of oxidation of gallic acid (APHA, 1995).

Twenty five urban wells were monitored in Salamanca, white 23 were sampled in Juventino Rosas. For the purpose of this research only As, F, and V were considered. The use of other hydrochemical methods or graphic information as Piper, Schoeller or Stiff diagrams do not contribute in the definition of GBV.

Evaluation of a single aberrant or inconsistent value using Dixon and Grubb test Dixon's Q test for the rejection of outlier values

A test for outliers of normally distributed data which is particularly simple to apply has been developed by Dixon (1951). This test is eminently suitable for small sample sizes; for samples having more than 30 data the test for significance of Pearson and Hartley can be used as well. In order to perform the Dean-Dixon test for outliers, the data set containing N values has to be sorted either in an ascending or descending order, with x1 being the suspect value. Then the test statistic Q is calculated using the equation.

$$Q= |X2\text{-}X1|/|Xn\text{-}X1| \qquad (1)$$

The decision whether x1 is an outlier is performed by comparing the value Q to the critical values listed in tables, where N is the number of observations and α is the level of significance: If the calculated value of Q is greater than the critical threshold the corresponding data value x1 is regarded to be an outlier.

Dean and Dixon suggested a more elaborate approach by using different formulas for different sample sizes in order to avoid the problem of two outliers on the same side of the distribution (Dixon 1953). They defined the following ratios and recommended that various ratios be applied as follows: for 3 <= N <=7 use r10; for 8 <= N <=10 use r11; for 11 <= N <= 13 use r21, and for n >= 14 use r22:

$$Q = r10 = |X2\text{-}X1|/|Xn\text{-}X1| \qquad (2)$$

$$Q = r111 = |X2\text{-}X1|/|Xn\text{-}1\text{-}X1| \qquad (3)$$

$$Q = r21 = |X3\text{-}X1|/|Xn\text{-}1\text{-}X1| \qquad (4)$$

$$Q = r22 = |X3\text{-}X1|/|Xn\text{-}2\text{-}X1| \qquad (5)$$

Tables proposed by Dixon (1953) show the critical values for r11, r21, and r22, respectively. R 10 is equal to Q.

Two of the statistical tests most often used in a group of unique data set are the proof of Dixon and the Grubbs test. Dixon test uses relationships between data spaces in different ways depending on the number of values in the data set. This value is compared with a critical value from a table, and the value is declared outlier value if it exceeds the critical value. The critical value depends on the sample size, n, and a level of representation chosen. The table usually uses low levels of representation such as 1% or 5%. (Dixon 1953).

Grubbs test uses a statistical test, T, which is the absolute difference between the outlier value X0 and the average of the X sample divided by the standard deviation of the sample, s.

Background values of Arsenic, Fluoride and vanadium in Salamanca and Juventino Rosas

Threshold values or Background values are reference concentration values of solutes that present a great probability to be systematically in an aquifer system without any anthropogenic influence. There are two types of background values; natural and environmental. The first correspond to geogenic concentrations related to the regional predominant rock and the water rock interactions, whereas the second corresponds to elements related directly or indirectly to an anthropogenic influence. Then GBV can be also divided in natural and no-natural. GBV are representatives only of a region and cannot be attributed to any recognized natural source of contamination in other areas (NREPC, 2004).

GBV are defined for areas with specific characteristic where can be identified the geological composition of the aquifer and the factors that control local and regional hydrodynamic. GBV cannot be assigned to all the aquifer system unless the aquifer presents homogeneity in its geological composition and a similar hydrodynamic behavior in its entire domain.

GBV are determined by means of an analytical data set representative of an area. Data are collected or selected from reliable historical archives (Runnells *et al*., 1992). There are several methodological proposals for GBV calculation. Before data management is carried out, the appraisals of outliers with Dixon's Q test rule out values that do not correspond with the rest of group values. In this case it was observed that the calculated values not exceed the values of tables and that data was rejected. The Environmental Protection Agency from US uses the Grubb Test to choose the concentration values to get a representative mean value (USEPA, 1988). Breckenridge and Crockett (1995) have used variation coefficient values (relationship between standard deviation and mean value) smaller than 0.5 to define the data set to be used.

The GBV are concentrations that vary from 10 % to 90 % of the percentiles of concentration distribution from the chosen data set (Kunkel *et al*., 2006). When the number of data is great, hundreds of data, regression or clusters analysis can be useful to get representative GBV (Vyas *et al*., 2001).

The GBV are not necessarily related to standards for any water use. The GBV for a risky element can be higher than the maximum concentrations recommended for potable water or other specific use. This situation occurs with arsenic concentrations reported in some aquifers (Hernández-García and Custodio, 2004; Armienta *et al*., 1997). When the GBV can be considered natural, it can be taken like pristine concentrations in areas where some elements can be originated from anthropogenic sources.

The Water Framework Directive of the European Union considers that in the definition of GBV must be included not only the aquifer characteristics but also the characteristics of the solute and water receptor bodies too (Muller *et al.*, 2006).

In Salamanca all the chemical analyzes were reviewed to choose only data obtained with the same analytical methodology. A data set was compiled and used for GBV determination.

The area was divided in Northern, Central and Southern Zone. The Lerma River that crosses the urban area is acting as a hydraulic barrier and a natural frontier. The division took also in consideration the geological composition of the aquifer (to the North prevail sedimentary units of variable granulometry like sand, gravels and clay, whereas to the south volcanic rocks; basaltic flows, fractured basalts and volcanic ashes). A shallow aquifer unit is located in the Central zone. The Northern

zone is a relatively pristine area, without the influence of the industrial area (Figure 1).

In JR the area was divided in three zones; NW zone with volcanic basaltic and ignimbrite-rhyolitic rocks: NE zone with volcanic ignimbrite-rhyolitic and sedimentary rocks and Southern, S, zone in the sedimentary plain. The division took in consideration the geological composition of the aquifer (to the North volcanic rocks; basaltic and ignimbrite-rhyolitcs flows, fractured volcanic rocks and ashes, whereas to the South prevail sedimentary units of variable granulometry like sand, gravels and clay the mainly igneous origin, interbeded with volcanic material as rhyolite and basalt). The Northern zones are relatively pristine areas. A shallow aquifer unit is located in the South zone. It is not excluded the influence of the agricultural activity.

The well Dulces Nombres, DN, was put in the NW zone, whereas the wells Val 1 and Val
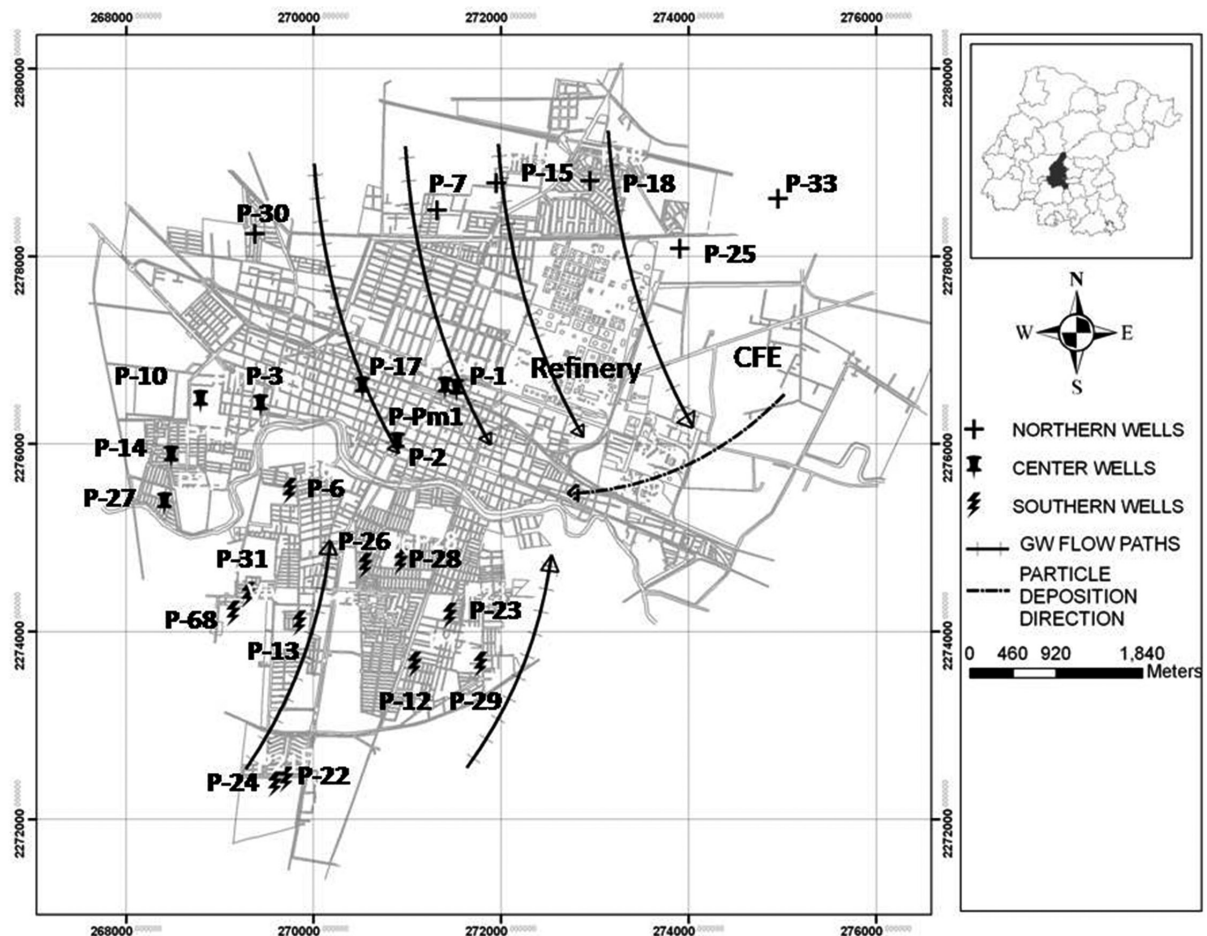
Figure 2. Well and GBV zoning in Salamanca, Mexico.
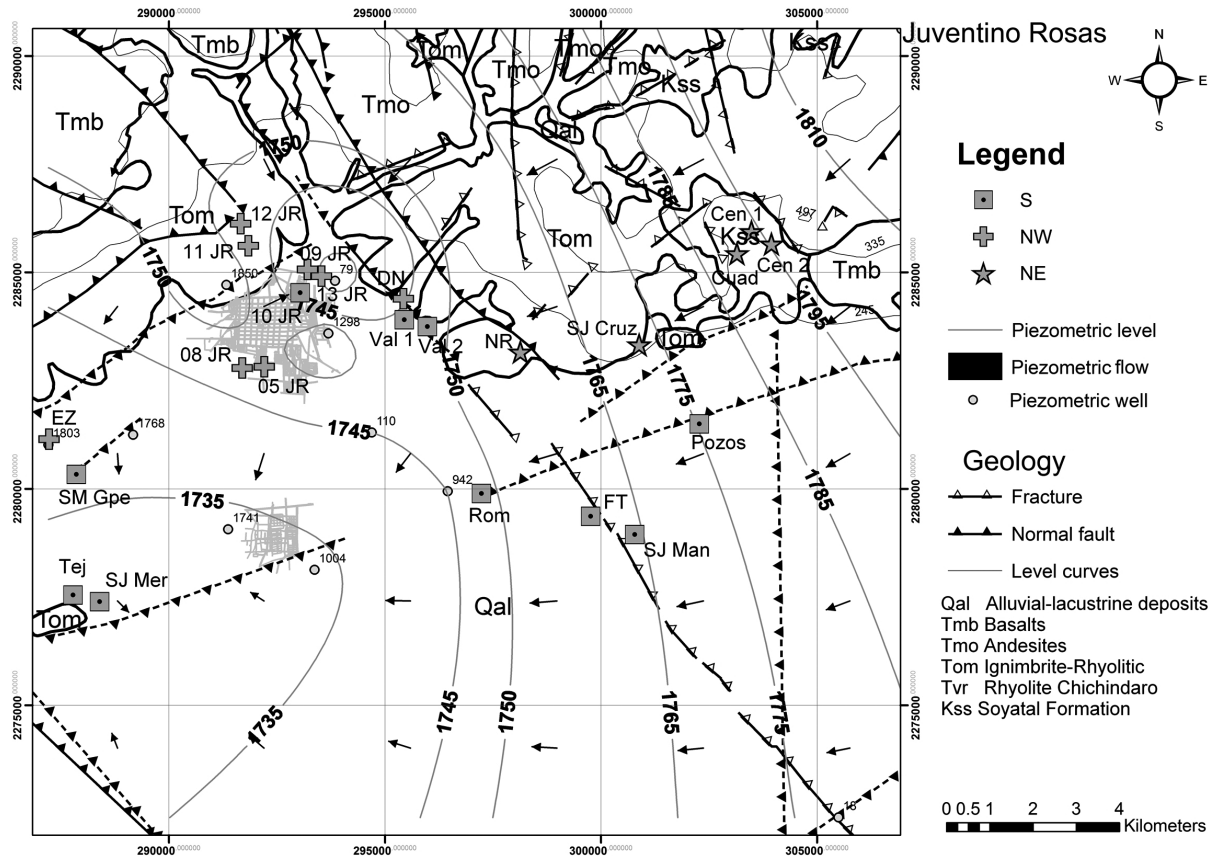
Figure 3. Wells and BVG zoning in Juventino Rosas, Gto. EZ= Emiliano Zapata; SM Gpe= Santa María Guadalupe; TEJ= Tejada; SJ Mer= San José Meríno; JR= Juventino Rosas; Val= Valencia; DN= Dulces Nombres; NR= Nuevo Rocillo; Cuad= Cuadrilla; Cen= Centeno; SJ Cruz = San José Cruz; Rom = Romerillo; FT= Franco Tavera; SJ Man= San José Manantiales.

2 in the zone S, although they are very close to each other. The well DN was drilled in rhyolites (Tom) and the wells Val 1 and Val 2 in volcanic sediments. The faults could be working as natural hydraulic conducts whereby hot water with other composition that infiltrated water can circulate. The hot water can alter the natural composition of the aquifer water.

Notwithstanding the Wells 9, 10 and 13 are located in the plain there are hydrochemical differences between them due to geological heterogeneities. The well 10, in the S zone, is intensely exploited for urban supply. It is one of the hottest wells that could be an indicator of a fault not mapped. The wells 9 and 13 were put in the NW zone because their hydrogeochemical behavior indicate that part of the well is extracting water from some rhyolitic unit.

The data set from Salamanca is formed by 51 files of 25 wells. Average and standard deviation, SD, were obtained for each well. The data set from Juventino Rosas is formed by 91 data files of 23 wells. Well distribution for Salamanca is showed in figure 2: The Northern Zone is represented by 6 wells; the central zone has 8 and the southern zone comprises 11. Well distribution for Juventino Rosas is showed in figure 3: The NW Zone is represented by 9 wells; the NE zone has 4 and the South zone comprises 10.

Results

Some of the detected concentrations are greater than the Mexican standards for drinking water (Figure 4). In the S zone of Salamanca, all wells have far exceeded the national standard for drinking water (Figure 2). The highest concentration was 0.076 mg/L in the well P 21. In the N zone, the As values were greater than the national standard, with a maximum in the well P 30, 0.777 mg/L. The wells of the central zone, (C), also had concentrations over the standard with a maximum of 0.068 mg/L in the well P 2. The maximum value of vanadium in the S zone was 0.091 mg/L in the well P22. For the N zone the greater concentration of V

was detected in the well P30, 0.062 mg/L. In the central area, the well P 10 had the highest V concentration, 0.065 mg/L.

The NE zone of Juventino Rosas of the wells exceeded the national standards for As and F. In the NW zone the wells JR 05 and JR 08 had concentrations over the As standard. The maximum value was found in the well JR 05, 0.036 mg/L. In the S zone, the wells Rom, Tej, Val 1 and JR 10 had values over the standard with a maximum in the wells Pozos and JR 10, 0.046 mg/L. The wells Tej, Val 2, Rom, Pozos, JR 10 and SJ Mer exceeded the standard for F; the highest value was 2.95 mg/L in the well Tej.

Three set of mean values with its SD were calculated. The Grubb Test, (Z), was applied to each data set. If Z is greater than the table values for N data, the respective well is excluded of the data set because the concentration does not correspond to a normal distribution. The Grubb Test considers the mean, the SD and the concentration value for each well (NREPC, op cit).

$$Z = \frac{(Mean - Individual\ concentration\ value)}{SD} \qquad (6)$$

The obtained results for Salamanca show that (Table 1) for the Northern and southern zones the GBV for arsenic are greater than the Mexican standard for drinking water, 0.025 mg/L. In the Central zone the GBV is lower, 0.023 mg/L.

Table 1. Background values for arsenic and vanadium in Salamanca Gto.

Zone	GBV (mg/L)		SD	
	As	**V**	As	V
South	0.030	0.037	0.010	0.016
Center	0.023	0.032	0.008	0.015
North	0.029	0.028	0.008	0.012

Vanadium has not standards for drinking water in Mexico even EPA does not consider it in the Secondary standards. The lowest values, 0.028 mg/L, were found to the North increasing the concentrations to the south reaching 0.037 mg/L.

The obtained results for Juventino Rosas show that (Table 2) for the S zone the GBV for arsenic are at the limit of the Mexican standard for drinking water, 0.025 mg/L. In the NE and NW zones the GBV are lower than the Mexican standard, 0.003 and 0.013 mg/L.

For the S zone the GBV for Fluoride, 1.93 mg/L, is greater than the Mexican standard for drinking water, 1.5 mg/L. The lowest values, 0.81 mg/L, were found to the NE increasing the concentrations to the NW1.19 mg/L.
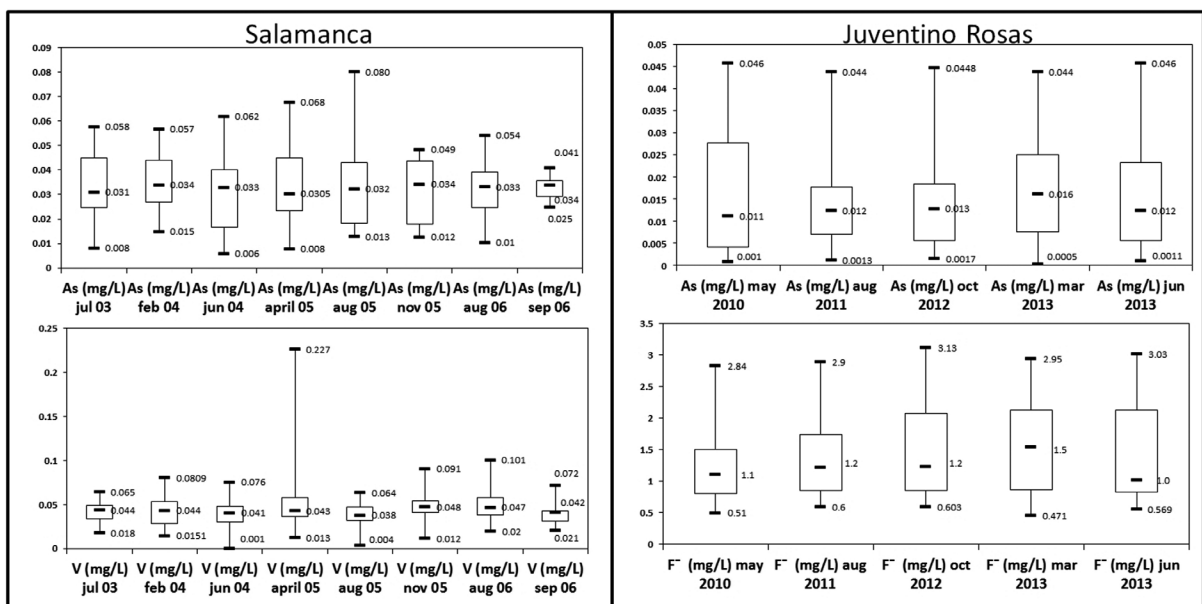
Figure 4. Summary of As, F and V of groundwater concentration in Salamanca and Juventino Rosas.

Table 2. Background values for arsenic and fluoride in Juventino Rosas, Gto.

Zone	GBV (mg/L)		SD	
	As	**F**	As	F
NE	0.003	0.81	0.002	0.08
NW	0.013	1.19	0.008	0.63
S	0.024	1.93	0.013	0.75

In 2009 some wells of Salamanca were sampled founding similar values for As and V in the South-western Zone (Rodriguez 2009). In piezometers located in the industrial area, greater concentrations than the GBV (obtained in this work) were found (Hernandez et al., 2007). The increase can be related to contamination processes due to the particulate deposition described above (Mejia et al., 2007). The particulate can fall and be deposited over the terrain and then can be incorporated to infiltrations of rain water or pipeline leakages.

In urban wells in Irapuato City, 20 km North-West Salamanca, V mean concentrations are 0.022 mg/L and for As 0.017 mg/L (lower than the GBV found in Salamanca). Although in "El Copal" a small community out of the Irapuato urban area Arsenic concentrations of 0.33 mg/L have been reported (Rodriguez et al., 2006).

The As and F- concentration in Juventino Rosas, occurs naturally in the aquifer by hydrogeochemical phenomena, but an anthropogenic contribution cannot be discarded. It is observed that some natural background values, especially for the area S, are above the values allowed by the NOM-127, consequently the site is of inadequate quality water for human consumption.

The processes controlling the release of As and F in Juventino Rosas groundwater

In Juventino Rosas the water temperature is above 36° C to 50° C on surface, Na-HCO$_3^-$ and Na-Ca-HCO$_3^-$ rich hydrothermal waters are formed by the interaction of thermal fluids with the host-rock (Morales et al., 2015). Regularly As and F- concentrations are higher in geothermal systems (Giggenbach, 1981). Due to hydrothermal and supergene processes that occur in different parts of Juventino Rosas, progressive alteration processes and formation of new mineralogy were observed, mainly in volcanic material of ignimbritic and rhyolitic

composition. The excess of F- and As, and low Mg^{2+} and Ca^{2+} could be a response to exchange processes between rock and hydrothermal aqueous fluids (Ellis and Mahon, 1964).

Grondwater wells with high temperature (24-48°C) are common in Juventino Rosas area. Deep faults and fractures systems are observed in the area (Figure 3), in addition, the geological background and the aquifer overexploitation due to the intensive use of groundwater for agriculture and urban supply, originated subsidence faults and fractures that can act as preferential channels for recharge and also for ascendant geothermal water. Faults and fractures can allow the migration of hydrothermal flows with As and F to surface. The hottest wells are located very near of faults. The zone S presents the highest As and F concentrations; in this area there are the greater number of hot wells, also there are a fault and fracture system with NW-NE orientation. The zone S corresponds to a basin with rhyolitic volcanic sediments. These rocks have arsenic and fluorine minerals. The fault and fracture system controls the geothermal water circulation. Groundwater accelerates the weathering processes of the silicate minerals originating high Na and HCO$_3^-$ concentrations and the mobilization of As and F.

Proposal of groundwater planning and management for Salamanca

The Water Framework Directive supports the idea to use GBV to guarantee that no affectations to population and groundwater dependent ecosystems are produced (Grima et al., 2015). GBV of well characterized aquifers can be an important tool to define management policies of aquifer systems mainly around urban areas and/or industrialized zones. One of the objectives of the BRIDGE project is to define methodologies to get groundwater background values (Hinsbyetal, 2008; Edmunds et al., 2008; Muller et al., 2006 a; Muller et al., 2006b). In Mexico some isolate efforts were made to that respect (Cardona et al., 1993).

In areas where subsidence phenomena occur, fractures and faults appear, increasing locally aquifer vulnerability. If in such areas there are soluble contaminants, these can be migrate to shallow aquifers. This is occurring in Salamanca and Juventino Rosas as well in Irapuato City, where more than 18 subsidence faults have been reported (Rodriguez, 2006).

Particulate normally is not considered as potential source of aquifer contamination. Most studies have considered it as an atmospheric

pollutant. There are recent studies about its role of health risk for the population living in areas with aggressive particulate (Gallus *et al*., 2008; Tadjine *et al*., 2008). The particulate generated by burned "combustoleo" contains important concentrations of arsenic, vanadium, nickel and zinc, between other risky elements (besides sulfur compounds).

Once deposited on the soil some particulate elements are susceptible to migrate to permeable formations. They can migrate with rainfall, irrigation water or leakages from sewages or potable water pipelines. The groundwater vanadium concentrations are lower in the pristine areas (North area) than in the central and southern ones in Salamanca (Figure 2). The latter could be affected by particulate deposition.

GBV allow differentiating in an easy way if measured concentrations are normal, from geogenic origin, or if they can be related to some anthropogenic process. The correlation between vulnerable areas, potential sources of pollution and GBV by area, allows a preliminary definition of a contamination process.

In Salamanca the found GBV corresponds to the local background altered by the slow incorporation, during at least 50 years, of risky elements infiltrated from particulate or inadequate waste disposal sites.

In Juventino Rosas the found GBV are related to natural hydrogeochemical processes that occur in the aquifer, the presence of faults and fractures allows the migration of hydrothermal fluids that increases the presence of As and F, mainly in the S zone.

GBV and aquifer vulnerability assessments can be incorporated in urban land planning, in the definition of protected areas, to locate adequate points for groundwater monitoring wells or for urban wells for urban supply. Water and environment stakeholders can be use them in projects aiming for sustainability.

Institutions in charge of Water at national level, CONAGUA (National Commission of Water), to state and municipal level must have information regarding quality aspects like analytical results, potential sources of contamination and solutes related to all identified potential sources. In developing countries the use of GIS is not so extended as in developed ones. In a GIS it is possible to put together, GBV zoning, aquifer vulnerability assessments, geological maps, mathematical models scenarios, water assigned volumes and

even more. All this information can improve water administration and management in an integral and sustainable way.

Discussion and Conclusion

Salamanca and Juventino Rosas, JR, are located in an almost similar geological environment. However, the aquifers in both areas show some differences, while in JR there are low-temperature manifestations, in Salamanca there are not. The volcanic basement in Salamanca is located to a greater deep than in JR (Rodriguez *et al*., 2001). Most of Salamanca wells are placed in lacustrine and fluvial sediments whereas in JR some wells were drilled in heterogeneous sediments and in volcanic rocks. The faults in JR allow deep flow contributions to the aquifer system altering the local hydrogeochemistry.

The differences between both areas propitiated that the GBV may not be similars. In Salamanca in the three defined zones, the As GBVs are greater than in the JR zones (Figures 2 and 3). The As concentrations varies spatial and temporally. The very low F concentrations in Salamanca allow suppose that the F in JR can be associated to the geothermal flow.

The highest values obtained in the S zone of Salamanca were expected since this area corresponds to the deposit of particulate enriched in these elements (As and V) (Rodríguez *et al*., 2002). Is quite difficult to define which origin is most important.

In JR there are not anthropogenic sources of As and F. Both elements are of geogenic origin. The geogenic sources can be two; the As and F-bearing rocks, mainly volcanic rocks, rhyolites, and As and F in the hot deep flow. The existence of vertical ascendant flow along the faults was been verified by a piezometric dome in the center of the plain (Morales *et al*., 2014.

Acknowledgements

References

APHA, AWWA, WWF, 2005, *Standard methods for the Examination of Water and Wastewater*. American Public health Association, the American Water Works

Association, Association Water Environment Federation, Washington, D.C.

Armienta A., Rodríguez R., Aguayo A., Ceniceros N., Villaseñor G., Cruz O., 1997, Arsenic contamination of groundwater at Zimapán, Mexico. *Hydrogeology Journal,* 5, 2, 39-47 pp.

Breckenridge R., Crockett A., 1995, Determination of background concentrations of inorganics in soil and sediments at hazardous waste sites. Engineering Forum Issue, *Report EPA/540/S-96/500,* 32 pp.

Cardona A., Carrillo-Rivera J., Armienta A., 1993, Elementos traza: contaminación y valores de fondo en aguas subterráneas de San Luis Potosí, México. *Geofísica Internacional*, 32, 2, 277-286 pp.

Cerca-Martínez L.M., Aguirre-Díaz G.J., López-Martínez M., 2000, The geological evolution of the southern Sierra de Guanajuato; a documented example of the transition from the Sierra Madre Occidental to the Mexican *Volcanic Belt. Int. Geol. Rev.,* 42, 131-151 pp.

Edmunds W.M., Shand P., Hart P., Ward R., 2003, The natural (baseline) quality of groundwater: a UK pilot study. *Science of the Total Environment,* 310 Issues 1-3, 25-35 pp.

Eugster H.P., 1986, Minerals in hot water. *Am. Mineral.,* 71, 655-673.

Dixon W.J., Dean R.B., 1951, Simplified Statistics for small numbers of observations. *Anal. Chem.,* 23, 636-638.

Dixon W.J., 1953, Processing data for outliers. *J. Biometrics,* 9, 74-89.

Ferrari L., 2000, Avances en el conocimiento de la Faja Volcánica Transmexicana durante la última década. *Boletín de la Sociedad Geológica Mexicana,* 53, 84-92 pp.

Foster S., Hirata R., 1988, Determinación del riesgo de contaminación de aguas subterráneas, una metodología basada en datos existentes. *Publicación de la Organización Panamericana de la Salud*, (OMS), Vol. VII, 79 pp.

Gallus S., Negri E., Boffeta P., McLaughlin J., Bosetti C., Vecchia C., 2008, European studies on long-term exposure to ambient particulate matter and lung cancer. *European Journal of Cancer Prevention,* 17, Issue 3, pp 191-194.

Grima J., Luque-espinar J.A., Mejia J.A., Rodriguez R., 2015, Methodological approach for the analysis of groundwater quality in the framework of the Groundwater Directive. *Environ Earth Sci*, DOI 10.1007/s12665-015-4472-x.

Hinsby K., Condesso de Melo M.T., Dahl M., 2008, European case studies supporting the derivation of natural background levels and groundwater threshold values for the protection of dependent ecosystems and human health. *Science of the Total Environment,* 401, Issues 1-3, 1-20 pp.

Hernandez-García E., Custodio E., 2004, Natural baseline quality of Madrid tertiary detrital aquifer groundwater (Spain): a basis for aquifer management. *Environmental Geology,* 46, 173-188 pp.

Hernández H., Rodríguez R., Morton O., Armienta A., Morales P., 2007, Presencia de metales en suelos y agua subterránea en la zona urbana de Salamanca, Gto. *Reporte Técnico, FOAM. COTAS Irapuato Valle de Santiago*, CEAG. 72 pp.

Kunkel R., Berthold G., Blum A., Elsass P., Fritsche J.G., Wendland F., Wolter R., 2006, Assessment of natural background levels and threshold values for groundwater bodies in the Upper Rhine Valley (France and Germany). *Geophysical Research Abstracts*, European Geosciences Union Assembly, 2 pp.

LAQUIMIA, 2004 Analytical Determination Report. Laboratorio Químico Industrial y Agrícola, S.A. de C. V. Irapuato, Gto. Inedit 3 pp.

Marañón B., 2010, Agua subterránea: gestión y participación social en Guanajuato. UNAM, Instituto de Investigaciones Económicas: Ed. Juan Pablos, 21 pp.

Mata E., 2006, Correlación entre la emisión de gases de combustión a la atmósfera y la presencia de vanadio en el agua subterránea en la Cd. de Salamanca, Gto. Master Degree Thesis. Master in Water sciences, Guanajuato Univ., Mexico 51 pp.

Mejía J.A., Rodriguez R., Armienta A., Mata E., Fiorucci A., 2007, Aquifer vulnerability

zoning, an indicator of atmospheric pollutants input? Vanadium in the Salamanca aquifer, Mexico. *Water Air and Soil Poll.*, 185, num 1-4, 95-100 pp.

Morales J.I., Villanueva-Estrada R.E., Rodríguez R., Armienta A., 2014, Geological, hydrogeological and geothermal factors associated to the origin of arsenic, fluoride and high groundwater temperature in a volcanic environment El Bajío Guanajuatense, Ph.D. Thesis UNAM Mexico. *Enviromental Earth Sciences*, 74, 6, 5403-5415.

Muller D., Fouillac A., Hart A., Quevauviller P.H., 2006, BRIDGE Background criteria for the identification of Groundwater threshold values. *Proceedings European Groundwater Conference*, Chapter 1.3.4, 6 pp.

Müller D., Blum A., Hart A., Hookey J., Kunkel R., Scheidleder A., 2006, Final proposal of a methodology to set up groundwater threshold values in Europe. *BRIDGE* (2005) en www.wfd-bridge.net

NREPC, 2004, Kentucky Guidance for ambient background assessment. Natural Resources and Environmental Protection Cabinet, NREPC. *Inedit Kentucky* USA.9 pp.

Reimann C., Garret R.G., 2005, Geochemical background – concept and reality. *Science of the Total Environment*, 350, 12-27 pp.

Rodríguez R., Mejía J.Á., Berlín J., Armienta A., González T., 2000, Estudio para la determinación del grado de alteración de la calidad del agua subterránea por compuestos orgánicos en Salamanca, Gto. *Reporte Técnico CEASG, IGF-UNAM*. 89 pp.

Rodríguez R., Reyes R., Rosales J., Berlín J., Mejía J.A., Ramos A., 2001 Estructuración de mapas temáticos de índices de vulnerabilidad acuífera de la mancha urbana de Salamanca Gto. Municipio de Salamanca. *Reporte Técnico CEAG, IGF-UNAM.* 99 pp.

Rodríguez R., Armienta A., Berlin J., Mejia J.A., 2002, Arsenic and lead pollution of the Salamanca Aquifer system. Origin, mobilization and restoration alternatives. Groundwater Quality. Edited by Steven F. Thornton & Sascha E. Oswald. Red Book IAHS, 275, Inglaterra, 561-567 pp.

Rodríguez R., Armienta A., Morales P., Silva T., Hernández H., 2006, Evaluación de Vulnerabilidad Acuífera del valle de Irapuato Gto. *Reporte Técnico JAPAMI, CONCyTEG, IGF UNAM.* 90 pp.

Rodríguez R., Rodríguez I., 2006, Consecuencias sociales de un desastre inducido, subsidencia. *Boletín de la Sociedad Geológica Mexicana,* Tomo LVIII, Num 2, 265-269 pp.

Rodríguez R., Morales I., Armienta A., Villanueva R., Segovia N., 2015, Geothermal systems of low temperature in Mexican Highlands: Alternative uses and associated risks. *Procedia Environmental Sciences* pp. 214-219.

Runnells D., Shepherd T.A., Angino E., 1992, Metals in water, determining natural background concentrations in mineralized areas. *Environ. Sci. Technol.,* 26, 12, 2316-2323 pp.

Salinas V., Diego A., Porcado J., 2001, Uso de crudo maya despuntado como combustible alterno al combustoleo, *Boletín* IIE, Año 25 25, 126-130 pp.

SEMARNAT, 2013, Programa de Gestión para Mejorar la Calidad del Aire de Salamanca, Celaya e Irapuato, 2013-2022. http://www.semarnat.gob.mx/sites/default/files/documentos/calidadaire/proaire_salamanca-celaya-_irapuato_2013_2022.pdf

Tadjine A., Courtois A., Djebra H., 2008, Toxicity of dust of dimissed complex of steel annaba on some hematologic parameters of rabbit (Europeus). *Environmental Research Journal* 2, 2, pp. 76-79.

United States Environmental protection Agency (USEPA) (1995) Determination of background concentrations of inorganics in soils and sediments at hazardous waste sites. *Report EPA/540/S-96/500, Office of Research and Development, Office of Solid Wastes and Emergency Response* USEPA, 79 pp

Vyas V., Roy A., Strawderman W., Georgopoulos P., David D., 2001, Defining background groundwater quality at the Savannah River site. *Technical Report CCL/RESP TROI-01*, State University of New Jersey, US.52 pp.

Tectonic Interpretation of Topographic Lineaments in the Seacoast Region of New Hampshire, U. S. A.

José Cruz Escamilla-Casas[*] and Jeffrey E. Schulz

Resumen

La identificación de lineamientos topográficos en modelos digitales de elevación, en sondeos batimétricos de alta resolución y en un mapa predictivo de la topografía del lecho rocoso, permite precisar las trazas de fallas asociadas al Sistema Norumbega, en la costa de New Hampshire. El análisis de polos simples de Euler sugiere que la formación del cauce de los ríos Cocheco y Piscataqua muy probablemente estuvo relacionada con los mecanismos de emplazamiento del Complejo Agamenticus del Mesozoico. Los análisis en perfiles topográficos, sondeos batimétricos, topografía del lecho rocoso y el análisis estructural de la deformación frágil confirman la presencia de un cuerpo plutónico sub-circular no expuesto. Finalmente, presentamos un modelo que explica, tentativamente, la evolución tectónica del estuario Great Bay.

Palabras clave: Estuario de Great Bay, formación Rye, grupo Merrimack, sistema de fallas Norumbega, análisis Kriging.

Abstract

The identification of topographic lineaments on Digital Elevation Models, high-resolution bathymetric soundings, and an ordinary Kriging prediction map provide the basis for refinement of the traces of known fault zones associated with the Norumbega Fault System in the seacoast region of New Hampshire. On the present topography, simple Euler poles analysis suggests the association of the course of the Piscataqua and the Cocheco rivers with the mechanics of emplacement of the Mesozoic Agamenticus Complex. Topographic profiles, bathymetric soundings, structural analysis of brittle structures, and an ordinary Kriging prediction map of the bedrock topography support the presence of a sub-circular structure that is being interpreted as related to a subsurface plutonic body. An extensional regime model is being presented to illustrate the possible tectonic evolution of Great Bay tidal estuary.

Key words: Great Bay estuary, Rye formation, Merrimack group, Norumbega fault system, Kriging analysis

J. C. Escamilla-Casas[*]
Universidad Autónoma del Estado de Hidalgo
Área Académica de Ciencias de la Tierra y Materiales
Carr. Pachuca-Tulancingo, Km 4.5
Mineral de la Reforma, Hidalgo
[*]Corresponding autor: jocesca@uaeh.edu.mx

J. E. Schulz
Weston Solutions, Inc.
425 G King Street
Suite 300
Anchorage, AK 99501

Introduction

The identification of fracture traces and lineaments on aerial photographs (Lattman, 1958; Shake and McHone, 1987), satellite images, topographic maps (Ferguson *et al.*, 1997; Ferguson, 1997; Riley, *et al.*, 1999), and high-resolution digital terrain models (Ludman, 1999) are common methods that have been used for decades to assist with bedrock geologic mapping in New England. These methods have proven effective in tracking large geologic structures in areas of poor rock exposure, thereby facilitating the interpretation of extensive areas (Rasco and Warner, 1999; Riley, *et al.*, 1999).

In seacoast New Hampshire, a first attempt to correlate on- and offshore structures was made by Birch (1984) who published his work based on detailed marine geophysical surveys, patterns of magnetic anomalies, and bedrock topography of the inner continental shelf. A bedrock-topography prediction map and a topographic lineament map of southeast New Hampshire and southwestern Maine were generated for this study. A regional, pervasive northeast to southwest trending structural grain and the most prominent geologic structures are easily visible on these maps.

The topographic lineament map and the high resolution bathymetry assisted in the identification of the traces of presently mapped ductile and brittle faults zones (*e.g.* Nannie Island and Portsmouth Fault Zones). The traces of these lineaments suggest that these fault zones are likely associated with the Norumbega Fault System of the New England Appalachians (Ludman and West, 1999). In the interpretation presented here, these prominent lineaments are associated with bedrock structures. These lineaments are used to refine traces of fault zones that were mostly inferred, due to poor or nonexistent rock exposure, as shown on recent geologic maps (*e.g.* Bothner, *et al.*, 2004; Escamilla-Casas, 2003). Additionally, this study analyzes and refines the Burlington-Portsmouth topographic lineament (McHone, 1998) and re-names it Burlington-York Lineament.

This study also identifies a sub-circular structure that is observable on both, the bedrock-topography prediction map and the topographic lineament map. This structure is being interpreted as related to a not presently exposed plutonic body. On surface topography, the structure is delineated by a local topographic elevation and a radial drainage pattern, while on bedrock topography, the structure occupies a topographic high. Structural analysis of the brittle deformation in and along the boundaries of the sub-circular structure denotes a relative vertical displacement and tilting to the west of the rock cap.

Based on this data, an innovative tectonic interpretation of the geological evolution of the area based on an extensional model related to the possible emplacement of a pluton is proposed. In this model, the emplacement of the pluton influenced the evolution of Great Bay tidal estuary and the geometry of the course of the Piscataqua and Cocheco Rivers, in the context of the opening of the North Atlantic Ocean during the Mesozoic.

Geologic setting

The study area is located in the seacoast area of New Hampshire and southwestern Maine (Figure 1). This region is underlain by lower Paleozoic metaigneous and metasedimentary rocks (Lyons *et al.*, 1997; Osberg *et al.*, 1985). Tectonostratigraphically, the area includes, from east to west, the Rye Complex and the eastern portion of the Merrimack Group. The Rye Complex, originally the Rye Formation of Billings (1956), is an association of variably metamorphosed and mylonitized calcareous and non-calcareous meta-sandstone and meta-siltstone with migmatized and non-migmatized metapelite (Hussey, 1980; Hussey and Bothner, 1993). Bothner and Hussey (1999) identified the Rye Formation as the most important ductile unit present in New Hampshire, and re-named it the Rye Complex. Recent efforts have been made to investigate the age of the Rye Complex; however these studies are not conclusive (Kane *et al.*, *2010)*. The Merrimack Group is a thick sequence of variably metamorphosed calcareous turbidites, stratigraphically subdivided into (from youngest to oldest and east to west) Kittery, Eliot, and Berwick Formations (Billings, 1956; Bothner *et al.*, 1984; Hussey, 1968; Hussey, 1985; Katz, 1917; Novotny, 1969, Schulz, 2004, Sorota *et al.*,2011, and Sorota, 2012). A fault with early ductile and late brittle components separates the Eliot Formation and the Berwick Formation (Escamilla-Casas, 2003; Bothner *et al.*, 2004; Hussey *et al.*, 2007), with recent interpretations indicating that it is a thrust fault (Wintsch, *et al.*, 2007). Detailed geology and stratigraphy of the Merrimack Group and the Rye Complex in the study area are discussed in Ludman and West (1999) and in Hussey (Hussey *et al.,* 2010). The youngest sedimentary materials in the research area are Quaternary deposits, mostly unconsolidated glacial deposits.
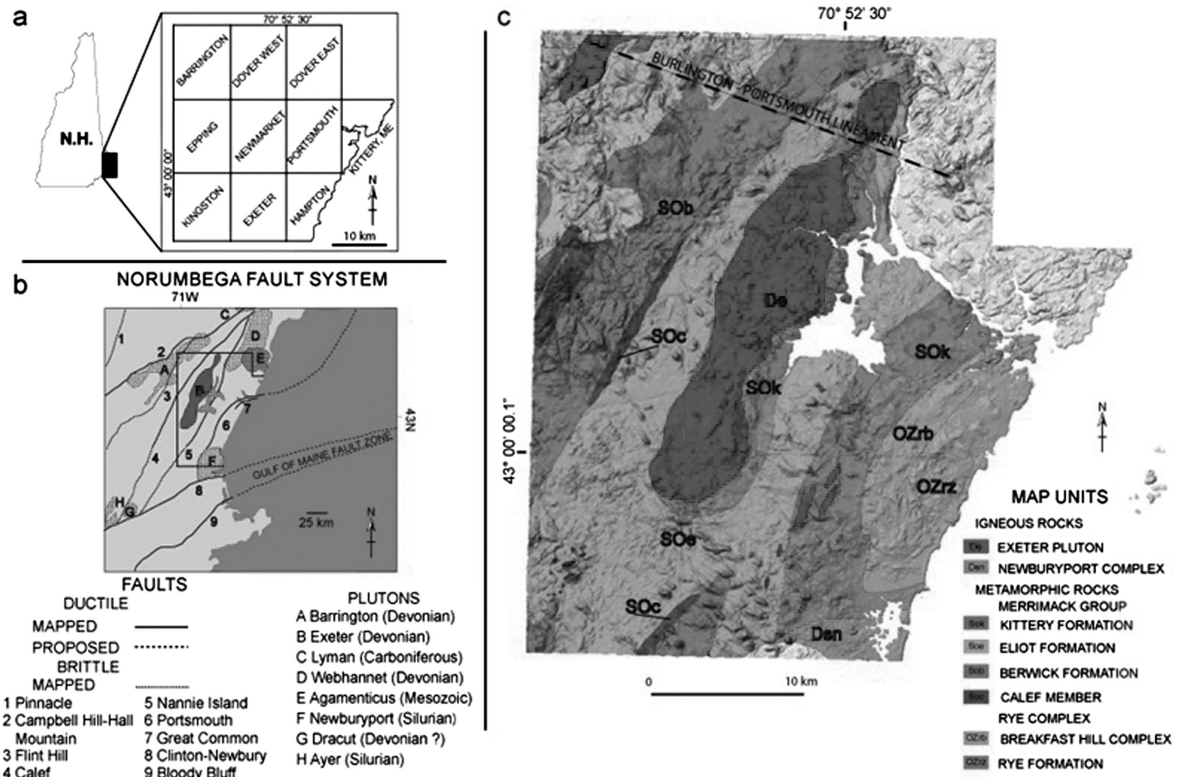
Figure 1. (a) Nine 7.5 minute quadrangles of southeast New Hampshire and one southern Maine quadrangle that make up the study area. (b) Simplified map of the Norumbega Fault System, the polygon outlines the area of the mosaic (adapted from Bothner and Hussey, 1999). (c) Mosaic of merged Digital Elevation Models and high-resolution bathymetry with draped New Hampshire geology from Lyons, *et al*. (1997).

Intrusive igneous rocks in seacoast New Hampshire consist of the Exeter Pluton and the Newburyport Complex for which Bothner *et al*. (in Lyons *et al*., 1997) reported U/Pb ages of 406 ± 1 and 418 ± 1 Ma, respectively. More recently, Bothner *et al*. (2008) reported new $^{206}Pb/^{238}U$ dates of the dioritic (407.7 Ma) and the gabbroic (407.4 Ma) phases of the Exeter Pluton. In southwestern Maine, are the Webhannet Pluton (403 ± 14 Ma; Gaudette *et al*., 1982) and the Agamenticus Complex (228 ± 5 Ma; Brooks, 1990 and references therein). McHone and Butler (1984) included the Mesozoic (210-240 Ma) igneous rocks of the study area into the Coastal New England igneous province.

Northeast-trending fault zones with predominantly ductile dextral shear and superimposed brittle-ductile deformation crosscut the study area (Figure 1b). From east to west these shear zones are, Great Common, Portsmouth, Nannie Island, and Calef (Bothner and Hussey, 1999; Carrigan, 1984; Escamilla-Casas, 2003). The spatial distribution of these presently mapped ductile and brittle faults

(northeast trending lineaments, Figure 1b) suggest that these faults extend offshore to the east, following a pattern associated with the Norumbega Fault System of the New England Appalachians (Ludman and West, 1999 and references therein).

Recent investigations indicate that the tectonic activity of the Norumbega Fault Zone (West and Roden-Tice, 2003) intermittently spans, from Middle Devonian to Late Cretaceous time. Moreover, to the north, a northwest-southeast trending prominent lineament that crosscuts the study area is presumably, a segment of the Burlington-Portsmouth topographic lineament (McHone, 1998), (Figure 1b).

In recent tectonic models, the oldest stages of deformation and metamorphism that affected the study area have been interpreted as being associated with the Acadian Orogeny (e.g. Bradley *et al*., 2000). Alternative models suggest the tectonometamorphic evolution of the area as the result of continuous deformation and metamorphism that initiated in the Late

Ordovician and extended into the Permian (Alleghanian Orogeny) e.g. van der Pluijm *et al*. (1993).

The youngest deformational event imprinted on the bedrock topography of the study area is very likely related to the tectonism associated with the opening of the Atlantic during the Mesozoic, e.g. Swanson (1982). Most geodynamic models relate the Mesozoic rifting between North America and Eastern Africa to mantle plume mechanisms (White and McKenzie (1989); Hill, (1991), and others). However, McHone (1996 and 2000) outlined chronologic and petrologic evidence from mafic dikes and flood basalts that are not consistent with the frame of a mantle plume model as a viable explanation for the opening of the Atlantic Ocean during the early Jurassic time. Furthermore, the younger Early Cretaceous hotspots present in the eastern Atlantic Ocean are responsible for alkaline magmatism that cannot be associated chronologically with rift basalts (Duncan, 1984; McHone, 2000). Nevertheless, both the Early Jurassic and Early Cretaceous geologic episodes are related to the extensional tectonics associated with the opening of the North Atlantic Ocean during the Mesozoic (McHone and Butler, 1984; McHone, 1988 and 2000).

Materials and methodology

For this study, ArcView V. 6.1 was used to retrieve and drape geologic information (Lyons *et al*., 1997) (Figure 1b) onto land topography, produce a bedrock-topography prediction map, and a topographic lineament map (Figure 2 and 3, respectively). The configuration of these two maps consists of merged high-resolution-bathymetry of Great Bay and Portsmouth Harbor (CCOM-JHC-UNH) with land topography Digital Elevation Models (DEMs) (GRANIT-UNH and USGS). Characteristics of the high resolution bathymetry and inland topography datasets are described by Cutter (2005) and in the UNH GRANIT website, respectively. Land topography of the study area covers three rows, each row containing three USGS 7.5 minute quadrangles: Barrington, Dover East, Dover West, Epping, Newmarket, Portsmouth, Kingston, Exeter, and Hampton (Figure 1a). The offshore dataset covers 839m by 2034m, with the center of the lower left corner grid cell originating at Universal Transverse Mercator (UTM) Northing 4768915m, Easting 360918m (Cutter, 2005). The land topography dataset of each 7.5 minute quadrangle was reprojected from NH State Plane feet, zone 4676 to NAD 27, zone 19 and then merged into a mosaic of nine 7.5 minute quadrangles. Despite
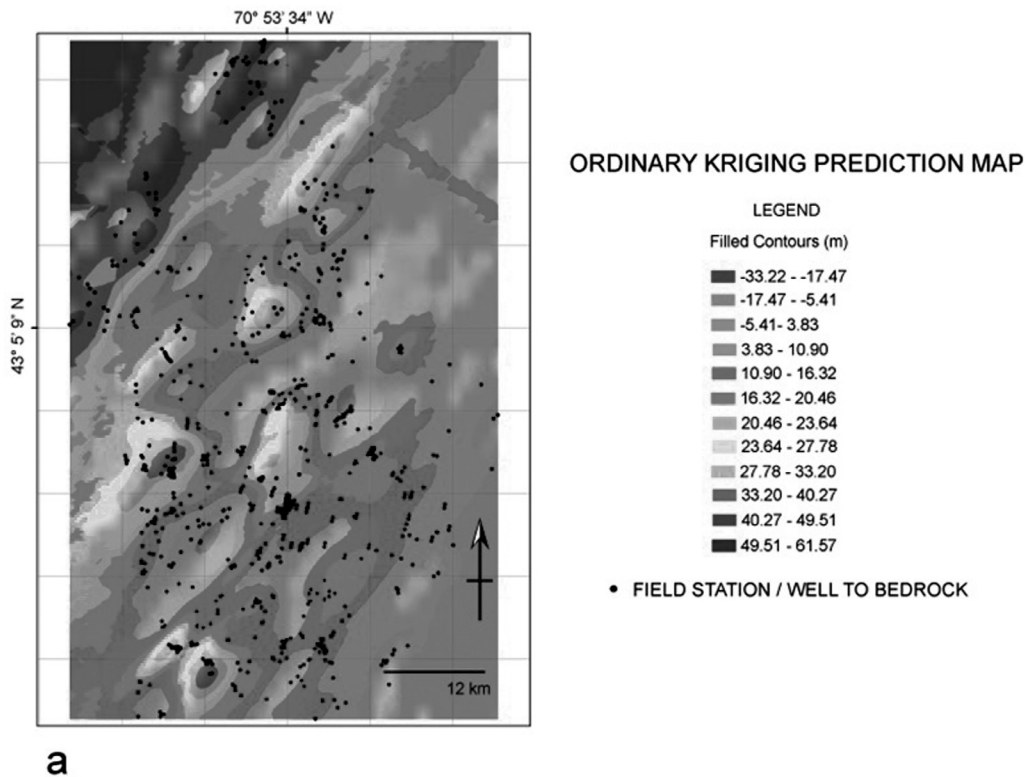
Figure 2. Estimated bedrock topography of the study area. (a) Approximation of the bedrock topography prediction map based on an ordinary Kriging analysis. Contour interval varies from −33.22 m to 17.47 m.
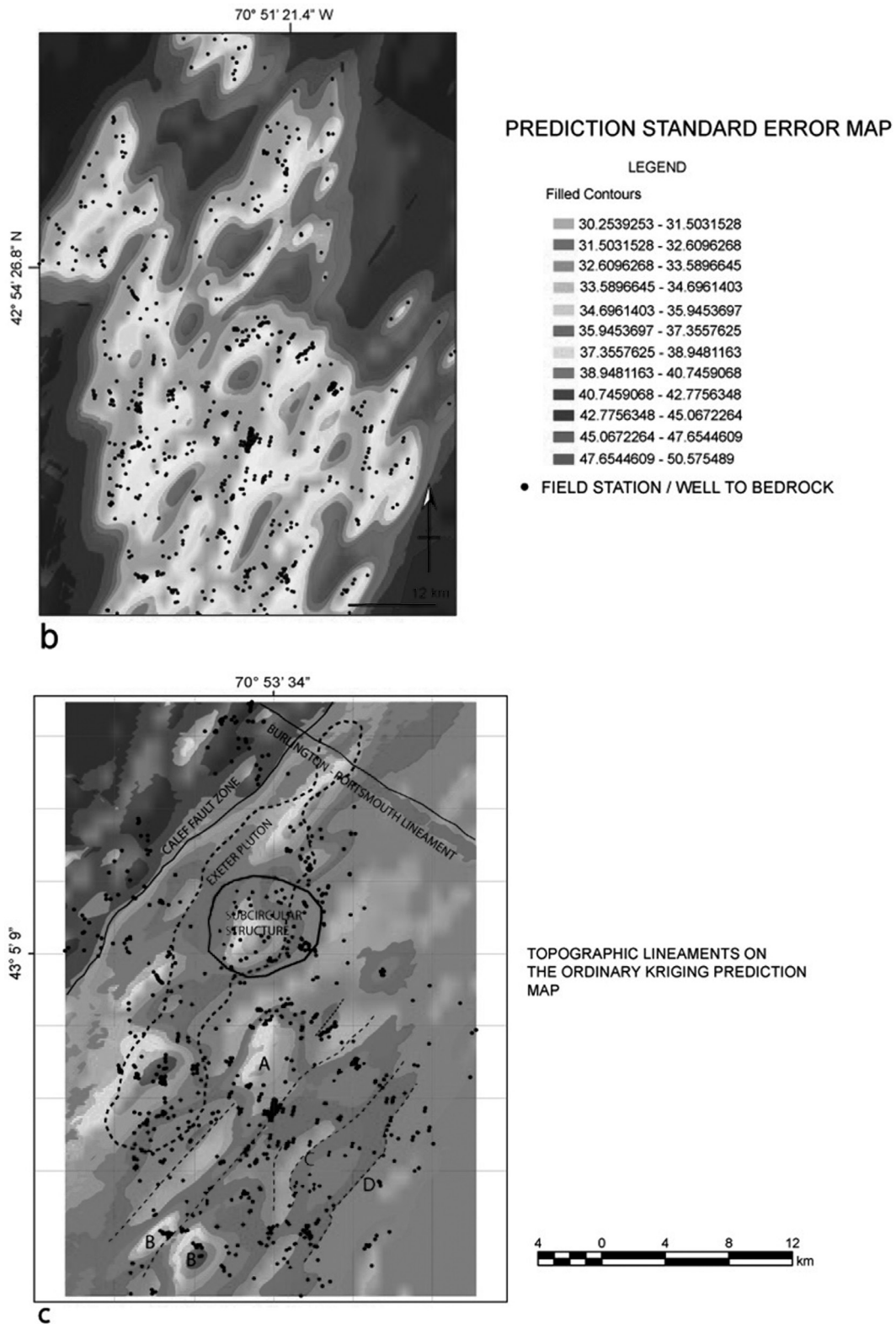
Figure 2. (Continue) (b) Prediction standard error map derived from the ordinary Kriging analysis showing the uncertainty of the predictions. Higher certainty values are indicated in light gray. Contour interval varies from 30.25 to 50.57. (c) Interpretation of topographic lineaments based on the ordinary Kriging prediction map. The configuration also shows major geological features discussed in this paper, e.g. Calef Fault, Burlington-Portsmouth lineament, and the sub-circular structure. For reference, the Exeter Pluton is indicated with a thick dashed line.

the fact that land and offshore datasets are presented on UTM projection (zone 19 north), for merging both datasets, the altitude values in the land topography were converted from feet into meters. In each case, the merging procedure was performed by using the ArcMap V.3.2. Data Management-toolbox merge tool. The resulting merged map presents two levels of resolution, 30 m for the inland topography and 3 m for the seafloor.

ArcMap V.3.26 Spatial Analyst and the ordinary method was used to generate the bedrock-topography prediction map from a 3D Kriging analysis based on location coordinates and elevations of outcrops, and depth to bedrock data from wells (z-values). The generated bedrock-topography prediction map provides evidence that supports the pervasive northwest – southeast structural grain, the presence of the sub-circular structure, and the extent of the Burlington-York lineament.

The ordinary Kriging method was chosen based on the following characteristics: the method is linear, exact, and gives an evaluation of uncertainty for interpolated values. For the ordinary Kriging analysis, 817 records of depth to bedrock data from wells (USGS-WRD and NH DES Water Division) and 56 field stations were used (Figure 2a).

A histogram was generated to show the univariate (depth to bedrock) distribution of the dataset (Figure 4a). The histogram indicates that the dataset is unimodal, fairly symmetric, and hence, close to a normal distribution. Nevertheless, the histogram is slightly skewed to the right. Furthermore, a Q-Q plot was generated to compare the distribution of the dataset with a standard normal distribution (Figure 4b). From the Q-Q plot, it can be seen that the distribution is very close to a straight line therefore, no further transformation was applied.

The Trend Analysis tool of the Spatial Analyst, Arc Map 3.2, was used to identify the existence of trends in the N-S and E-W directions (X-Z and X-Z planes of Figure 4c, respectively). Among the identified trends, N-S trend is the strongest. To remove the trends from data and generate the prediction map, a second order-polynomial was applied. Once the Spatial Analyst removed the trends, the statistical analysis was performed on the short range variation component. Before the final prediction map was created, the trends were added back. Therefore, a more accurate surface was produced, because the statistical analysis was performed on the short-range

variation component of the surface or the residuals (Figure 2a).

To evaluate the Kriging configuration, a standard error map was used (Figure 2b). The distribution of the highest values of uncertainty in this map reveals that the strength of the ordinary Kriging analysis resides in the midsection of the study area (Figure 2b). Besides the error map, the effectiveness of the Kriging analysis has been successfully tested in this work by contrasting the outstanding features in the prediction map against mapped bedrock geology (Figure 2c).

Modern visualization software (ArcView V. 6.1, Fledermaus, and Adobe Illustrator CS2) was used to change the orientation and elevation of the light source, set up the vertical exaggeration ratios, and select an appropriate false-color map for the DEM. Manipulation and enhancement of the DEM topography with these programs, dramatically improved the definition of the recorded topographic lineaments (Figure 3). In addition to the methodology described by Gantenbein (2012) for creating shaded relief in DEM by using light sources, animation files were used that resulted in enhanced shadows which aided in the identification of new topographic lineaments and the refinement of the traces of mapped lineaments on DEM. These animation files consisted of a set of images of the DEM covering the study area with sequential illumination settings, constant vertical exaggeration, and same false color map. In each file, the illumination settings were spaced 10º along a 360º span at a constant elevation from the virtual horizon. The topographic exaggeration ratio was constant for each set of images ranging from 1 to 6 in all prepared sets. The lack of a specific animation file, that yielded the best possibility to refine the traces of the topographic lineaments, is due to the low topographic relief to the southeast of the study area, the extensive swamp area, structural grain, and topography dominated by glacial deposits.

To further investigations on the topographic expression of the most prominent topographic lineaments, the Fledermaus computer program was used to generate topographic profiles from merged DEM. In all cases, the profiles are perpendicular to the trace of the lineaments.

A field structural analysis of the rocks affected by the sub-circular structure was conducted in order to confirm its occurrence and to support the observations that were made on the DEM and Kriging analysis. Data sets of the attitude of joints, shear fractures,

and slickenfibers were collected and analyzed from outcrops inside the presumed sub-circular structure boundary and along its periphery. Following the theory outlined by Dyer (1988), the interactive geometry of different sets of systematic joints allows the determination of their relative ages. Thus, for interpretation purposes, we considered each set of joints as a separate jointing episode associated with a stress field. Therefore, results of this structural analysis documents the orientation of the regional stress acting on the study area over time, as inferred from the superposition of multiple joint sets.

Results

Bedrock topography Configuration

In an earlier work, Escamilla-Casas (2001 and 2003) presented bedrock topography configurations of the Exeter and Hampton USGS 7.5-minute quadrangles based on depth to bedrock data estimated from 220 drill logs (USGS-WRD and NH DES Water Division) and outcrop elevations. Those configurations failed to identify the extension of the Merrimack Group, but showed the presence of minor intrusions similar to the Exeter Pluton, which occupies topographic highs. In this paper, a configuration of the bedrock topography covering a larger area and a larger data set is presented.

Figure 2a presents an ordinary Kriging prediction map which subdivides the bedrock topography into twelve contoured classes, ranging from -33.22 m to 61.6 m (-109 ft to 202 ft) relative to present sea level. The highest and lowest topographic values occur in the northwest and southeast portion of the map, respectively, accentuating a prominent contrast in elevation along a southwest – northeast trending sharp boundary.

Map contours delineate a southwest to northeast-trending fabric (Figure 2a), which stands out and coincides with the orientation of most of the bedrock geologic structures identified in the study area (Figure 1a). For instance, the sharp northeast-trending boundary between topographic highs and lows coincides with the trace of a strongly defined northeast-southwest lineament on the DEM that corresponds to the Calef Fault Zone (Figure 1b, 2a, and 2c). In the upper central section of the ordinary Kriging prediction map (Figure 2a) there is a topographic high surrounded by topographic lows suggesting the presence of a circular-shaped structure (Figure 1, 2a,

and 2c). This circular-shaped topographic high, which is also observable in the present topography and the DEM, will be discussed and detailed in a separate section of this paper.

The two lowest topographic values in the ordinary Kriging prediction map are aligned along a northeast-southwest-trending line defining a trough (Figure 2a). The trough is separated by a local high (labeled A in Figure 2c). If the trough corresponds to a geologic structure, such a feature must be deeply imprinted in the bedrock topography. The trend of this deep linear structure probably extends to the southwest, as shown by the topographic low to the south. At present, there is no geologic structure mapped in that specific location, but the Nannie Island Fault Zone (Figure 1) crops out in two nearby locations along strike (Escamilla-Casas, 2003). Furthermore, the presence of abundant Exeter Pluton-like satellitic bodies in the area could be responsible for the discontinuous nature of the inferred trough (Escamilla-Casas, 2001).

Along the southern border of the ordinary Kriging prediction map, two topographic highs occur close to each other (labeled B in Figure 2c). The topographic high to the northwest has an elongated shape and is oriented parallel to the predominant structural grain in the area; the other has a round shape and thus, does not have a preferred orientation. These two features are separated by a narrow topographic low that can be connected along strike with more topographic lows to the northeast, thus defining the trace of a topographic lineament.

Characteristic of the south portion of the study area is the extensive cover of glacial sediments and swamps resulting in limited outcrop exposure, making field geological mapping difficult. Therefore, topographic lineaments and traces of geologic structures are poorly controlled on the surface of these areas due to a low topographic contrast. However, lineaments in the prediction map, although not prominent, assist in the fine-tuning of the traces of shear zones in this area, particularly, the Great Common and Portsmouth fault zones (Figure 1b). The prediction map shows a curved lineament (labeled C in Figure 2c) merging with a northeast-southwest trending lineament at its southern extent (southeast corner, labeled D in Figure 2c). Based on similarity of trends, it is suggested that the curved lineament corresponds to what is known as the Portsmouth Fault Zone, and the north-east-trending lineament is related to the Great Common Fault (Figure 1).

In the northeastern corner of the study area, the ordinary Kriging prediction map shows an incipient northwest-southeast trending lineament that is perpendicular to the predominant Northeast-Southwest fabric (Figure 1, 2a, and 2c). This lineament is not present in the Geologic State Map (Lyons, *et al.*, 1997), but it is consistent with previous interpretations that recognize a NW-SE trending structure in the area (e.g. Ballard and Uchupi, 1972; Birch, 1979; Hussey and Pankiwsky, 1976; Stewart, 1971; among others). McHone (1998) described it as the Burlington – Portsmouth Lineament (Figure 1b and 2c) and interpreted it as being related to the opening of the Atlantic Ocean during the Mesozoic.

Topographic Lineaments

The topographic lineament map that is presented here (Figure 3) includes the analysis of lineaments observed on both, inland topography and high-resolution-bathymetry of the seacoast of New Hampshire. Onshore, the present topography shows a pervasive northwest – southeast structural grain that consists of glacial deposits characterized by discontinuous and elongated topographic highs, and a less persistent northeast – southwest grain. The lineament map shows a strong contrast between topographic highs and lows in the northwest edge of the study area (Figure 3), similar to the prediction map presented in the previous section (Figure 2a). Topographic profiles show that this topographic contrast corresponds to the Calef Fault Zone and consists of a lineament characterized by both, slopes gently dipping to the northwest and slopes steeply dipping to the southeast (Figures 3 and 5).

Sections A-A' and B-B' are northwest to southeast-trending topographic profiles perpendicular to the trace of the Calef Fault Zone (Figure 5). These topographic profiles show that the elevation to the west is higher than to the east, and that the topographic lineament defining the trace of the Calef Fault Zone has, locally, a difference in elevation of approximately 110 meters.

A single, well-defined, west-northwest to east-southeast trending prominent lineament crosscuts the uppermost portion of the study area (Figures 3 and 5). A topographic profile (Section C-C' on Figure 5) perpendicular to the trend of this lineament shows that it consists
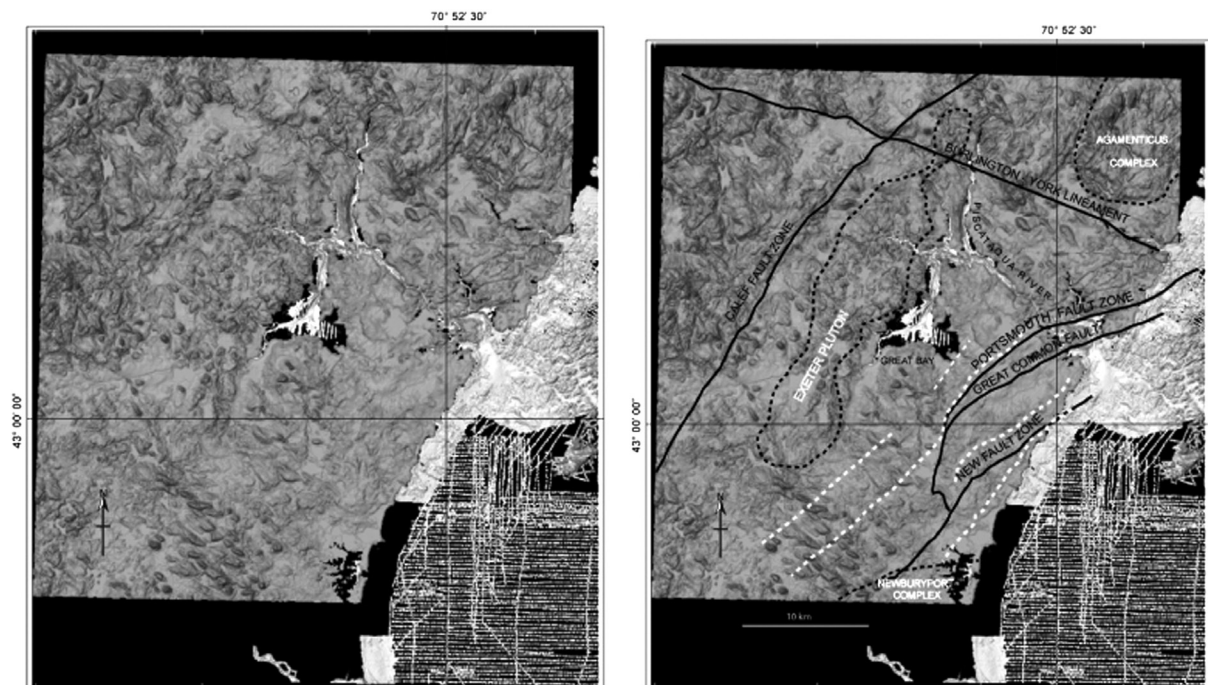
Figure 3. Topographic lineament map interpreted (right) on a mosaic of merged Digital Elevations Models and high-resolution bathymetric soundings of Great Bay, Piscataqua River, and offshore New Hampshire (left). Black dashed lines indicate the location of intrusive bodies and solid lines represent fault zones. White dashed lines indicate the lineaments inferred from the kriging analysis.
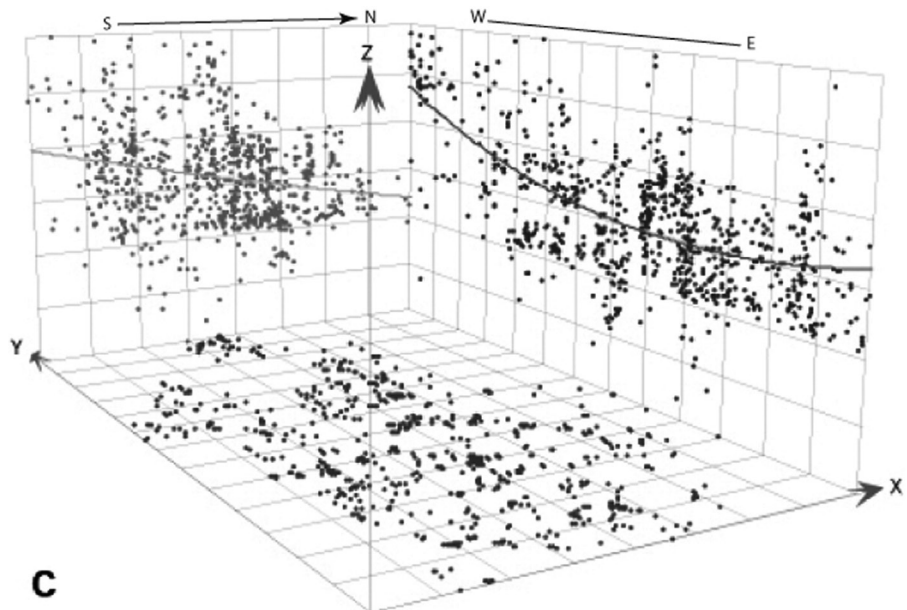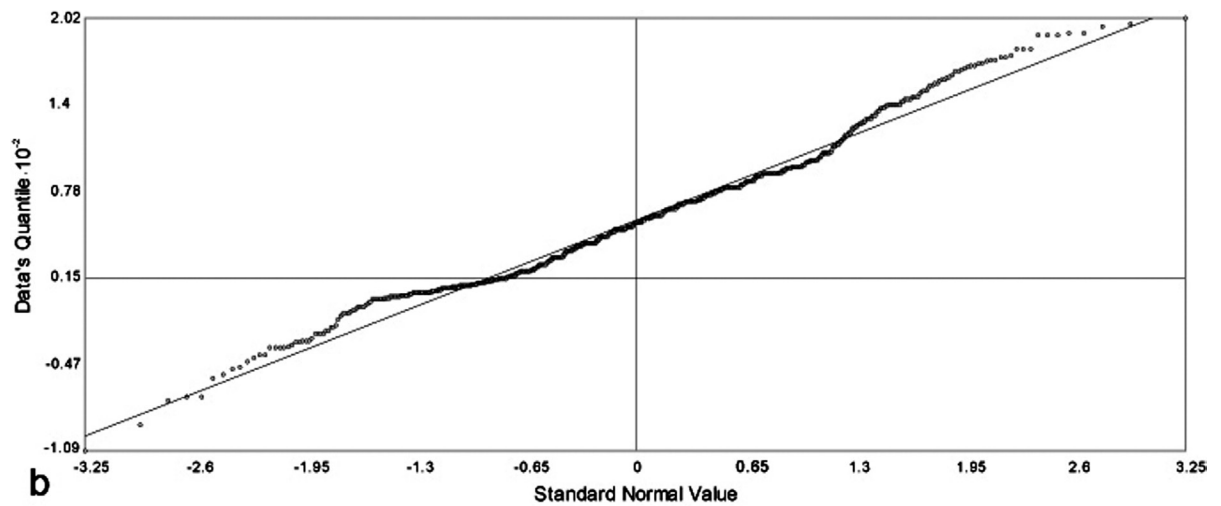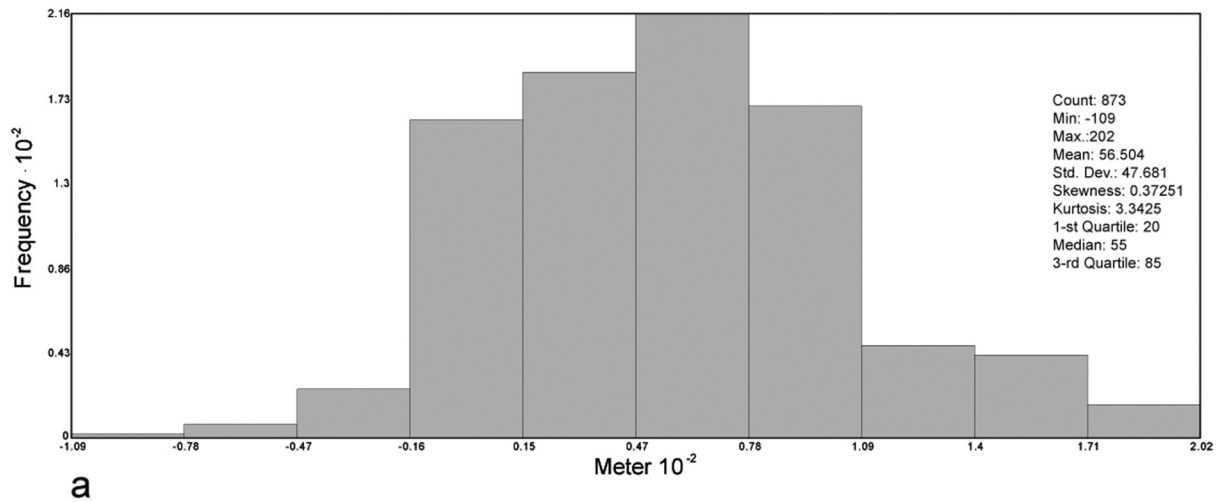
Figure 4. Graphical results of the statistical analysis of the dataset used in the ordinary Kriging analysis. (a) Histogram showing the data distribution. (b) Probability plot (Q-Q Plot) to contrast the distribution of data against the standard normal distribution. (c) Trends in the dataset. The planes X-Z and Y-Z are parallel to the E-W and N-S directions, respectively.

of a deep topographic low with a marked elevation contrast on both sides, where to the north of the lineament the elevation is higher than to the south. This lineament extends to the east offshore as it is observed on the bathymetry, proving that the lineament is imprinted on the seafloor topography (Figures 3, 5 and 6). Based on the lineaments location and trend, it is being suggested that this lineament very likely corresponds to a segment of the Burlington-Portsmouth Lineament described by McHone (1998). Since the trace crosses through York Harbor in Maine instead of Portsmouth, New Hampshire, the authors suggest that Burlington-York Lineament is a more appropriate name.

The stepping up to the northwest en-echelon array of the course of the Piscataqua River can be estimated by Euler Pole analysis (Figure 6), by tracing perpendicular lines to

the long segments of the steps. The resulting plot shows that the lines converge on a sector located close to the center of the topographic high where the Agamenticus Complex crops out. Nevertheless, perpendicular lines to the long segments of the course of Cocheco River define a different Euler Pole.

To the south and southeast regions of the study area, the low topographic relief obscures the identification and tracing of lineaments (Figure 3). Nevertheless, the illumination settings and shadow contrasts of the animation files aided with the identification of lineaments, which can be traced off-shore and connected with those shown on the bathymetry of Portsmouth Harbor (Figure 3). Based on descriptions of previous authors and the trends of the traces identified in Gerrish Island and Newcastle (e.g. Hussey, 1980; Carrigan, 1984), these lineaments likely correspond
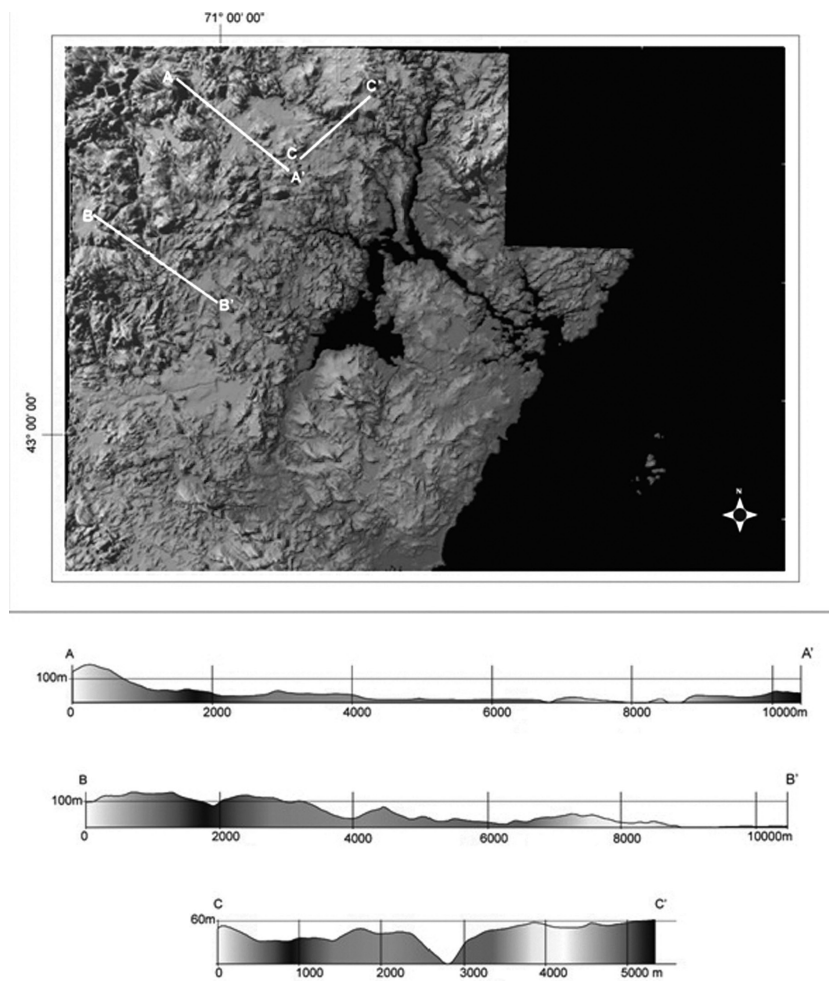
Figure 5. Mosaic of Digital Elevation Models of the study area showing the location of the topographic profiles (see text for explanation). Profiles A-A' and B B' show the difference in elevation along the Calef Fault Zone. Profile C-C' shows a deep topographic feature that corresponds to the Burlington-York topographic lineament.
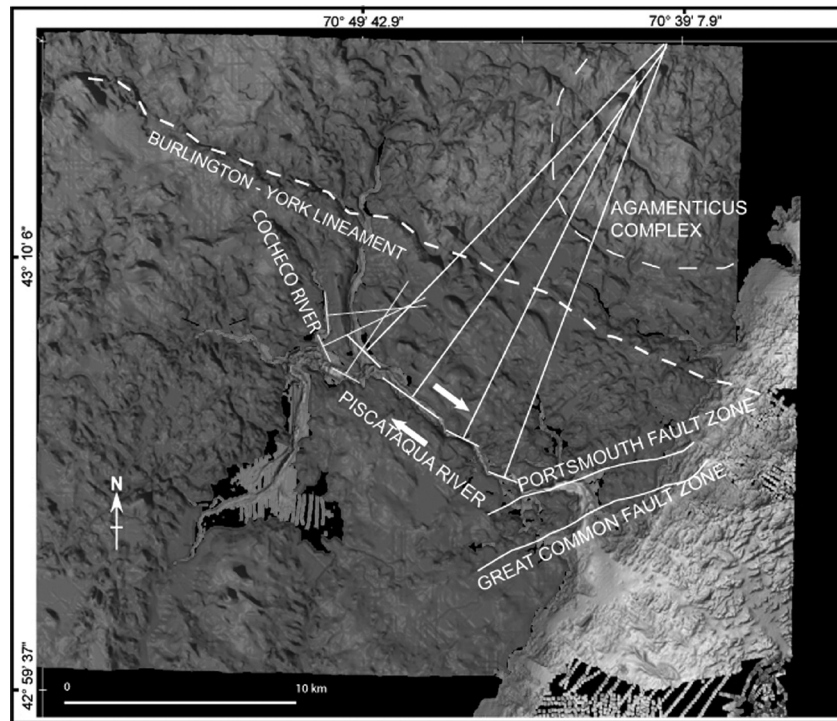
Figure 6. Traces of Euler poles to the long segments of the course of the Piscataqua and Cocheco rivers on a mosaic of merged Digital Elevation Models and bathymetry, converge at different points. However, both poles are close to the center of the Agamenticus Complex. For reference, the traces of the Portsmouth and Great Common fault zones and the Burlington-York lineament are indicated.

to the Portsmouth and Great Common faults zones (Figure 1, Figure 3). However, the inland continuation of these lineaments to the south suggests that these faults eventually merge onshore. This convergence of faults is also consistent with previous interpretation of the fault trends in the area (*e.g.* Lyons et. al., 1997). Escamilla-Casas (2003) published a map showing the traces of the Portsmouth and Great Common Fault Zones merging to the south, which is consistent with the lineament pattern presented in this paper.

A more recent geologic map of the area shows a new fault zone to the south of the Great Common Fault Zone (Bothner *et al.*, 2004). This new fault zone extends to the east and merges with both, the Portsmouth and Great Common fault zones in its southern extent. Lineaments corresponding to these faults continue offshore to the northeast, as shown on the bathymetry of Figure 3. The orientation and location of these lineaments, which are parallel to the trace of the Norumbega Fault System described by Ludman and West (1999), indicate that the new fault, the Great Common, and Portsmouth fault zones, likely belong to the Norumbega Fault System. The authors propose the name

of Hampton Fault Zone for the new fault, as Hampton is the main locality of the fault.

Sub-circular Structure

In plan view, a composite image of the merged digital terrain models and high-resolution bathymetric soundings suggests the presence of a circular structure bounded to the north by the Oyster River, to the south by the Lamprey River, and to the east by the Great Bay (Figures 2c and 7). The perimeter of the identified sub-circular structure is approximately 24 km long and covers an estimated area of 31 km². Its long and short diameters are 7.2 km and 5.5 km long, respectively.

While a radial drainage system is present outside the sub-circular structure's boundary, a deranged pattern developed inside the structure (Figures 7a). The original drainage inside the structure was, very likely altered by fine-grained glacial deposits that formed wetlands and impounded streams resulting in the formation of small lakes. Both, wetlands and small lakes are common features present in the geomorphology of this area.

a)

b)
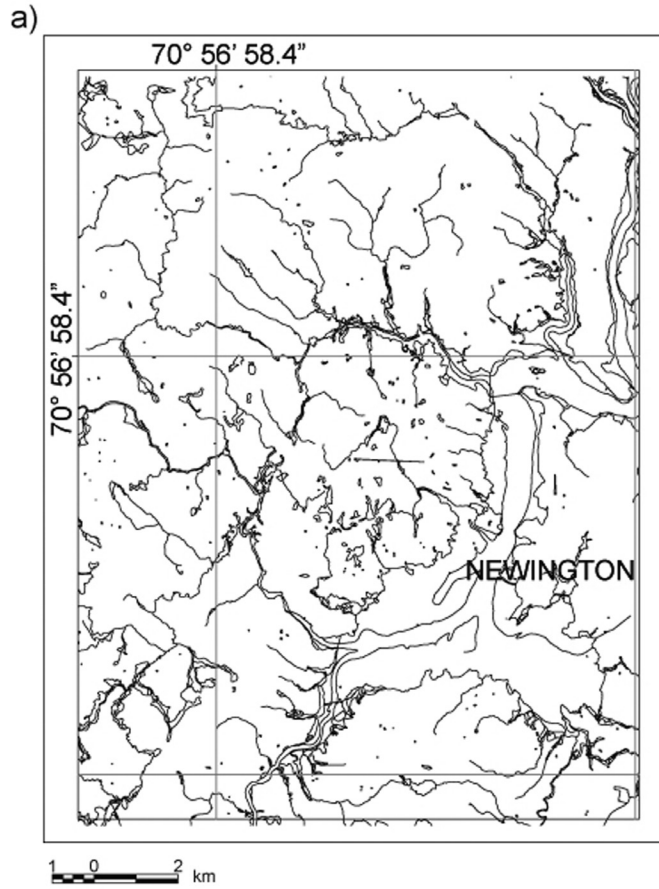
Figure 7. Location of the sub-circular structure on the study area. (a) Radial drainage pattern delineating the periphery of the sub-circular structure. (b) Simplified geologic map of the sub-circular structure showing the joint sampling locations. For each field station, illustrations of the polar plots indicating the dip, dip direction, and relative percentage of occurrence of each joint set are shown. (c) Mosaic of merged Digital Elevation Models and bathymetry of Great Bay showing the location of the three topographic profiles. The topographic profiles delineate the boundaries of the sub-circular structure. A northwest-southeast-trending-normal fault (block down to the northeast) crosscuts the sub-circular structure.
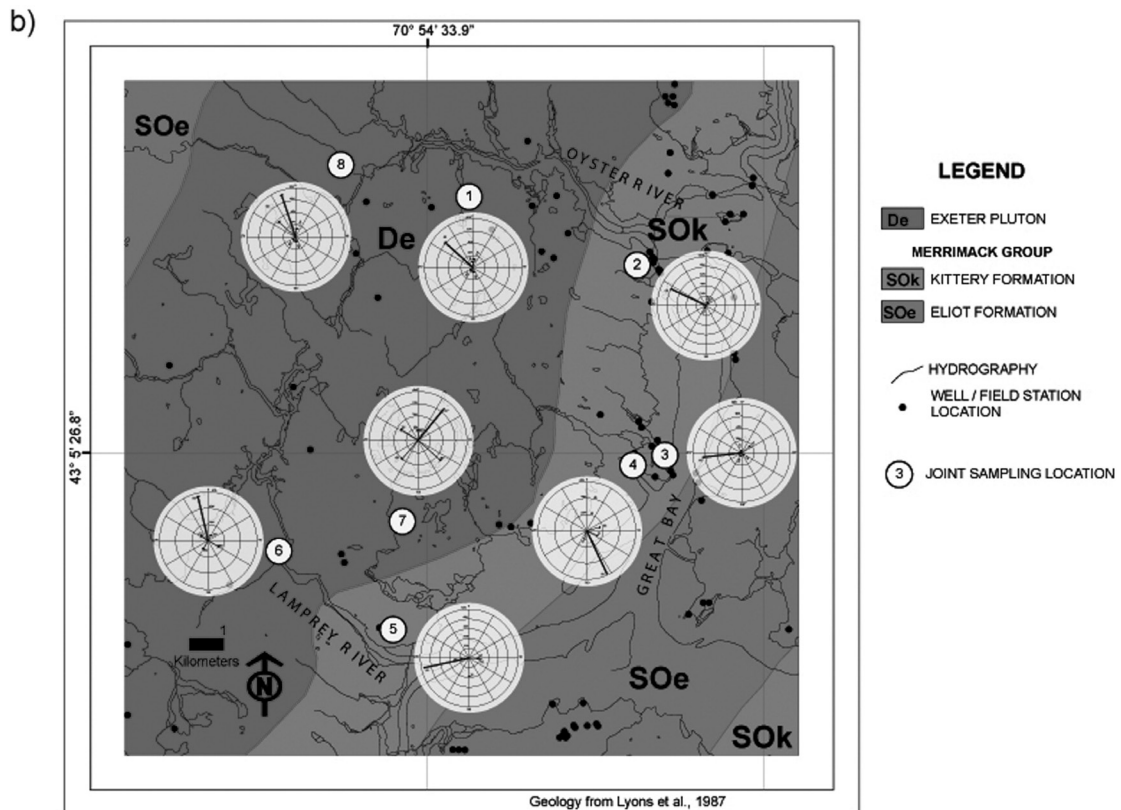
c)
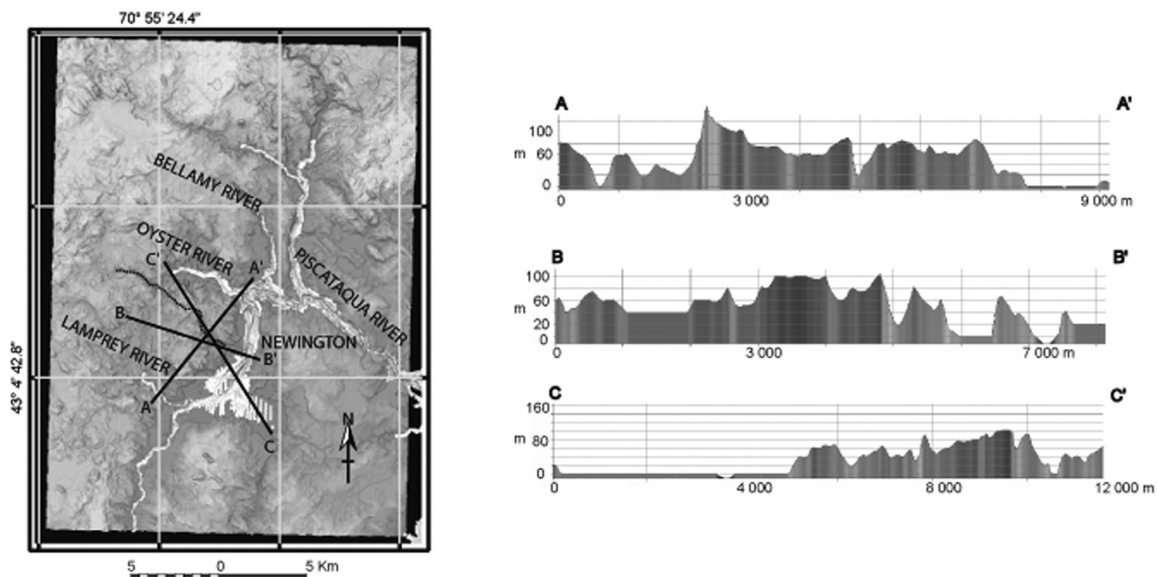
Figure 7. (Continue).

Three topographic profiles (A-A', B-B', and C-C'; Figure 7c) show that the sub-circular structure is elevated with respect to the surrounding rock topography and slightly tilted to the west (Figure 7c). These profiles depict a prominent topographic high close to its center and a deep channel-feature that bounds the structure to the east. The presence of this channel is also revealed by the high-resolution bathymetric soundings of Great Bay and by the Kriging analysis (Figures 8 and 2a, respectively). Moreover, the soundings and Kriging analysis indicate that the channel is imprinted on the bedrock topography, discarding any possible association with soft sediment deposits (see DEM, Figure 3 and bathymetry in Figure 8).

Gravity surveys show that the Exeter Pluton presents a positive Bouger gravity anomaly in excess of 16 Mgals (Bothner, 1974) in the location of the sub-circular structure. Two and three-dimensional models based on gravity surveys in this area also suggest the presence of a 1-3 km thick plutonic body with both, a southeastern steep contact and a shallower northwest contact with the host rock. Additionally, aerial magnetometric surveys revealed anomalies related to the Agamenticus Complex in this region (Bothner and Hussey, 1999; Brooks, 1990).

Within the sub-circular structure, data sets of joints were grouped into two domains, each domain defined upon the dominant rock type where the joints occur (Figure 7b, Table 1).

Domain 1 defined from the intrusive rocks from the Exeter Pluton and Domain 2 defined from the metasediments of the Merrimack Group (Kittery Formation). In both domains, the joint sets present a strong variation in the number of joint planes per meter (joint frequency). However, the orientation of the joints can be grouped into three main sets, regardless of the domain in which they occur. Table 1 summarizes the orientation (predominant strike and dip) of the joint sets observed within each rock domain.

To analyze the variation of joint frequency and its spatial distribution through the study area, a polar plot of the vectors representing the relative percentage of occurrence and the average dip and dip direction of each joint set was created for each joint sampling location (Figure 7b, Table 1). The spatial distribution of the regions with higher joint frequency delineates the areas where prominent structures occur. Crosscutting relationships indicate that rocks of the Merrimack Group are older than the Exeter Pluton, and thus it is inferred that joints older than the age of emplacement of the Exeter Pluton might exist in the Merrimack Group. However, the orientation and crosscutting relationship of joints in each domain permitted the identification and establishment of the joints relative chronology (sequence of formation) to be made and identify the joints that are related to the mechanisms of the intrusion. A comparison of the attitude between joint sets of the two domains also aided with the identification of

Table 1. Summary of the Joint set orientations in each domain.

Sample location	Set 1	Set 2	Set 3	Set 4	Set 5
Exeter Pluton					
1, n = 225	312/55	358/74	177/68	9/65	221/68
7, n = 184	132/80	303/78	39/65	221/68	358/80
6, n = 240	347/67	303/80	122/65	30/65	210/70
8, n = 245	305/65	132/80	30/60	221/70	312/75
Merrimack Group					
2, n = 285	62/32	215/55	295/80	58/76	N.D.
3, n = 270	264/66	202/84	22/16	132/65	337/52
4, n = 180	155/86	198/21	114/12	75/46	N.D
5, n = 305	258/83	180/20	96/37	263/80	118/88

Notes:
- Values indicate the average dip direction (azimuth) and dip angle (degrees) of each joint set.
- Refer to Figure 6b for locations.
- n = sample population.

the overall relative chronology. Joint sets were investigated at eight field stations (Figure 7b, Table 1), four of them located within the Merrimack Group and four within the Exeter Pluton.

At least five distinct sets of joints are present in the rocks of the Exeter Pluton (Domain 1, Joint Sampling Locations 1, 6, 7, and 8, on Figure 7b; Table 1). At Location 1, the oldest set of joints dips 74° to the northwest and it is crosscut by a conjugate set of joints dipping 65° to the northeast and 68° to the south. A second set of joints is present dipping 68° to the southwest; its relative age with respect to the previously described sets is uncertain. A third set of joint planes (the youngest) dips 55° to the northwest and has the highest frequency.

Figure 8. Image generated from high-resolution bathymetric soundings of Great Bay to the east of the sub-circular structure. The image shows the presence of dioritic dikes, which are also traceable on the surface and illustrates the inferred fault-related channel that bounds the sub-circular structure to the east.
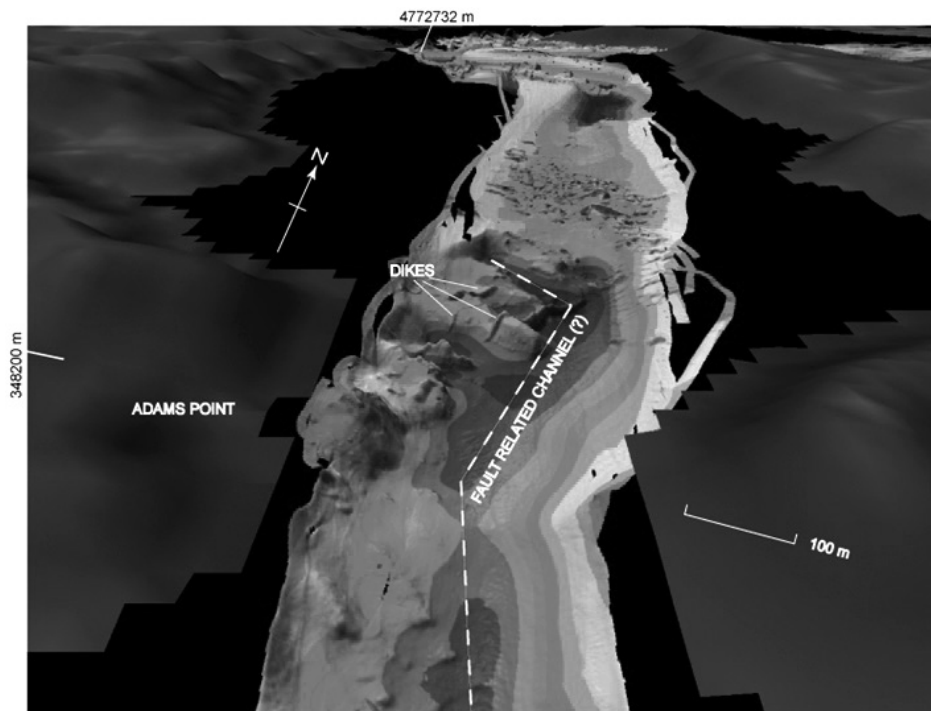
At location 6, two main sets of conjugate joints have been observed. Joints that belong to the older set dip 65° to the northeast and 70° to the southeast, while a younger joint set dips 67° to the northwest and 65° to the southeast. At this location, the third and youngest joint set dips 80° to the northwest, and has the highest joint frequency. At location 6, a few joint surfaces contain slickenfibers that indicate a south block down vertical displacement. At Location 7, the oldest joint set dips 80° to the northwest and is crosscut by two conjugate sets: one with planes dipping 65° to the northeast and the other dipping 68° to the southwest. The youngest joint set dips 78° to the northwest and 80° to the southeast. At Location 8, the oldest conjugate set of joints dips 60° to the northeast and 70° to the southwest. A younger conjugate set dips 75° to the northwest and 80° to the southeast. The set with highest frequency of planes is the youngest in this location and dips 65° to the northwest.

Analysis of joints from locations 1, 6, 7, and 8 (Figure 7b) indicates that the Exeter Pluton has two conjugate sets of joints: one set dipping to the northeast and to the southwest, and a younger set dipping to the northwest and to the southeast. Following the interpretation of Dyer (1988), the geometry of these conjugate joint sets suggests that during their formation, the principal tectonic stress was vertically oriented. In locations 5, 6, and 8 (Figure 7b) joint planes with dip directions tangential to the circular structure have the highest frequency. Locations with high joint frequency around the elevated sub-circular structure indicate that this structure was significantly affected by brittle deformation, and shows the presence of other structures, for instance, a fault that bisects the sub-circular structure (Figure 7c). In all joint sets within the Exeter Pluton, the youngest set has the highest frequency of planes (Sample Location 1).

Each field station in the Merrimack Group contains at least four sets of joints (Joint Sampling Locations 2, 3, 4, and 5 of Figure 7b; Table 1). Rocks in field stations of the Merrimack Group are characterized by higher joint frequency than the rocks of the Exeter Pluton. At location 2, the oldest joint set dips 76° to the northeast and it is crosscut by a conjugate set of joints dipping 32° to the northeast and 55° to the southwest. Here, the youngest set has the highest frequency of joints, with planes steeply dipping to the southwest. On these joint planes, slickenfibers indicate a north block down vertical displacement. At location 3, the oldest joint set dips 16° to the northeast and with a conjugate set dipping

84° to the southwest. This conjugate set is crosscut by two sets of joints, one dipping 52° to the northwest and the younger set dips 65° to the southeast. The youngest joint set contain the highest frequency of joint planes, is characterized by planes dipping 66° to the west, and contain slickenfibers that indicate an east-block-up vertical displacement. At location 4, the oldest conjugate set of joints dip 46° to the northeast and 21° to the southwest and are crosscut by a joint set that dips gently to the southwest (12°). The highest frequency of joints corresponds to the youngest joint set with planes dipping 80° to the southeast. These planes also contain slickenfibers indicating vertical (north block up) and horizontal (to the west) displacements. At location 5, the oldest set consists of conjugate planes that dip 37° to the east and 80° to the west, and are crosscut by a younger conjugate joint set characterized by sub-vertical planes. The two previously described conjugate sets are crosscut by a set of joints with planes that dip gently (20°) to the south. The youngest joint set at location 5, dips steeply to the southwest and have the highest joint frequency. Slickenfibers are observed on the planes of this youngest set, but cannot be used as kinematic indicators at this location.

Analysis of the general orientation of joint sets from locations 2, 3, 4, and 5 (Figure 7b; Table 1) indicates that conjugate sets of joints have variable orientations in the Merrimack Group, and thus, the interpretation of the stress fields is uncertain in this unit. At each location 2, 3, and 4, (Figure 7b and Table 1) the oldest conjugate set of joints have planes that variably dip to the northeast and to the southwest. The variation in the orientation of these joint planes is likely influenced by the anisotropy inherent to bedding and the Acadian folding of the meta-sediments. Furthermore, it is likely that the Exeter Pluton fractured the host rocks during or after its emplacement, producing most of the joint sets. In all locations within the Merrimack Group, the strike of the younger set of joints is tangent to the presumed sub-circular structure and the slickenfibers on the joint planes indicate vertical displacement. This is consistent with the vertically oriented tectonic stress that is interpreted from the joint orientation present in the rocks of the Exeter Pluton. Hence, both, the orientations of joint planes and kinematic indications from slickenfibers of the youngest set of joints in both domains, support the hypothesis of the presence of a sub-circular structure bounded by a brittle fault with vertical motion. The variability of sense of vertical movement, inferred from kinematic indicators preserved

on joint planes in both domains, suggests reactivation of the vertical displacement along the fault with respect to its host rock at different time.

Tectonic Model

The tectonic interpretation of the geological evolution of the area, takes into consideration that the emplacement of the pluton, which is presumably underneath the circular structure, occurred under an extensional regime that prevailed during the Mesozoic. Thus, such intrusion is responsible for influencing the evolution of Great Bay tidal estuary and the geometry of the course of the Piscataqua and Cocheco rivers in times of the opening of the North Atlantic Ocean. This innovative extensional model contains the following stages:

First, during the Mesozoic, the Agamenticus Complex intruded rocks of the Merrimack Group. Due to the intrusion, the surrounding crust was subjected to tensional stresses (Figure 9a). As a result, and according to the Euler Poles analysis, the breakup of the crust produced a set of fractures in an en-echelon array that later was occupied by the drainage system that led to the formation of the present course of the Piscataqua River. The en-echelon array implies breakup resolved by pull-apart and strike slip faulting, produced by the motion of a rigid segment of the crust on the curved surface of the Earth about an approximately rotation pole or the Euler pole. The presence of the preexisting Exeter Pluton may have refracted the intrusion-related fracture trend forming the branch that corresponds to the present course of the Cocheco River.

Second, it is probable that an Agamenticus-like igneous body was emplaced in the middle section of the Exeter Pluton (Figure 9b). Although this ascendant pluton did not have the buoyancy to remove the overlying rocks completely, its rising vertical movement imprinted brittle deformation on the Exeter Pluton and nearby rocks of the Merrimack Group. After cooling, the intrusive body very likely collapsed moving vertically again. This resulted in the ambiguous sense of vertical movement that is inferred from the slickenfibers observed on the joint planes. From the structural analysis and the lack of other structures, it is inferred that the concentration of brittle deformation related to each vertical movement occurred along the fault that surrounds the sub-circular structure. Based on gravity surveys, the 1-3 km thick intrusive body may be responsible
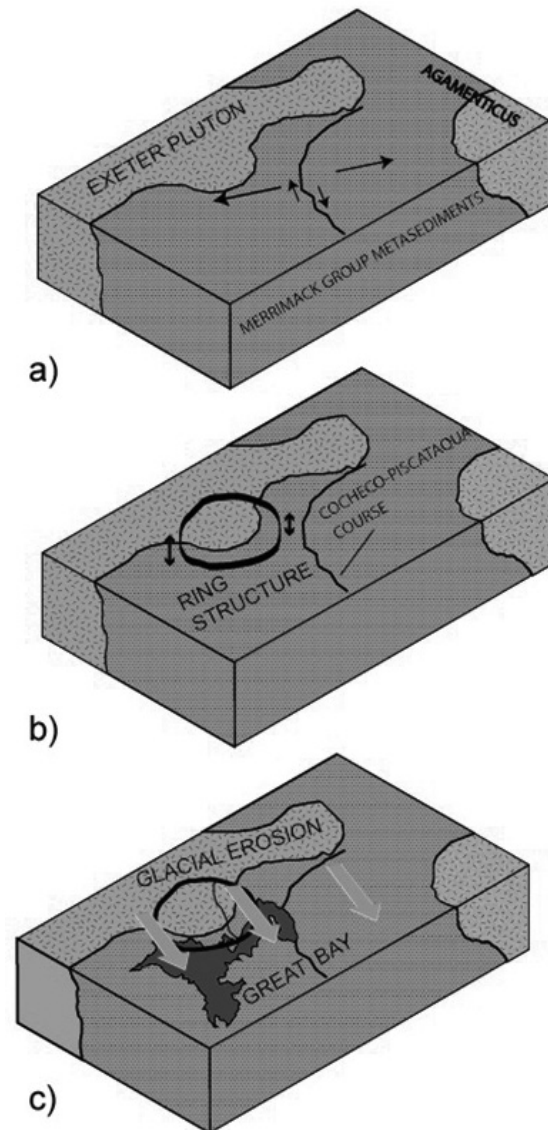
Figure 9. Tectonic model proposed in this study. (a) The initial stage in this model suggests that the emplacement of the Agamenticus Complex generated the extensional regime. The extension produced a set of fractures that defined the trace of the present course of the Piscataqua River. The presence of the preexisting Exeter Pluton refracted the trace of the extension fractures generating the trace of the present Cocheco River. (b) The emplacement of an intrusive body, probably associated with the Agamenticus Complex, did not have the buoyancy to completely remove the Exeter Pluton and Merrimack Group cap rock. During the emplacement of this intrusive body, a rising movement was followed by subsequent collapse after the cooling stage. As a result of this vertical movement, brittle deformation was imprinted on the host rocks. (c) Finally, glacial erosion of the softer metasedimentary Merrimack Group rocks shaped the present Great Bay.

for the positive Bouger anomaly of the Exeter Pluton; its correlation with the Agamenticus Complex is based on aerial magnetometry.

The formation of the topographic low near the Exeter Pluton, and subsequent events (intrusion of plutonic bodies and youngest imprint of brittle deformation), was very likely part of the initial stages of formation of the actual Great Bay during the lower to mid Paleozoic. The presence of northwest to southeast trending drumlins and several other distinctive glacial deposits indicate that glacial erosion was intense in the lower east portion of Great Bay during the Quaternary (Fig. 9c). The glacial erosion was particularly strong where the less competent metasedimentary rocks of the Merrimack Group are predominant. Consistent with a glacial origin, the lower east branch of Great Bay is oriented northwest to southeast paralleling the general trend of glacial deposits in the study area.

Discusion

The use of DEMs facilitates the interpretation of the bedrock geology in areas of poor rock exposure in the seacoast area of New Hampshire. In this study, the results of the analysis of the lineaments observed on mosaics of merged DEMs and high-resolution bathymetric soundings were used to refine the traces of lineaments, which mostly correlate to previously mapped fault zones. To support the interpretation of the traces and the identification of a sub-circular structure nearby the Exeter Pluton, a prediction map based on x-y-z data (location coordinates and borehole depth to bedrock elevations) of the bedrock topography was constructed and supplemented with information from current geologic maps.

In the middle portion of the Exeter Pluton, the present topography defines a radial drainage pattern, and the bedrock topography prediction map shows a topographic high that delineates a sub-circular structure. In this location, field analysis of brittle structures confirms the presence of a circular fault that bounds the topographic high.

The structural analysis of slickenfibers on jointed planes inside the sub-circular structure, suggests that the structure was formed due to vertical displacements that is hypothesized to be related to the emplacement of an intrusive body that presently is not exposed. The mechanisms of emplacement of the intrusive body jointed and faulted (extensional regime) the overlaying host Exeter Pluton and Merrimack Group rocks, but was not strong

enough to remove the cap. The existence of the sub-circular structure is consistent with the presence of structures associated with plutonic bodies in the bedrock of New Hampshire. Furthermore, the proximity of the Agamenticus Complex to the proposed sub-circular structure also supports its likely association with the plutonism that prevailed during the Mesozoic.

In the proposed tectonic model, the fault that surrounds the sub-circular structure was responsible for the formation of Great Bay. Also, according to this model, Great Bay was a topographic low from which a northeast-southwest trending rivers formed during the Quaternary. The river was enlarged and reshaped as a result of glacial erosion and sedimentation processes.

Euler Pole analysis of the course of the Piscataqua River suggests a right-lateral extensional regime that is consistent with its en-echelon pattern, which is very likely related to the emplacement of the Mesozoic Agamenticus Complex during the opening of the Atlantic Ocean. For the Euler Pole analysis, it is assumed that during the emplacement of the Agamenticus Complex, some rotation of the rigid crust occurred and originated the right lateral shear. The course of York River, which is near the Agamenticus Complex, might not have been affected by the intrusion because it is a younger feature associated with the Burlington-York Lineament. It is likely that the current topography is also affected by the interaction of the Devonian Webhannet Pluton with the Mesozoic Agamenticus Complex.

Conclusions

The pervasive northeast-southwest structural grain of the bedrock geology of Seacoast New Hampshire and southwestern Maine is evident on both mosaics of DEMs of inland topography merged with offshore high-resolution bathymetry, and on a configuration of the bedrock topography based on Kriging analysis.

On bedrock (inferred) and surface topographies, lineaments were identified that are associated with the trace of fault zones that likely belong to the Norumbega Fault System. Computer animation files with images of the topography facilitated the identification of lineaments and the refinement of traces of presently mapped faults. High-resolution-bathymetry of the seafloor aided in the identification of the trace of the lineaments and supports the continuation of the fault trace offshore.

The use of modern visualization software and topographic profiles helped to determine that the Calef Fault Zone and the Burlington-Portsmouth Lineament are topographic features deeply imprinted on bedrock topography. Moreover, Geographic Information Systems, topographic data, and field structural data from rocks of the Merrimack Group and Exeter Pluton, aided in the identification and delineation of a sub-circular structure. It is hypothesized that the sub-circular structure formed as a result of a failed extrusion of a plutonic body associated with nearby Mesozoic plutonic bodies. It is interpreted that the failed extrusion imprinted brittle deformation on the host rock and produced the subsequent tilting of the rock cap triggering the formation of the Great Bay estuary that was subsequently reshaped by glacial erosion. Similarly, the extension and breakup of the crust during the intrusion of the Agamenticus Pluton determined the trace of the present course of the Cocheco and Piscataqua rivers.

These observations of brittle structures, surface topographic features, high resolution bathymetry, and predicted bedrock topography lead to the postulation of a tectonic model that explains the origin and formation of the Piscataqua and Cocheco rivers, and the Great Bay estuary.

Aknowledgements

References

Havskov J., Singh S.K., Nava E., Dominguez T., Rodriguez M., 1983, Playa Azul, Michoacán, Mexico earthquake of 25 October, 1981 (Ms = 7.3), *Bull. Seism. Soc.*, 73, 2, 449-458.

Arlegui L.E., Soriano M.A., 1998, Characterizing lineaments from satellite images and field studies in the central Ebro basin (NE Spain). *International Journal of Remote Sensing,* 19, 16, 3169-3185.

Ballard R.D., Uchupi E., 1972, Carboniferous and Triassic rifting: a preliminary outline of the tectonic history of the Gulf of Maine. *Geological Society of America Bulletin*, 83, 2285-2302.

Billings M.P., 1956, The geology of New Hampshire; Part 2, bedrock geology: Concord, N. H., *New Hampshire State Planning and Development Commission*, 200pp.

Birch F.S., 1979, Magnetic Fabric of the Exeter Pluton, New Hampshire. *Journal of Geophysical Research*, 84, B3, 1129-1137.

Birch F.S., 1984, Geophysical Survey of Bedrock on the Inner Continental Shelf of New Hampshire. *Northeastern Geology*, 6, 2, 92-102.

Bothner W.A., 1974. Gravity study of the Exeter pluton, southeastern New Hampshire. *Geological Society of America Bulletin*, 85, 51-56.

Bothner W.A., Boudette E.L., Fagan T.J., Gaudette H.E., Laird J., Olzewski W.J., 1984, Geologic framework of the Massabesic anticlinorium and the Merrimack trough, southeastern New Hampshire. *New England Intercollegiate Geological Conference* (76th Annual Meeting, Danvers, Mass., Oct. 12-14, 1984, Salem, Mass., Salem State College, Department of Geological Sciences), 186-206.

Bothner W.A., Hussey A.M., II, 1999, Norumbega Connections: Casco Bay, Maine to Massachusetts? *in* Ludman, A.; West, D.P., Jr. (eds.), Norumbega Fault System of the Northern Appalachians. Boulder, Colorado. *Geological Society of America Special Paper,* 331, 59-72.

Bothner W.A., Laird J., Escamilla Casas J.C., Kerwin C.M., Schulz J., Loveless J.P., 2004, EDMAPS/newmaps in southeastern New Hampshire. *Geological Society of America Abstracts with Programs*, 36, 57.

Bothner W.A., Blackburn T., Bowring S., Buchwaldt R., Hussey A.M., II, 2008, Temporal Constraints on Paleozoic Plutonism in Southwestern Maine and Southeastern New Hampshire: revisions and Implications. *Geological Society of America Abstracts with Programs*, 41, 3, 32.

Bradley D.C., Tucker R.D., Lux D.R., Harris A.G., McGregor D.C., 2000, *Migration of the Acadian Orogen and foreland basin across the Northern Appalachians of Maine and*

adjacent areas: U. S. Geological Survey Professional Paper Report, 1624: 55 pp.

Brooks J.A., 1990, The petrogenesis of the Agamenticus Complex and Late Paleozoic and Mesozoic tectonics in New England: University of New Hampshire, Ph.D. thesis, 317 pp.

Carrigan J.A., 1984, Geology of the Rye Formation, New Castle Island and adjacent parts of Portsmouth Harbor, New Hampshire: University of New Hampshire, M.S. Thesis, 128 pp.

Clark S.F., Jr. Moore R.B., Ferguson E.W., Picard M.Z., 1996, *Criteria and Methods for Fracture-Trace Analysis of the New Hampshire Bedrock Aquifer*: USGS- Open-File Report, 96-479, 12 pp.

Crider J.G., Peacock D.C.P., 2004, Initiation of brittle faults in the upper crust: a review of field observations. *Journal of Structural Geology*, 26, 691-707.

Cutter J.R., 2005, Seafloor Habitat Characterization, Classification, and Maps for the Lower Pscataqua River Estuary: University of New Hampshire, Ph.D. Thesis, 291 p.

Duncan R.A., 1984, Age-progressive volcanism in the New England Seamounts and the opening of the central Atlantic Ocean. *Journal of Geophysical Research*, 89, 12, 9980-99990.

Dyer R., 1988, Using joint interactions to estimate paleostress ratios. *Journal of Structural Geology*, 10, 685-699.

Escamilla-Casas J.C., 2001, Geology of the Exeter and Hampton 71/2' Quadrangles, SE New Hampshire. *Geological Society of America Abstracts with Programs*, 33, 1, 49.

Escamilla-Casas J.C., 2003, Bedrock geology of the seacoast region of New Hampshire. USA: University of New Hampshire, Ph.D. Thesis. 218 pp.

Ferguson E.W., Clark S.F., Jr. Picard M.Z., Moore R.B., 1997, *Lineament* Map of Area 1 of the New Hampshire Bedrock Aquifer Assessment, scale 1:48,000: USGS Open-File Report 97-762.

Ferguson E.W., 1997, *Lineament Map of Area 3 of the New Hampshire Bedrock Aquifer Assessment, scale 1:48,000*: USGS Open-File Report 97-762.

Fargo T.R., Bothner W.A., 1995, Polydeformation in the Merrimack Group, southeastern New Hampshire and southwestern Maine, *in* Hussey A.M.II, and Johnson, R.A. (eds.), *Guidebook to field trips in southern Maine and adjacent New Hampshire*. New England Intercollegiate Geological Conference Guidebook, 87, 15-28.

Gaudette H.E., Kovach A., Hussey A.M., 1982, Ages of some intrusive rocks of southern Maine, U.S.A. *Canadian Journal of Earth Sciences*, 19, 1350-1357.

Gantenbein C., 2012, Creating Shaded Relief for Geologic Mapping using Multiple Light Sources, *Digital Mapping Techniques '10 – Workshop Proceedings*, USGS Open File Report 2012-1171, http://pubs.usgs.gov/of/2012/1172/.

GRANIT-UNH, NH GRANIT, New Hampshire Statewide GIS Clearinghouse, 2014, www.granit.unh.edu.

Hill R.I., 1991, Starting plumes and continental break-up. *Earth and Planetary Science Letters*, 104, 2-4, 398-416.

Hubbard M.S., West D.P., Jr. Ludman A., Guidotti C.V., Lux D.R., 1995, The Norumbega fault zone, Maine: a mid- to shallow-level crustal section within a transcurrent shear zone. *Atlantic Geology*, 31, 109-116.

Hussey A.M. II, 1968, Stratigraphy and structure of southwestern Maine. In: Zen E-an, White, W. S., Hadley, J. B., and Thompson, J. B., (eds.), *Studies in Appalachian Geology-northern and Maritime*: Interscience, NY, 291-301.

Hussey A.M. II, Pankiwskyj K.A., 1976, *Preliminary geologic map of southwestern Maine*: Maine Geological Society, Open-file Map 1976-1.

Hussey A.M. II, 1980, The Rye Formation of Gerrish Island, Kittery, Maine: A reinterpretation. *The Maine Geologist*, 6, 2, 2-3.

Hussey A.M. II, 1985,*The bedrock geology of Bath and Portland 2-degree map sheets, Maine*: Maine Geological Survey, Open-File Report No. 85-87, 82 pp.

Hussey A.M. II, Bothner W.A., 1993, Geology of the coastal lithotectonic belt, SW Maine and

SE New Hampshire. *In:* Cheney, J.T., and Hepburn, J.C, (eds.) *Field trip guidebook for the northeastern United States: Amherst, University of Massachusetts*. Department of Geology and Geography Contribution, 67, pp. K1-K19.

Hussey A.M., Bothner W.A., Thompson P.J., 2007, New interpretation of the Merrimack Group in southwestern Maine and Southeastern New Hampshire. *Geological Society of America Abstracts with Programs*, 39, 1, p. 76.

Hussey A.M., Bothner W.A., Aleinikoff J., 2010, The Tectono-stratigraphic framework and evolution of southwestern Maine and southeastern New Hampshire. *Geological Society of America Memoir*, 206, 205-230.

Katz F.J., 1917, Stratigraphy in southwestern Maine and southern New Hampshire*. USGS Professional Paper*, 108, 165-177.

Lattman L.H., 1958, Technique of mapping geologic fracture traces and lineaments on aerial photographs. *Photogrammetric Engineering and Remote Sensing*, 24, 4, 568-576.

Ludman A., 1999, High-resolution digital terrain models, free for the making: an example from eastern and east-central Maine. *Geological Society of America, Abstracts with Programs,* 31, 7,111.

Ludman A., West D.P. Jr., eds., 1999, The Norumbega fault system of the Northern Appalachians: *Geological Society of America Special Paper 331*, 199 pp.

Lyons J.B., Bothner W.A., Moench R.H., Thompson J.B. Jr., 1997, *Bedrock Geologic Map of New Hampshire*: U.S. Geological Survey State Map Series, scales 1:250,000 and 1:500,000.

McHone J.G., 2000, Non-plume magmatism and rifting during the opening of the Central Atlantic Ocean. *Tectonophysics*, 316, 3-4, 287-296.

McHone J.G., 1996, Constraints on the mantle plume model for the Mesozoic alkaline intrusions in northeastern North America. *The Canadian Mineralogist*, 34, 325-334.

McHone J.G., 1988, Tectonic and paleostress patterns of Mesozoic intrusions in eastern North America. In: Manspeizer, W. (ed.), *Triassic-Jurassic rifting*. Elsevier

Developments in Geotectonics. New York, Elsevier, 22, Part B, 607-620.

McHone J.G., Butler J.R., 1984, Mesozoic igneous provinces of New England and the opening of the North Atlantic Ocean. *Geological Society of America Bulletin*, 95, 757-765.

Novotny R.F., 1969, *The geology of the seacoast region, New Hampshire*. New Hampshire Department of Resources and Economic Development, 46 p.

Osberg P.H., Hussey A.M. II, Boone G.M., 1985, *Bedrock geologic map of Maine.* Augusta, Maine Geological Survey, scale: 1:500, 000.

Pollard D.D., Aydin A., 1988, Progress in understanding jointing over the past century. *Geological Society of America Bulletin*, 100, 1181-1204.

Rasco H.P., Warner T.A., 1999, Multiple data set integration and GIS techniques used to investigate linear structural controls in the southern Powder River basin. *Geological Society of America Abstracts with Programs*, 31, 7, 176.

Riley D.N., Barton M., Dalton-Sorrel C., 1999, Preliminary assessment of the geological mapping in eastern Maine, USA using Shuttle Imaging Radar (SIR-C). *Geological Society of America Abstracts with Programs*, 31, 7, 176.

Schulz J.E., 2004, Metamorphic Petrology and Structural Implications of the calcareous (Unnamed) Member of the Berwick Formation Within the Epping 7.5 Minute Quadrangle Southeast, New Hampshire: University of New Hampshire, M. Sc. Thesis, 216pp.

Shake S.N., McHone J.G., 1987, Topographic lineaments and their geologic significance in central New England and adjacent New York. *Northeastern Geology*, 9, 3, 120-128.

Stewart G.W., 1971, *Occurrence and characteristics of fractures in crystalline rocks of southeastern New Hampshire and their relationship to yield of drilled water wells*: Proj. Rep. A-016-NH, Water Resources Research Center, Durham, N.H.

Swanson M.T., 1982, Preliminary model for an early transform history in central Atlantic rifting. *Geology*, 10, 8, 317-320.

USGS-DEM Resources, GeoCommunity, 2014, www.data.geocomm.com/dem/.

Van der Pluijm B.A, Johnson R.J.E., Van der Voo R., 1993, Paleogeography, accretionary history, and tectonic scenario: a working hypothesis for the Ordovician and Silurian evolution of the Northern Appalachians. In: Roy, D.C., and Skehan, J.W. (eds.), The Acadian Orogeny; recent studies in New England, Maritime Canada, and the autochthonous foreland: *Geological Society of America - Special Paper*, 275, pp.27-40.

West D.P. Jr., Roden-Tice M.K., 2003, Late Cretaceous reactivation of the Norumbega fault zone, Maine: Evidence from apatite fission-track ages. *Geology*, 31, 7, 649-652.

White R., McKenzie D., 1989, Magmatism at rift zones: The generation of volcanic continental margins and flood basalts: *Journal of Geophysical Research*, 94, 7685-7729.

Wintsch R.P., Aleinikoff J.N., Walsh G.J., Bothner W.A., Hussey A.M., Fanning C.M., 2007, SHRIMP U-Pb evidence for a Late Silurian age of metasedimentary rocks in the Merrimack Group and Putnam-Nashoba Terranes, eastern New England. *American Journal of Science*, 307, 119-167.

An Innovative Tool for Effectively Applying Highly Parallelized Hardware To Problems of Elasticity

Ismael Herrera[*] and Iván Contreras

Resumen

En la actualidad los métodos de descomposición de dominio (DDM, por sus siglas en inglés) más eficientes como instrumento de paralelización son los métodos sin traslape (non-overlapping). Su alta eficiencia es debida a la independencia muy significativa que logran los problemas locales planteados en subdominios que no se traslapan. Sin embargo, los métodos de discretización estándar que habían usado hasta ahora los DDM, aún los sin traslape, utilizan sistemas de nodos en que algunos de ellos son compartidos por varios subdominios de la descomposición. Ésta es una característica limitativa del estado del arte actual de este tipo de procedimientos y, muy probablemente, mayores niveles de independencia de los problemas locales podrían lograrse si se le eliminara. I. Herrera y sus colaboradores han atacado este problema, para lo cual han introducido una nueva manera de formular los DDM que no tiene esta limitación: el método DVS. Un rasgo conspicuo de esta forma de abordar la descomposición de dominio es que se utiliza un método nuevo de discretización de las EDPs, también introducido en la línea de investigación a la que pertenece este artículo, conocido con el nombre de 'discretización sin traslape' (non-overlapping discretization), en el cual cada nodo de la discretización pertenece a uno y solo uno de los subdominios de la descomposición del dominio. Aunque los métodos DVS ya se han desarrollado considerablemente, para que rindan frutos plenamente es indispensable contar con códigos que permitan su implementación eficiente. A eso precisamente está dedicado este artículo: presentar y poner a prueba software de tales características. El software aquí reportado muestra que los algoritmos DVS son los más adecuados para desarrollar software que permita la aplicación efectiva de equipo de cómputo avanzado, altamente en paralelo, a la solución de las ecuaciones diferenciales parciales de los modelos de la ciencia y la ingeniería. Aunque el software que aquí se presenta trata específicamente problemas de elasticidad lineal, los algoritmos DVS son muy eclécticos y pueden ser aplicados a una gran diversidad de ecuaciones diferenciales parciales, después de que las mismas han sido discretizadas. Además, ahora se continúa con trabajo adicional de investigación para desarrollar códigos de propósito general basados en los algoritmos DVS.

Palabras clave: Software en paralelo para EDPs, procesamiento en paralelo de elasticidad, cómputo de alto rendimiento, HPC, elasticidad estática, cómputo en paralelo, métodos de descomposición de dominio.

I. Herrera[*]
Instituto de Geofísica
Universidad Nacional Autónoma de México
Circuito de la Investigación Científica s/n
Ciudad Universitaria
Delegación Coyoacán, 04510
México D.F., México
*Corresponding autor: iherrerarevilla@gmail.com

I. Contreras
Posgrado en Ciencia e Ingeniería de la Computación
Universidad Nacional Autónoma de México
Circuito de la Investigación Científica s/n
Ciudad Universitaria
Delegación Coyoacán, 04510
México D.F., México

I. Herrera and I. Contreras

Abstract

At present, the most efficient domain decomposition methods (DDM) are non-overlapping methods. The improved efficiency of such methods is due to the significant independence achieved by local problems when the subdomains are non-overlapping. However, standard discretizations applied up to now in non-overlapping DDMs use systems of nodes in which some of the nodes are shared by more than one subdomain of the domain decomposition. This is a limiting feature of the present state-of-the-art in these techniques and apparently further increases of the independence of local problems should be expected if this limiting characteristic was eliminated. In previous work, I. Herrera and co-workers have developed a new approach to domain decomposition methods: the 'DVS framework' that addresses this problem introducing a new discretization method, the 'non-overlapping discretization method', in which a non-overlapping system of nodes is used in the discrete formulation of the problem.

Although the DVS algorithms have already been developed significantly, to profit from such advances it is essential to have available effective codes that permit their efficient implementation. As a further contribution in this line of research, in this paper we present and test software of such characteristics. The results here reported indicate that the DVS algorithms are very suitable for developing software that permits to apply effectively the most advanced hardware in parallel available at present to the solution of partial differential equations. Although the software here reported specifically treats static elasticity only, the DVS-algorithms are very eclectic and can be applied to a great diversity of problems after they have been discretized. Additional research work is being carried out oriented to develop general purpose codes based on the DVS algorithms.

Key words: Parallel software for PDEs, parallel processing of elasticity, high performance computing, HPC, elastostatics, parallel computing, domain decomposition methods (DDM).

Introduction

Mathematical models occurring in science and engineering, lead to systems of partial differential equations (PDEs) (Herrera and Pinder, 2012), whose solution methods are based on the computational processing of large-scale algebraic systems and the advance of many areas, particularly Earth Sciences, depends on the application of the most powerful computational hardware to them (Presiden'ts Information Technology Advisoty Committee, 2005).

Parallel computing is outstanding among the new computational tools, especially at present when further increases in hardware speed apparently have reached insurmountable barriers.

As it is well known, the main difficulties of parallel computing are associated with the coordination of the many processors that carry out the different tasks and the information-transmission. Ideally, given a task, these difficulties disappear when such '*a task is carried out with the processors working independently of each other*'. We refer to this latter condition as the '*paradigm of parallel-computing software*'.

The emergence of parallel computing prompted on the part of the computational-modeling community a continued and systematic effort with the purpose of harnessing it for the endeavor of solving the mathematical models of scientific and engineering systems. Very early after such an effort began, it was recognized that domain decomposition methods (DDM) were the most effective technique for applying parallel computing to the solution of partial differential equations (DDM Organization 1988-2014), since such an approach drastically simplifies the coordination of the many processors that carry out the different tasks and also reduces very much the requirements of information-transmission between them (Toselli and Widlund, 2005) (Farhat *et al*., 2000).

When a *DDM* is applied, firstly a discretization of the mathematical model is carried out in a *fine-mesh* and, afterwards, a *coarse-mesh* is introduced, which properly constitutes the domain-decomposition. The '*DDM-paradigm*', a paradigm for domain decomposition methods concomitant with the *paradigm of parallel-computing software* (Herrera *et al*., 2014*)*, consists in '*obtaining the global solution by solving local problems exclusively*' (a local problem is one defined separately in a subdomain of the *coarse-mesh*). Stated in a simplistic manner, the basic idea is that, when the *DDM-paradigm* is satisfied, full parallelization can be achieved by assigning each subdomain to a different processor.

When intensive DDM research began much attention was given to *overlapping DDMs*, but soon after attention shifted to *non-overlapping* DDMs. When the *DDM-paradigm* is taken into account, this evolution seems natural because it is easier to uncouple the local problems when the subdomains do not overlap. However, even in this kind of methods different subdomains are linked by interface nodes that are shared by several subdomains and, therefore, *non-overlapping DDMs* are actually overlapping when seen from the perspective of the nodes used in the discretization. So, a more thorough uncoupling of the local problems and significant computational advantages should be expected if it were possible to carry out the discretization of the differential equations in a '*non-overlapping system of nodes*' (Herrera *et al*., 2014); i.e., a set of nodes with the property that each one of them belongs to one and only one subdomain of the *coarse-mesh* (this is the mesh that constitutes a *domain decomposition*). In (Herrera *et al*., 2014), as in what follows, discretization methods that fulfill these conditions are referred to as *non-overlapping discretizations*.

In a line of research, which this paper belongs to, I. Herrera and co-workers addressed this problem and to cope with it have developed a framework -the '*DVS-framework*'- thoroughly formulated using a *non-overlapping discretization* of the original partial differential equations. Due to the properties of *non-overlapping discretizations* in such algorithms the links between different processors are very much relaxed, and also the required information-transmission between them is reduced. Such properties, as well as preliminary analysis of the algorithms, indicate that they should be extremely adequate to program the treatment of partial differential equations occurring in science and engineering models by the highly parallelized hardware of today. Although the *DVS-algorithms* have already been significantly developed and some examples have been previously treated (Herrera *et al*., 2014 and Carrillo-Ledesma *et al*., 2013), up to now no software that took full advantage of the *DVS-algorithms* had been developed. Clearly, to profit fully from such advances it is essential to develop software, carefully coded, which permit applying effectively the *DVS-algorithms* to problems of interest in science and engineering. As a further contribution to these advances, in this paper, for the first time we present and test software of such characteristics.

Overview of DVS-software

The *derived-vector-space framework (DVS-framework)* deals with the matrix that is obtained after the partial differential equation (PDE), or system of such equations, has been discretized by means of a standard discretization procedure (i.e., an *overlapping discretization*). The resulting discrete system of equations is referred to as the *original-system*.

The DVS-procedures follow the next steps:

1. The partial differential equation, or system of such equations, is discretized by any standard method that satisfies the axioms of the theory (here stated in section how to build non-overlapping discretizations) in a mesh -called the *fine-mesh*- to obtain a discrete problem that is written as

$$\underline{\underline{M}}\,\underline{U} = \underline{F} \qquad (2.1)$$

This is called the *original-problem*, while the nodes of the *fine-mesh* are called *original-nodes*. The notation $\hat{X}$ will be used for the whole set of *original-nodes*; any function defined on the set $\hat{X}$ by definition is an *original-vector*. Finally, the notation $\hat{W}$ will be used for the linear space spanned by the *original-vectors*, which in turn is called *original-vector space*;

2. A *coarse-mesh* is introduced, which constitutes a non-overlapping decomposition of the problem-domain. The system of *original-nodes* turns out to be *overlapping* with respect to the *coarse-mesh*;

3. A system of *non-overlapping nodes* (the *derived-nodes*), denoted by X, is constructed applying the procedure explained in previous articles (see also preliminary notions and notations). The functions defined in the whole set X are by definition the *derived-vectors* and the notation W is used for the whole linear space of *derived-vectors*, which constitutes the *derived-vector space*;

4. The theory of the *DVS-framework* supplies a formula that permits transforming the *original-discretization* into a *non-overlapping discretization*. Applying this formula the *non-overlapping discretization* is obtained. This is another discrete formulation that is equivalent to the *original-problem*, except that it constitutes a *non-overlapping discretization*; and

5. Thereafter, each one of the *coarse-mesh* subdomains is assigned to a different processor and the code is programmed separately in each one of the processors.

The theoretical DVS-framework is very elegant; in it, the algebraic operations can be carried out systematically and with great simplicity. Furthermore, many simplifying algebraic results have been obtained in previous work (Herrera *et al*., 2014 and Herrera and Yates, 2011). To optimize the communications and processing time a purely algebraic critical-route is defined, which profits much from such algebraic results previously obtained. Then, this algebraic critical-route is transformed into a computational code using *C++* and several well-established computational techniques such as MPI.

Following the steps indicated above, in the present paper software for problems of isotropic elastic solids in equilibrium has been developed and tested experimentally. The high parallelization efficiency of the software so obtained has been verified experimentally. To be specific, only the DVS-BDDC algorithm has been implemented for this problem. However, by simple combinations of the routines already developed the other *DVS-algorithms* can be implemented.

The standard discretization

Following the steps succinctly described in overview of DVS-software, software that constitutes a tool for effectively applying massively parallel hardware to isotropic elastic solids in equilibrium was constructed. In particular, it permits to treat the following boundary value problem (BVP):

$$(\lambda + \mu)\, \nabla\nabla\bullet\underline{u} + \mu_{\Delta}\underline{u} = \underline{f}_{\Omega} \quad (3.1)$$

Subjected to the *Dirichlet* boundary conditions:

$$\underline{u} = 0,\ \text{on}\ \partial \quad (3.2)$$

By simple modifications of the code, other boundary conditions can also be accommodated.

The software that we have developed treats in parallel the discrete system of linear equations that is obtained when the *standard discretization method* used to obtain the *original discretization* of the Dirichlet BVP defined by Eqs. (3.1) and (3.2) is the finite element method (FEM). In particular, it was obtained applying the well-known variational principle:

$$\int_{\Omega} \left\{ (\lambda + \mu)(\nabla\bullet\underline{u})(\nabla\bullet\underline{w}) + \mu\,\nabla\underline{u}:\nabla\underline{w} \right\} dx =$$
$$\int_{\Omega} \underline{f}_{\Omega}\bullet\underline{w}\,dx \quad (3.3)$$

with linear functions.

Such system of equations can be written as

$$\underline{\underline{M}}\,\underline{U} = \underline{F} \quad (3.4)$$

Here, it is understood that the vectors $\underline{U}$ and $\underline{F}$, are functions defined on the whole set of *original-nodes* of the mesh used in the FEM discretization, whose values at each node are 3-D vectors. They can be written as $\underline{U} \equiv (\underline{U}_p) \equiv (U_{pi})$ and $\underline{F} \equiv (\underline{F}_p) \equiv (F_{pi})$. As for the matrix $\underline{\underline{M}}$, the notation

$$\underline{\underline{M}} \equiv (\underline{\underline{M}}_{pq}) \equiv (M_{piqj}) \quad (3.5)$$

is adopted. Above, the range of *p and q* is the whole set of *original-nodes*, while *i* and *j* may take any of the values 1, 2, 3.

Preliminary notions and notations

The *DVS-approach* is based on *non-overlapping discretizations*, which were introduced during its development (Herrera *et al*., 2014). A discretization is *non-overlapping* when it is based on a system of nodes that is *non-overlapping*; to distinguish the nodes of such a system from the *original-nodes*, they are called *derived-nodes*. In turn, a system of nodes is *non-overlapping*, with respect to a *coarse-mesh* (or, domain-decomposition), if each one of them belongs to one and only one of the domain-decomposition subdomains. In the general DVS-framework, the *derived-vector space* (DVS) is constituted by the whole linear space of functions whose domain is the total set of *derived-nodes* and take values in $\mathbb{R}^n$. In the present paper, where problems of elasticity that are governed by a system of three PDEs are treated, we take $n = 3$. Usually, when the basic mathematical model is governed by a single differential equation, n is chosen to be equal to 1.

Generally, when the *coarse-mesh* is introduced some of the nodes of the *fine-mesh* fall in the closures of more than one subdomain of the *coarse-mesh*. When that is the case, a general procedure for transforming such an overlapping set of nodes into a non-overlapping one was introduced in previous papers (see Herrera *et al*., 2014). Such a procedure

consists in dividing each *original-node* into as many pieces as subdomains it belongs to, and then allocating one and only one of such pieces to each one of the subdomains. For a case in which the *coarse-mesh* consists of only four subdomains, this process is schematically illustrated in Figures 1 to 4.

Then, the final result is the system of *non-overlapping nodes* shown in Figure 4. Each one of the *non-overlapping* nodes is uniquely identified by the pair (p, α), where p is the *original-node* it comes from and α is the subdomain it belongs to. Using this notation, for each fixed $\beta = 1, ..., E$, it is useful to define $X^\beta \subset X$ as follows: The derived node (p, α) belongs to X^β, if and only if, $\alpha = \beta$.

In what follows, the family of subsets $\{X^1, ..., X^E\}$ just defined will be referred to as the *non-overlapping decomposition of the set of derived-nodes*. This because this family of subsets of X possesses the following property:

$$X = \bigcup_{\alpha=1}^{E} X^\alpha \ and \ \varnothing = X^\alpha \cap X^\beta \ when \ \alpha \neq \beta, \tag{4.1}$$

An important property implied by Eq. (4.1) is that the *derived-vector space*, W, is the direct-sum of the following family of subspaces of W: $\{W^1, ..., W^E\}$; i.e.,

$$W = W^1 \oplus ... \oplus W^E \tag{4.2}$$

Here, we have written

$$W^\alpha \equiv W(X^\alpha), \alpha = 1, ..., E \tag{4.3}$$

The notation $W(X^\alpha)$, introduced previously (see, for example Herrera *et al*., 2014), is here used to represent the linear subspace of W whose vectors vanish at every *derived-node* that does not belong to X^α. An important implication, very useful for developing codes in parallel, is that every *derived-vector* $\underline{w} \in W$ can be written uniquely in the form

$$\underline{w} = \sum_{\alpha=1}^{E} \underline{w}^\alpha, \ with \ \underline{w}^\alpha \in W^\alpha \tag{4.4}$$

As it is customary in DDM developments, in the *DVS-approach* a classification of the
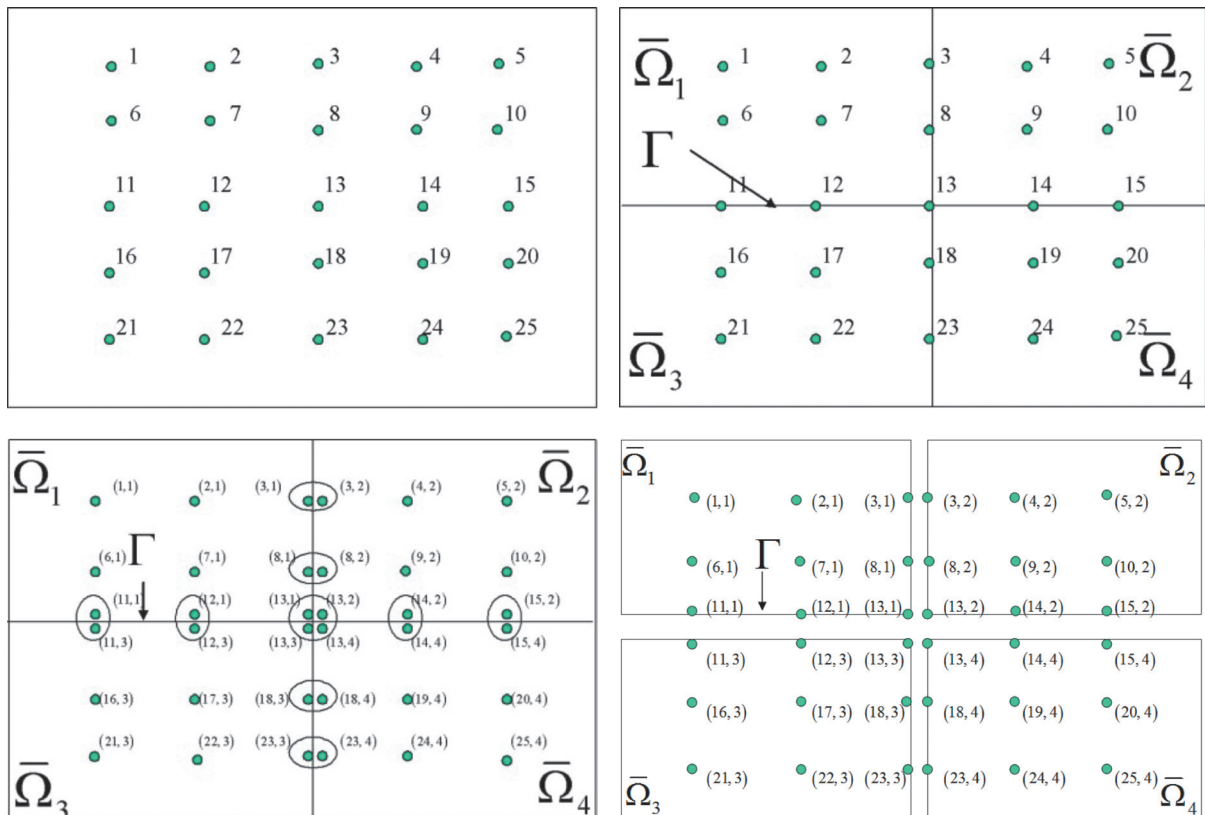
Figures 1 to 4.

nodes used is introduced. We list next the most relevant subsets of X used in what follows:

I *internal nodes*
Γ *interface nodes*
π *primal nodes*
Δ *dual nodes*
Π ≡ I∪π *'extended primal' nodes*
Σ ≡ I∪Δ *'extended dual' nodes*

Also, we observe that each one of the following set-families are disjoint: {I, Γ}, {I, π, Δ}, {Π, Δ} and {Σ, π}, while

$$X = I \cup \Gamma = I \cup \pi \cup \Delta = \Pi \cup \Delta = \Sigma \cup \pi$$
(4.6)

Next, we highlight some of most important notation and nomenclature used in the *DVS-framework*; for further details the reader is referred to previous works of this line of research (in particular (Herrera *et al.*, 2014), where additional references are given). When considering any given *derived-node*, which is identified by the pair of numbers (p, α), the natural number p (which corresponds to an *original-node*) is called the *'ancestor'* of the *derived-node*, while α (which ranges from 1 to E) identifies the subdomain it belongs to. Furthermore, for every *original-node* $p \in \widehat{X}$, the notation $Z(p) \subset X$ will be used to represent the set of *derived-nodes* that derived from it. Then, the *'multiplicity of p'*, $m(p)$, is the *cardinality* of $Z(p)$.

We observe that the *multiplicity of p* is defined as a property of each *original-node*, p. There is another kind of multiplicity that is used in the *DVS-framework*, which is defined as a property of each pair (p, q) of *original-nodes* and is also used in the *DVS-framework* theory. To introduce it, we define

$$\delta_{pq}^{\alpha} \equiv \begin{array}{l} 1, if\ p,q \in \overline{}_{\alpha} \\ 0, otherwise \end{array}, \alpha = 1,...,E;\ and$$
(4.7)

Then, the multiplicity of the pair (p, q) -written as $m(p, q)$- is defined to be

$$m(p,q) \equiv \sum_{\alpha=1}^{E} \delta_{pq}^{\alpha}$$
(4.8)

When $\underline{u}$ is a *derived-vector*, so that $\underline{u}$ is a function defined on X, $\underline{u}(p, \alpha)$ stands

for the value of $\underline{u}$ at the *derived-node* (p, α). In particular, in applications of the *DVS-framework* to elasticity problems, those values are -vectors and the real-number $u(p, \alpha, i)$ - $i = 1, 2, 3$- will be the $i–th$ component of the vector $\underline{u}(p, \alpha)$. The *derived-vector space* is supplied with an inner product, the *'Euclidean inner-product'*, which using the above notation for every pair of *derived-vectors*, $\underline{u}$ and $\underline{w}$, is defined by

$$\underline{u} \bullet \underline{w} \equiv \sum_{(p,\alpha)\in X} \sum_{i=1}^{3} u(p,\alpha,i) w(p,\alpha,i) = $$
$$\sum_{\alpha=1}^{E} \sum_{(p,\alpha)\in X^{\alpha}} \sum_{i=1}^{3} u(p,\alpha,i) w(p,\alpha,i)$$
(4.9)

For the parallelization of the algorithms the relation

$$\underline{u} \bullet \underline{w} = \sum_{\alpha=1}^{E} \underline{u}^{\alpha} \bullet \underline{w}^{\alpha}, whenever\ \underline{u}^{\alpha}, \underline{w}^{\alpha} \in W^{\alpha}$$
(4.10)

will be useful, because the vector-components corresponding to different subdomains will be handled by different processors when implementing them.

Let $p \in \widehat{X}$, be an *original-node* and $\underline{u} \in W$ a *derived-vector*. Then, $\underline{u} \in W$ is said to be *'continuous at p'* when $\underline{u}(p, \alpha)$ is independent of α, and it is said to be of *'zero-average at p'* when

$$\sum_{\alpha \in Z(p)} \underline{u}(p,\alpha) = 0 \qquad (4.11)$$

When the corresponding properties are satisfied for every $p \in \widehat{X}$, the derived-vector $\underline{u}$ is simply said to be *'continuous'* or *'zero-average'*. The linear subspaces W_{12} and W_{11} of W, are constituted by the *continuous* and the *zero-average* vectors of W, respectively. These two subspaces are orthogonal complements of each other. The matrices $\underline{\underline{a}}$ and $\underline{\underline{j}}$ are the orthogonal projections on $\widehat{W}_{12}$ and on W_{11}, respectively. They satisfy:

$$\underline{\underline{a}} + \underline{\underline{j}} = \underline{\underline{I}} \qquad (4.12)$$

where $\underline{\underline{I}}$ is the identity matrix. For any $\underline{w} \in W$, the explicit evaluation of $\underline{v} \equiv \underline{\underline{a}}\underline{w}$ is given by:

$$\underline{v}(p,\alpha) \equiv \frac{1}{m(p)} \sum_{(p,\beta) \in Z(p)} \underline{w}(p,\beta) \quad (4.13)$$

Using this equation, the evaluation of $\underline{j}\underline{w}$ is also straight forward, since Eq. (4.12) implies

$$\underline{j}\underline{w} = \underline{w} - \underline{a}\underline{w} \qquad (4.14)$$

The *natural injection* of $\widehat{W}$ into W, written as $R{:}\widehat{W} \to W$, is defined for every $\widehat{\underline{u}} \in \widehat{W}$ by

$$\left(R\widehat{\underline{u}}\right)(p,\alpha) = \widehat{\underline{u}}(p), \ \forall (p,\alpha) \in X \ (4.15)$$

When $\widehat{\underline{u}} \in \widehat{W}$, $\left(R\widehat{\underline{u}}\right) \in W_{12}$ necessarily. We observe that $R\widehat{W} = W_{12}$. Furthermore, it can be seen that R has a unique inverse in W_{12}; i.e., $R^{-1}{:}W_{12} \to \widehat{W}$ is well-defined.

How to build non-overlapping discretizations

This Section explains how to transform a standard (*overlapping*) discretization into a *non-overlapping discretization*. The DVS procedure here explained permits transforming an *overlapping discretization* into a *non-overlapping discretizations* and yields directly *preconditioned* algorithms that are subjected to *constraints*. It can be applied whenever the following basic assumption is fulfilled:

$$m(p,q) = 0 \Rightarrow M_{pq} = 0 \qquad (5.1)$$

Here, the symbol $\Rightarrow$ stands for the logical implication and it is understood that $\underline{M}$ is the matrix occurring in Eq. (2.1).

We define the matrix $\underline{a}'$ by its action on any vector of W: when $\underline{u} \in W$, we have

$$\underline{a}'\underline{u} = \underline{u}_I + \underline{u}_\Delta + \underline{a}\underline{u}_\pi \qquad (5.2)$$

We observe that the action of $\underline{a}$ can be carried out by applying the operator at the *primal-nodes* exclusively. Then, we define the '*constrained space*' by

$$W^r \equiv \underline{a}'W \qquad (5.3)$$

Clearly, $W^r {\subset} W$ is a linear subspace of W and for any $\underline{u} \in W$, $\underline{a}'\underline{u}$ is the projection of $\underline{u}$, on W^r.

Now, we define

$$s(p,q) \equiv \begin{matrix} 1, when \ m(p,q) = 0 \\ m(p,q), when \ m(p,q) \neq 0 \end{matrix} \ (5.4)$$

For $\gamma = 1, ..., E$, we define the matrices

$$\underline{M}^\gamma \equiv \left(M_{pq}^\gamma\right) with \ M_{pq}^\gamma \equiv \frac{M_{pq}}{s(p,q)} \delta_{pq}^\gamma \ (5.5)$$

Next, we define the matrices:

$$\underline{A}^\gamma \equiv \left(A_{(p,\alpha)(q,\beta)}^\gamma\right) with \ A_{(p,\alpha)(q,\beta)}^\gamma \equiv M_{pq}^\gamma \delta_{(\alpha,\gamma)} \delta_{(\beta,\gamma)}$$

$$(5.6)$$

and

$$\underline{A}^t \equiv \sum_{\gamma=1}^{E} \underline{A}^\gamma \qquad (5.7)$$

Then, we define

$$\underline{A} \equiv \underline{a}'\underline{A}^t\underline{a}' \qquad (5.8)$$

The following result was shown in previous papers (Herrera *et al*., 2014):

Theorem 5.1.- Let $\underline{U} \in \widehat{W}$ and $\underline{u} \in W$ be related by $\underline{u} = RU$, while $\underline{f} \in W_{12}$ is defined by

$$\underline{f} \equiv R\left(\widehat{\underline{m}}^{-1}\underline{F}\right) \qquad (5.9)$$

Here, $\widehat{m}$ is a diagonal matrix that transforms $\widehat{W}$ into itself, whose diagonal-values are $m(p)$, while here its inverse is denoted by $\widehat{\underline{m}}^{-1}$. Then, the discretized version of static elasticity of Eq.: (3.4):

$$\underline{M}\underline{U} = \underline{F} \qquad (5.10)$$

is fulfilled, if and only if

$$\underline{a}\underline{A}\underline{u} = \underline{f} \ and \ \underline{j}\underline{u} = 0 \qquad (5.11)$$

Proof.- See for example (Herrera *et al.*, 2014).

The preconditioned DVS-algorithms with constraints

There are four *DVS-algorithms* (Herrera *et al.*, 2014), and two of them are the DVS-BDDC and the DVS- FETI-DP. These are DVS versions of the well-known BDDC (Dohrmann, 2003), (Mandel *et al.*, 2005) and FETI-DP (Farhat and Roux, 1991), (Farhat *et al.*, 2000). As for the other two, nothing similar had been reported in the literature prior to the publication of the *DVS-algorithms*. By now, it is well known that BDDC and FETI-DP are closely related and the same can be said of the whole group of four DVS-algorithms.

The DVS-Schur-complement is defined by

$$\underline{\underline{S}} \equiv \underline{\underline{A}}_{\Delta\Delta} - \underline{\underline{A}}_{\Delta\Pi} \left(\underline{\underline{A}}_{\Pi\Pi} \right)^{-1} \underline{\underline{A}}_{\Pi\Delta} \qquad (6.1)$$

We also define

$$\overline{\underline{f}}_{\Delta} \equiv \underline{f}_{\Delta} - \underline{\underline{A}}_{\Delta\Pi} \left(\underline{\underline{A}}_{\Pi\Pi} \right)^{-1} \underline{f}_{\Pi} \qquad (6.2)$$

Then, writing $\underline{u} \equiv \underline{u}_{\Pi} + \underline{u}_{\Delta}$ it has been shown (Herrera *et al.*, 2014) that Eq. (5.11) is fulfilled if and only if

$$\underline{\underline{a}}\underline{\underline{S}}\underline{u}_{\Delta} = \overline{\underline{f}}_{\Delta}, \quad \underline{\underline{j}}\underline{u}_{\Delta} = 0 \qquad (6.3)$$

and

$$u_{\Pi} = \left(\underline{\underline{A}}_{\Pi\Pi} \right)^{-1} \left(\underline{f}_{\Pi\Delta} - \underline{\underline{A}}_{\Pi\Delta}\underline{u}_{\Delta} \right) \qquad (6.4)$$

The general strategy followed in the DVS approach, is to find $\underline{u}_{\Delta} \in W(\Delta)$ first and then apply Eq. (6.4) to obtain the remaining part, $\underline{u}_{\Pi} \in W(\Pi)$, of $\underline{u}$. For this strategy to be effective it is essential that the application of $\left(\underline{\underline{A}}_{\Pi\Pi} \right)^{-1}$ be computationally cheap. Different DVS-algorithms are derived by seeking different pieces of information such that $\underline{u}_{\Delta} \in W(\Delta)$ can be derived from it in a computationally-cheap manner. In particular, the four DVS-algorithms mentioned before seek for: $\underline{u}_{\Delta}$, $\underline{\underline{j}}\underline{\underline{S}}\underline{u}_{\Delta}$, $\underline{\underline{S}}^{-1}\underline{\underline{j}}\underline{\underline{S}}\underline{u}_{\Delta}$ and $\underline{\underline{S}}\underline{u}_{\Delta}$, respectively. Drawing from (Herrera *et al.*, 2014), they are here listed.

The DVS-BDDC algorithm

This algorithm seeks for $\underline{u}_{\Delta}$. It is:

$$\underline{\underline{a}}\underline{\underline{S}}^{-1}\underline{\underline{a}}\underline{\underline{S}}\underline{u}_{\Delta} = \underline{\underline{a}}\underline{\underline{S}}^{-1}\underline{f}_{\Delta} \, and \, \underline{\underline{j}}\underline{u}_{\Delta} = 0 \quad (6.5)$$

The DVS-primal-algorithm

We set $\underline{v}_{\Delta} \equiv \underline{\underline{S}}^{-1}\underline{\underline{j}}\underline{\underline{S}}\underline{u}_{\Delta}$ and the algorithm consists in searching for a function $\underline{v}_{\Delta} \in W_{\Delta}$, which fulfills:

$$\underline{\underline{S}}^{-1}\underline{\underline{j}}\underline{\underline{S}}\underline{\underline{j}}\underline{v}_{\Delta} = \underline{\underline{S}}^{-1}\underline{\underline{j}}\underline{\underline{S}}\underline{\underline{j}}\underline{\underline{S}}^{-1}\underline{f}_{\Delta} \, and \, \underline{\underline{a}}\underline{\underline{S}}\underline{v}_{\Delta} = 0$$
$$(6.6)$$

Once $\underline{v}_{\Delta} \in W(\Delta)$ has been obtained, then

$$\underline{u}_{\Delta} = \underline{\underline{a}}\left(\underline{\underline{S}}^{-1}\underline{f}_{\Delta} + \underline{v}_{\Delta} \right) \qquad (6.7)$$

The DVS-feti-dp algorithm

This algorithm seeks for $\underline{\lambda} \equiv \underline{\underline{j}}\underline{\underline{S}}\underline{u}_{\Delta}$. Thus, the algorithm is: "Given $\underline{f}_{\Delta} \in \underline{\underline{a}}W_{\Delta}$, find $\underline{\lambda}_{\Delta} \in W_{\Delta}$ such that

$$\underline{\underline{j}}\underline{\underline{S}}\underline{\underline{j}}\underline{\underline{S}}^{-1}\underline{\lambda} = -\underline{\underline{j}}\underline{\underline{S}}\underline{\underline{j}}\underline{\underline{S}}^{-1}\underline{f}_{\Delta} \, and \, \underline{\underline{a}}\underline{\lambda} = 0 \quad (6.8)$$

Once $\underline{\lambda} \in W_{\Delta}$ has been obtained, $\underline{u}_{\Delta} \in \underline{\underline{a}}W_{\Delta}$ is given by:

$$\underline{u}_{\Delta} = \underline{\underline{a}}\underline{\underline{S}}^{-1}\left(\underline{f}_{\Delta} + \underline{\lambda} \right) \qquad (6.9)$$

The DVS-dual-algorithm

In this case one seeks for $\underline{\mu} \equiv \underline{\underline{S}}\underline{u}_{\Delta}$ using the relation:

$$\underline{\underline{S}}\underline{\underline{a}}\underline{\underline{S}}^{-1}\underline{\underline{a}}\underline{\mu} = \underline{\underline{S}}\underline{\underline{a}}\underline{\underline{S}}^{-1}\underline{f}_{\Delta} \, and \, \underline{\underline{j}}\underline{\underline{S}}^{-1}\underline{\mu} = 0_{(6.10)}$$

Once $\underline{\mu}_{\Delta} \in W(\Delta)$ has been obtained, $\underline{u}_{\Delta} \in W(\Delta)$ is given by:

$$\underline{u}_{\Delta} = \underline{\underline{S}}^{-1}\underline{\mu} \qquad (6.11)$$

The elementary pieces of DVS-software

All the DVS-algorithms are iterative algorithms and can be implemented with recourse to Conjugate Gradient Method (CGM), when the matrix is definite and symmetric, as is the case of elasticity problems here considered, or some other iterative procedure such as GMRES, when that is not the case. At each iteration step, depending on the *DVS-algorithm* that is applied, one has to compute the action on an arbitrary *derived-vector* of one of the following matrices:

$\underline{\underline{a}}\underline{\underline{S}}^{\sim 1}\underline{\underline{a}}\underline{\underline{S}}$, $\underline{\underline{j}}\underline{\underline{S}}\underline{\underline{j}}\underline{\underline{S}}^{\sim 1}$, $\underline{\underline{S}}^{\sim 1}\underline{\underline{j}}\underline{\underline{S}}\underline{\underline{j}}$ or $\underline{\underline{S}}\underline{\underline{a}}\underline{\underline{S}}^{\sim 1}\underline{\underline{a}}$. In turn, such matrices are different permutations of $\underline{\underline{S}}$, $\underline{\underline{S}}^{\sim 1}$, $\underline{\underline{a}}$ and $\underline{\underline{j}}$. Thus, a code for implementing any of the DVS-algorithms can be easily developed when codes for carrying out the action of each one of such matrices are already available.

To produce such codes will be the goal of the next Section, while the remaining of this one is devoted to obtain some auxiliary results that will be used there and were previously presented in (Herrera *et al*., 2014). The first one of such results is:

$$\underline{\underline{S}} \equiv \underline{\underline{A}}^{t}_{\Delta\Delta} - \underline{\underline{A}}^{t}_{\Delta\Pi}\left(\underline{\underline{a}}'\underline{\underline{A}}^{t}_{\Pi\Pi}\underline{\underline{a}}'\right)^{-1}\underline{\underline{a}}'\underline{\underline{A}}^{t}_{\Pi\Delta} \tag{7.1}$$

The second one is: When $\underline{w}\in W$, the following identity holds

$$\underline{\underline{S}}^{\sim 1}\underline{w} = \left(\underline{\underline{A}}^{\sim 1}\underline{w}_{\Delta}\right)_{\Delta} \tag{7.2}$$

Here the notation $\left(\underline{\underline{A}}^{\sim 1}\underline{w}_{\Delta}\right)_{\Delta}$ stands for the component on $W(\Delta)$ of $\underline{\underline{A}}^{\sim 1}\underline{w}_{\Delta}$.

The third and fourth results required refer to the *pseudo-inverses* that occur in Eqs. (7.1) and (7.2). They are:

Let $\underline{w}\in W^{r}(\Pi)$ and $\underline{v} \equiv \left(\underline{\underline{A}}_{\Pi\Pi}\right)^{\sim 1}\underline{w}$, then

$$\underline{\underline{a}}'\left(\underline{\underline{A}}^{t}_{\pi\pi} - \underline{\underline{A}}^{t}_{\pi I}\left(\underline{\underline{A}}^{t}_{II}\right)^{-1}\underline{\underline{A}}^{t}_{I\pi}\right)^{-1}\underline{v}_{\pi} =$$

$$\underline{w}_{\pi} - \underline{\underline{A}}^{t}_{\pi I}\left(\underline{\underline{A}}^{t}_{II}\right)^{-1}\underline{w}_{I}, \ and \ \underline{\underline{j}}\underline{v}_{\pi} = 0 \tag{7.3}$$

together with

$$\underline{v}_{I} = \left(\underline{\underline{A}}^{t}_{II}\right)^{-1}\left(\underline{w}_{I} - \underline{\underline{A}}^{t}_{I\pi}\underline{v}_{\pi}\right) \tag{7.4}$$

Let $\underline{w}\in W^{r}$ and $\underline{v} \equiv \underline{\underline{A}}^{\sim 1}\underline{w}$, then

$$\underline{\underline{a}}'\left(\underline{\underline{A}}^{t}_{\pi\pi} - \underline{\underline{A}}^{t}_{\pi\Sigma}\left(\underline{\underline{A}}^{t}_{\Sigma\Sigma}\right)^{-1}\underline{\underline{A}}^{t}_{\Sigma\pi}\right)\underline{v}_{\pi} =$$

$$\underline{w}_{\pi} - \underline{\underline{A}}^{t}_{\pi\Sigma}\left(\underline{\underline{A}}^{t}_{\Sigma\Sigma}\right)^{-1}\underline{w}_{\Sigma}, \ and \ \underline{\underline{j}}\underline{v}_{\pi} = 0 \tag{7.5}$$

together with

$$\underline{v}_{\Sigma} = \left(\underline{\underline{A}}^{t}_{\Sigma\Sigma}\right)^{-1}\left(\underline{w}_{\Sigma} - \underline{\underline{A}}^{t}_{\Sigma\pi}\underline{v}_{\pi}\right) \tag{7.6}$$

These two results permit applying iterative algorithms, in which the CGM is used, when the actions of $\left(\underline{\underline{A}}_{\Pi\Pi}\right)^{\sim 1}$ and $\underline{\underline{A}}^{\sim 1}$, respectively, are computed.

Construction of the DVS-software

All the DVS-algorithms presented in the Section on the preconditioned DVS-algorithms with constraints are iterative, as is the case with most DDM algorithms, and to implement them it is only necessary to develop parallelized codes capable of computing the action of each one of the matrices $\underline{\underline{S}}$, $\underline{\underline{S}}^{\sim 1}$, $\underline{\underline{a}}$ or $\underline{\underline{j}}$ on an arbitrary *derived-vector*, as it was foreseen in (Herrera *et al*., 2014).

In the code here reported, all system-of-equations' solutions that were non-local were obtained with the help of the CGM algorithm. Due to this fact, actually the following subprograms were required: $\underline{\underline{S}}$, $\underline{\underline{S}}^{\sim 1}$ and $\left(\underline{\underline{a}}\,\underline{\underline{S}}\,\underline{\underline{a}}\,\underline{\underline{S}}\right)^{-1}$. Furthermore, the application of

$$\underline{\underline{S}} = \underline{\underline{A}}^{t}_{\Delta\Delta} - \underline{\underline{A}}^{t}_{\Delta\Pi}\left(\underline{\underline{a}}'\underline{\underline{A}}^{t}_{\Pi\Pi}\underline{\underline{a}}'\right)^{-1}\underline{\underline{a}}'\underline{\underline{A}}^{t}_{\Pi\Delta} \tag{8.1}$$

requires to compute the action of $\left(\underline{\underline{a}}'\underline{\underline{A}}^{t}_{\Pi\Pi}\underline{\underline{a}}'\right)^{-1}$ which is non-local. Thus, an efficient subprogram to carry-out this operation efficiently in parallel was required and was developed.

The communications required by *DVS-algorithms* are very easy to analyze. Indeed, when a different processor is allocated to each one of the coarse-mesh subdomains (i.e., to the subsets of *derived-nodes*, X^{α}, $\alpha = 1, ..., E$, of the *non-overlapping partition of* X) –as it was done in the work here reported– transmission of information between different processors occurs only when the *global Euclidean inner-product* is computed, or either the matrix $\underline{\underline{a}}$ or the matrix $\underline{\underline{a}}'$ is applied. Furthermore, in these operations the amount of information transmitted is very small.

In a first tentative version of the software, a *master-processor* was also used. However, using such a *master-processor* as a communications center is very time-costly and when the *master-processor* is not used

as a communications center the work done by it is so small that it can be eliminated easily. When this is done, the performance of the DVS-algorithm became extremely good as it is explained and discussed in the Section on Numerical Results.

Only the DVS-BDDC algorithm was implemented. Although the implementation of the other three DVS-algorithms is very similar, and their expected parallel efficiency as well, their implementation would have taken additional time and effort that we preferred to save for future work.

Construction of the local DVS-software

A fundamental property of $\underline{\underline{A}}^t$, as defined by Eq. (5.7) is that it is block-diagonal, in which each one of the blocks is $\underline{\underline{A}}^\alpha$, for each $\alpha = 1$, ..., E, is a linear-transformation of W^α into itself. This property simplifies very much the parallelization of the codes to implement the DVS-algorithms.

To this end, each one of the subsets X^α of the *non-overlapping decomposition of* X, is assigned to a different processor and the set of processors is numbered accordingly. The fact that every vector $\underline{w} \in W$ can be written in a unique manner as

$$\underline{w} = \sum_{\alpha=1}^{E} \underline{w}_\alpha, \ with \ \underline{w}_\alpha \in W^\alpha \qquad (9.1)$$

is used for this purpose. The processor γ handles only the $\underline{w}_\gamma$ component of every vector $\underline{w} \in W$. Then, all the operations of the processor γ transform $\underline{w}_\gamma$ into a vector that also belongs to W^γ; even the operators $\underline{\underline{a}}$ and $\underline{\underline{a}}'$ transform $\underline{w}_\gamma$ into a vector of W^γ, except that $\underline{\underline{a}}$ and $\underline{\underline{a}}'$ require information from of a few neighboring processors. However, it is important to make sure that such information be updated at the time it is gathered.

When evaluating the action on a vector of any of the matrices considered, processor γ will be responsible of constructing the γ component of such a vector; in particular, $\left(\underline{\underline{S}}\underline{w}\right)_\gamma$, $\left(\underline{\underline{S}}^{-1}\underline{w}\right)_\gamma$, $\left(\underline{\underline{a}}\underline{w}\right)_{\gamma'}$ or $\left(\underline{\underline{j}}\underline{w}\right)_{\gamma'}$ depending on the matrix that is being applied. In what follows it is assumed that, from the start, the nodes of the set X^γ have been classified into I: *internal,* π: *primal,* and Δ: *dual.* Other *node-classes* of X^γ that will be considered are: Π: *extended-primal,* and Σ: *extended-dual.* Without any further notice, the following relation will also be used:

$$W^\gamma \equiv W^\gamma(\mathrm{I}) \oplus W^\gamma(\pi) \oplus W^\gamma(\Delta) =$$
$$W^\gamma(\Pi) \oplus W^\gamma(\Delta) = W^\gamma(\Sigma) \oplus W^\gamma(\pi)$$
$$(9.2)$$

The application of $\underline{\underline{a}}$, $\underline{\underline{a}}'$ and $\underline{\underline{j}}$

To start with, we evaluate $\left(\underline{\underline{a}}\underline{w}\right)_\gamma$ when $\underline{w} \in W^\gamma$. As it will be seen, the application of $\underline{\underline{a}}$ to any vector of W^γ requires exchange of information between processor γ and other processors. Indeed, recalling Eq. (4.13) we have

$$\left(\underline{\underline{a}}\underline{w}\right)_\gamma = \underline{\underline{a}}\underline{w}(p,\gamma) = \frac{1}{m(p)} \sum_{(p,\beta) \in Z(p)} \underline{w}(p,\beta) \quad (9.3)$$

Thus, this operation requires information from the processors that possess *derived-nodes* belonging to $Z(p)$; therefore, its computation involves communications between different processors, which may slow the processing. In view of Eq. (9.3), it is clear that except for this exchange of information, the evaluation of $\left(\underline{\underline{a}}\underline{w}\right)_{\gamma'}$ is very simple. Once $\underline{\underline{a}}\underline{w}$, has been obtained, the relation $\underline{\underline{j}}\underline{w} = \underline{w} - \underline{\underline{a}}\underline{w}$, can be used to compute the action of $\underline{\underline{j}}$. As for the action of $\underline{\underline{a}}'$, we recall that $\underline{\underline{a}}'$ is obtained when the application of $\underline{\underline{a}}$ is restricted to *primal-nodes.*

Before going ahead, some final comments are in order. The application of $\underline{\underline{a}}$, and hence that of $\underline{\underline{a}}'$, also requires transmission of information between the processors. Thus, for enhancing the efficiency of the codes it is essential that the application procedures be designed with great care. As it will be seen, with a few exceptions, all the exchange of information required when the DVS-algorithms are implemented is when the transformations $\underline{\underline{a}}$ and $\underline{\underline{a}}'$ are applied.

The DVS-software for $\underline{\underline{S}}$ and $\underline{\underline{S}}^{-1}$

It should be observed that in view of the definition of the matrix $\underline{\underline{A}}^\gamma$ and the submatrices occurring in the following decomposition:

$$\underline{\underline{A}}^\gamma = \begin{pmatrix} \underline{\underline{A}}^\gamma_{II} & \underline{\underline{A}}^\gamma_{I\pi} & \underline{\underline{A}}^\gamma_{I\Delta} \\ \underline{\underline{A}}^\gamma_{\pi I} & \underline{\underline{A}}^\gamma_{\pi\pi} & \underline{\underline{A}}^\gamma_{\pi\Delta} \\ \underline{\underline{A}}^\gamma_{\Delta I} & \underline{\underline{A}}^\gamma_{\Delta\pi} & \underline{\underline{A}}^\gamma_{\pi\Delta} \end{pmatrix} \qquad (9.4)$$

for any they transform vectors of $W(X^\gamma)$ into vectors of $W(X^\gamma)$. Therefore, the *local* matrix $\underline{\underline{Q}}$ is defined to be

$$\underline{\underline{Q}} \equiv \underline{\underline{A}}^\gamma \qquad (9.5)$$

where $\underline{\underline{A}}^\gamma$ is the matrix defined in how to build non-overlapping discretizations, by Eq. (5.6). In this equation the index γ is omitted in the definition of $\underline{\underline{Q}}$, because γ is kept fixed. Due to the comments already made, it is clear that $\underline{\underline{Q}}$ is a well-defined linear transformation of $\overline{\overline{W}}^\gamma$ into itself. In particular, when $\underline{w}^\gamma \in W^\gamma$, the computation of $\left(\underline{\underline{Q}}\,\underline{w}^\gamma\right)_\gamma$ can be carried out in an autonomous manner, at processor γ, without exchange of information with other processors. This is a fundamental difference with $\underline{\underline{a}}$, $\underline{\underline{a}}'$ and $\underline{\underline{j}}$, and implies that at each processor either the matrix $\underline{\underline{Q}}$ is constructed, or internal software capable of evaluating its action on any vector of W^γ is made available.

In view of Eq. (9.4), the matrix $\underline{\underline{Q}}$ will be written in two forms

$$\underline{\underline{Q}} = \left(\begin{array}{cc} \left(\begin{array}{cc} \underline{\underline{Q}}_{II} & \underline{\underline{Q}}_{I\pi} \\ \underline{\underline{Q}}_{\pi I} & \underline{\underline{Q}}_{\pi\pi} \end{array}\right) & \left(\begin{array}{c} \underline{\underline{Q}}_{I\Delta} \\ \underline{\underline{Q}}_{\pi\Delta} \end{array}\right) \\ \left(\begin{array}{cc} \underline{\underline{Q}}_{\Delta I} & \underline{\underline{Q}}_{\Delta\pi} \end{array}\right) & \left(\begin{array}{c} \underline{\underline{Q}}_{\Delta\Delta} \end{array}\right) \end{array}\right) = \left(\begin{array}{cc} \left(\begin{array}{cc} \underline{\underline{Q}}_{II} & \underline{\underline{Q}}_{I\Delta} \\ \underline{\underline{Q}}_{\Delta I} & \underline{\underline{Q}}_{\Delta\Delta} \end{array}\right) & \left(\begin{array}{c} \underline{\underline{Q}}_{I\pi} \\ \underline{\underline{Q}}_{\Delta\pi} \end{array}\right) \\ \left(\begin{array}{cc} \underline{\underline{Q}}_{\pi I} & \underline{\underline{Q}}_{\pi\Delta} \end{array}\right) & \left(\begin{array}{c} \underline{\underline{Q}}_{\pi\pi} \end{array}\right) \end{array}\right) \qquad (9.6)$$

The following expressions, which are clear in view of Eq. (9.6), will be used in the sequel:

$$\underline{\underline{Q}} = \left(\begin{array}{c} \underline{\underline{Q}}_{\Pi\Pi}\,\underline{\underline{Q}}_{\Pi\Delta} \\ \underline{\underline{Q}}_{\Delta\Pi}\,\underline{\underline{Q}}_{\Pi\Delta} \end{array}\right) = \left(\begin{array}{c} \underline{\underline{Q}}_{\Sigma\Sigma}\,\underline{\underline{Q}}_{\Sigma\pi} \\ \underline{\underline{Q}}_{\pi\Sigma}\,\underline{\underline{Q}}_{\pi\pi} \end{array}\right) \qquad (9.7)$$

Here:

$$\underline{\underline{Q}}_{\Pi\Pi} \equiv \left(\begin{array}{cc} \underline{\underline{Q}}_{II} & \underline{\underline{Q}}_{I\pi} \\ \underline{\underline{Q}}_{\pi I} & \underline{\underline{Q}}_{\pi\pi} \end{array}\right), \underline{\underline{Q}}_{\Pi\Delta} \equiv \left(\begin{array}{c} \underline{\underline{Q}}_{I\Delta} \\ \underline{\underline{Q}}_{\pi\Delta} \end{array}\right) \qquad (9.8)$$

$$\underline{\underline{Q}}_{\Delta\Pi} \equiv \left(\underline{\underline{Q}}_{\Delta I}\,\underline{\underline{Q}}_{\Delta\pi}\right), \underline{\underline{Q}}_{\Delta\Delta} \equiv \left(\underline{\underline{Q}}_{\Delta\Delta}\right)$$

and

$$\underline{\underline{Q}}_{\Sigma\Sigma} \equiv \left(\begin{array}{cc} \underline{\underline{Q}}_{II} & \underline{\underline{Q}}_{I\Delta} \\ \underline{\underline{Q}}_{\Delta I} & \underline{\underline{Q}}_{\Delta\Delta} \end{array}\right), \underline{\underline{Q}}_{\Sigma\pi} \equiv \left(\begin{array}{c} \underline{\underline{Q}}_{I\pi} \\ \underline{\underline{Q}}_{\Delta\pi} \end{array}\right)$$

$$\underline{\underline{Q}}_{\pi\Sigma} \equiv \left(\underline{\underline{Q}}_{\pi I}\,\underline{\underline{Q}}_{\pi\Delta}\right), \underline{\underline{Q}}_{\pi\pi} \equiv \left(\underline{\underline{Q}}_{\pi\pi}\right) \qquad (9.9)$$

A. The Local DVS-software for $\underline{\underline{S}}$

Let $\underline{w}_\Delta \in W$, and recall Eq. (7.1); then:

$$\left(\underline{\underline{S}}\underline{w}\right)_\gamma = \underline{\underline{Q}}_{\Delta\Delta}\,\underline{w}_\Delta - \underline{\underline{Q}}_{\Delta\Pi}\left(\underline{\underline{A}}_{\Pi\Pi}\right)^{-1}\underline{\underline{a}}'\underline{\underline{Q}}_{\Pi\Delta}\,\underline{w}_\Delta \qquad (9.10)$$

In this equation the meaning of the terms $\underline{\underline{Q}}_{\Delta\Delta}\,\underline{w}_\Delta$ and $\underline{\underline{Q}}_{\Pi\Delta}\,\underline{w}_\Delta$ are clear since both $\underline{\underline{Q}}_{\Delta\Delta}$ and $\underline{\underline{Q}}_{\Pi\Delta}$ are well-defined linear transformations of W^γ into itself. Something similar happens when the operator $\left(\underline{\underline{A}}_{\Pi\Pi}\right)^{-1}$ is applied to $\underline{\underline{a}}'\underline{\underline{Q}}_{\Pi\Delta}\,\underline{w}_\Delta$, since this is also a global linear transformation. It must also be understood that, when it is applied, the local vector $\left(\underline{\underline{a}}'\underline{\underline{Q}}_{\Pi\Delta}\,\underline{w}_\Delta\right)_\gamma$ has already been stored at processor γ and at each one of the other processors. Due to the global character of the operator $\left(\underline{\underline{A}}_{\Pi\Pi}\right)^{-1}$ special software was developed for it.

A.1. The local DVS-software for $\left(\underline{\underline{A}}_{\Pi\Pi}\right)^{-1}$

The local software that was developed is based on the next formula:

"Let $\underline{w}_\Pi \in W^r(\Pi)$ and $\underline{v}_\Pi = \left(\underline{\underline{A}}_{\Pi\Pi}\right)^{-1}\underline{w}_\Pi$, then

$$\underline{\underline{a}}'\left(\underline{\underline{A}}_{\pi\pi}^t - \underline{\underline{A}}_{\pi I}^t\left(\underline{\underline{A}}_{II}^t\right)^{-1}\underline{\underline{A}}_{I\pi}^t\right)\underline{v}_\pi =$$

$$\underline{w}_\pi - \underline{\underline{A}}_{\pi I}^t\left(\underline{\underline{A}}_{II}^t\right)^{-1}\underline{w}_I, \text{ and } \underline{\underline{j}}\underline{v}_\pi = 0 \qquad (9.11)$$

together with

$$v_I = \left(\underset{=}{A_{II}^t}\right)^{-1}\left(w_I - \underset{=}{A_{I\pi}^t} v_\pi\right) \quad (9.12)$$

To apply this formula iteratively, at each processor γ it was necessary to develop local software capable of carrying out the following operations:

$$\underset{=}{a}' \left[\underset{\underline{=}}{Q}_{\pi\pi} - \underset{\underline{=}}{Q}_{\pi I} \left(\underset{\underline{=}}{Q}_{II}\right)^{-1} \underset{\underline{=}}{Q}_{I\pi}\right] v_\pi = w_\pi - \underset{=}{a}'\underset{\underline{=}}{Q}_{\pi I} \left(\underset{\underline{=}}{Q}_{II}\right)^{-1} w_I \quad (9.13)$$

and, once convergence has been achieved, the following *autonomous* operation is carried out:

$$v_I = \left(\underset{\underline{=}}{Q}_{II}\right)^{-1}\left(w_I - \underset{\underline{=}}{Q}_{I\pi} v_\pi\right) \quad (9.14)$$

We see here that except for $\underset{=}{a}'$ all the linear transformations involved are *autonomous* and can be expressed by means of local matrices defined in each processor. In the DVS-software that is the subject of this paper, such matrices were not constructed but we recognize that in some problems such an option may be more competitive,

B. The Local DVS-Software for $\underset{=}{S}^{-1}$

The local software that was developed is based on the next formula: *"When $w_\Delta \in W(\Delta)$, then*

$$\underset{=}{S}^{-1} w = \left(\underset{=}{A}^{-1} w_\Delta\right)_\Delta \quad (9.15)$$

Therefore, if $v \in W^r$ is defined by the condition $\underset{=}{A}v = w_\Delta$ and it is written in the form $v = v_I + v_\Delta + v_{\pi'}$, then $\underset{=}{S}^{-1} w = v_\Delta$. A more explicit form of the condition $v \in W^r$ is $jv_\pi = 0$. This latter condition together with the equation $\underset{=}{A}v = w_\Delta$ gives rise to a global problem whose solution, in the parallel software we have developed, was based on the iterative scheme: *"Let $w_\Delta \in W(\Delta)$ and $v_\Delta \equiv \underset{=}{S}^{-1} w_\Delta = \left(\underset{=}{A}^{-1} w_\Delta\right)_\Delta$, then at processor γ:*

$$\underset{=}{a}' \left[\underset{\underline{=}}{Q}_{\pi\pi} - \underset{\underline{=}}{Q}_{\pi\Sigma} \left(\underset{\underline{=}}{Q}_{\Sigma\Sigma}\right)^{-1} \underset{\underline{=}}{Q}_{\Sigma\pi}\right] V_\pi =$$

$$-\underset{=}{a}'\underset{\underline{=}}{Q}_{\pi\Sigma} \left(\underset{\underline{=}}{Q}_{\Sigma\Sigma}\right)^{-1} w \;, and \; j\underset{=}{V}_\pi = 0 \quad (9.16)$$

Once v_π has been obtained, v_Δ is given by

$$\underset{=}{S}^{-1} w_\Delta = v_\Delta = \left(\left(\underset{\underline{=}}{Q}_{\Sigma\Sigma}\right)^{-1}\left(w_{\Sigma\Sigma} - \underset{\underline{=}}{Q}_{\Sigma\pi} v_\pi\right)\right)_\Delta \quad (9.17)$$

At processor γ that is being considered, Eqs. (9.16) and (9.17) are:

$$\underset{=}{a}' \left[\underset{\underline{=}}{Q}_{\pi\pi} - \underset{\underline{=}}{Q}_{\pi\Sigma} \left(\underset{\underline{=}}{Q}_{\Sigma\Sigma}\right)^{-1} \underset{\underline{=}}{Q}_{\Sigma\pi}\right] V_\pi =$$

$$-\underset{=}{a}'\underset{\underline{=}}{Q}_{\pi\Sigma} \left(\underset{\underline{=}}{Q}_{\Sigma\Sigma}\right)^{-1} w \;, and \; j\underset{=}{V}_\pi = 0 \quad (9.18)$$

and

$$v_\Delta = \left(\left(\underset{\underline{=}}{Q}_{\Sigma\Sigma}\right)^{-1}\left(w_\Sigma - \underset{\underline{=}}{Q}_{\Sigma\pi} v_\pi\right)\right)_\Delta (9.19)$$

respectively.

C. Applications of the Conjugate Gradient Method (CGM)

There are three main instances in which CGM was applied: *i*) to invert $\underset{=}{A}_{\Pi\Pi'}$; *ii*) to invert $\underset{=}{A}$; *iii*) to solve iteratively the *global equation* such equation may be: either Eq. (6.5), Eq. (6.6), Eq. (6.8) or Eq. (6.10), depending on the *DVS-algorithm* that is applied-. Furthermore, it should be mentioned that the inverses of the *local-matrices*: $\underset{\underline{=}}{Q}_{II}$ and $\underset{\underline{=}}{Q}_{\Sigma\Sigma}$ can either be obtained by direct or by iterative methods; in the *DVS-software* here reported, this latter option was chosen and CGM was also applied at that level.

Numerical Results

In the numerical experiments that were carried out to test the *DVS-software*, the boundary-value problem for static elasticity introduced in the standar discretization was treated. In this paper only the DVS-BDDC algorithm has been tested. Work is underway to test the other *DVS-algorithms*, albeit similar results are expected for them. The elastic material was assumed to be homogeneous; so, the Lamé parameters were assumed to be constant and their values were taken to be

Table 1. Numerical Results

Number of Subdomains = Number of processors	DoF.	Nodes by Subdomain	Primal Nodes	Processing Time in seconds	Parallel efficiency $\left(\dfrac{p_{min}}{p_{max}} \bullet s\right) \times 100$	Speed up $s = \dfrac{T(p_{min})}{T(p_{max})}$	Norm of error $\left\|\underline{e}\right\|_\circ$
8	22,244,625	941,192	583	14,959	1	1	0.0263
27	21,904,152	274,625	2,312	5,882	75%	2.543	0.018
64	22,244,625	117,649	5,211	2,676	70%	5.59	0.029
125	21,904,152	59,319	9,184	1,212	79%	12.342	0.011
216	22,936,119	35,937	14,525	703	79%	21.280	0.010
343	22,244,625	21,952	20,628	406	86%	36.845	0.010
512	23,641,797	13,824	27,391	242	97%	61.814	0.011
729	23,287,176	10,648	36,800	183	90%	81.74	0.010
1000	23,641,797	8,000	46,899	136	88%	109.992	0.009
1331	22,936,119	5,832	57,100	96	94%	155.823	0.010
1728	20,903,613	4,096	66,671	89	78%	168.078	0.009
2197	21,904,152	3,375	80,352	64	85%	233.734	0.008
2744	22,244,625	2,744	94,471	51	86%	293.313	0.009

$$\lambda = \frac{Ev}{(1+v)(1-2v)} = 29.6412 \times 10^9 \, \frac{N}{m^2}$$

$$\mu = \frac{E}{2(1+v)} = 27.3611 \times 10^9 \, \frac{N}{m^2}$$

These values correspond to a class of cast iron (for further details about such a material see, http://en.wikipedia.org/wiki/Poisson's_ratio) whose *Young modulus*, E, and *Poison ratio*, v, are:

$$E = 68.95 \times 10^9 \, \frac{N}{m^2} \; and \; v = 0.26$$

The domain $\Omega \subset R^3$ that the homogeneous-isotropic linearly-elastic solid considered occupies is a unitary cube. The boundary-value problem considered is a *Dirichlet problem*, with homogeneous boundary conditions, whose exact solution is:

$$\underline{u} = (\sin \pi x \sin \pi y \sin \pi z, \; \sin \pi x \sin \pi y \sin \pi z, \; \sin \pi x \sin \pi y \sin \pi z) \tag{10.1}$$

The *fine-mesh* that was introduced consisted of $(193)^3 = 7,189,057$ cubes, which yielded $(194)^3 = 7,301,384$ *original-nodes*.

The *coarse-mesh* consisted of a family of subdomains $\{\Omega_1, \ldots, \Omega_E\}$, whose interfaces constitute the *internal-boundary* Γ. The number E of subdomains was varied taking successively the values 8, 27, 64, 125, 216, 343, 512 and so on up to 2,744. The total

number of *derived-nodes* and corresponding number of *degrees-of-freedom* are around 7.5×10^6 and 2.5×10^6, respectively. The constraints that were imposed consisted of continuity at *primal-nodes*; in every one of the numerical experiments all the nodes located at edges and vertices of the *coarse mesh* were taken as *primal-nodes*. In this manner, the total number of *primal-nodes* varied from a minimum of 583 to a maximum of 94,471. Thereby, it should be mentioned that these conditions granted that at each one of the numerical experiments the matrix $\underline{\underline{A}}$ was positive definite and possessed a well-defined inverse.

All the codes were developed in C++ and MPI was used. The computations were performed at the Mitzli Supercomputer of the National Autonomous University of Mexico (UNAM), operated by the DGTIC. All calculations were carried out in a 314-node cluster with 8 processors per node. The cluster consists 2.6 GHz Intel Xeon Sandy Bridge E5-2670 processors with 48 GB of RAM.

As it was exhibited in the analysis of the operations, the transmission of information between different processors exclusively occurs when the *average-operators* $\underline{\underline{a}}$ and $\underline{\underline{a}}'$ are applied. In a first version of the software reported in the present paper such exchange of information was carried out through a *master-processor*, which is time expensive. However, the efficiency of the software (as a parallelization tool) improved very much when

the participation of the *master-processor* in the communication and exchange of information process was avoided. In its new version, the *master-processor* was eliminated altogether. A Table summarizing the numerical results follows.

It should be noticed that the *computational efficiency* is very high, reaching a maximum value of 96.6%. Furthermore, the efficiency increases as the number of processors increases, a commendable feature for software that intends to be top as a tool for programming the largest supercomputers available at present.

Conclusions

1. This paper contributes to further develop *non-overlapping discretization methods* and the *derived-vector approach (DVS)*, introduced by I. Herrera and co-workers (Herrera *et al*., 2014), (Herrera and Rosas-Medina, 2013), (Carrillo-Ledesma *et al*., 2013), (Herrera and Yates, 2011), (Herrera, 2007), (Herrera, 2008), (Herrera and Yates, 2010) and (Herrera and Yates, 2011);

2. A procedure for transforming *overlapping discretizations* into *non-overlapping* ones has been presented;

3. Such a method is applicable to symmetric and non-symmetric matrices;

4. To illustrate the procedures that are needed for constructing software based on non-*overlapping discretizations*, software suitable to treat problems of isotropic static elasticity has been developed; and

5. The software so obtained has been numerically tested and the high efficiency, as a parallelization tool, expected from DVS software has been experimentally confirmed.

The main general conclusion is that the *DVS* approach and *non-overlapping discretizations* are very adequate tools for applying highly parallelized hardware to treat the partial differential equations occurring in systems of science and engineering.

Acknowlegement

References

Carrillo-Ledesma A., Herrera I., de la Cruz Luis Miguel, 2013, Parallel Algorithms for Computational Models of Geophysical Systems". *Geofísica Internacional*, 52, 3, pp., 293-309.

DDM Organization, Proceedings of 22 International Conferences on Domain Decomposition Methods www.ddm.org, 1988-2014.

Dohrmann C.R., 2003, A preconditioner for substructuring based on constrained energy minimization. *SIAM J. Sci. Comput*., 25, 1, 246-258.

Farhat Ch., Roux F., 1991, A method of finite element tearing and interconnecting and its parallel solution algorithm. *Internat. J. Numer. Methods Engrg*., 32:1205-1227.

Farhat C., Lessoinne M., Pierson K., 2000, A scalable dual-primal domain decomposition method, *Numer. Linear Algebra Appl.*, 7, pp 687-714.

Farhat C., Lessoinne M., LeTallec P., Pierson K., Rixen D., 2001, FETI-DP a dual-primal unified FETI method, Part I: A faster alternative to the two-level FETI method. *Int. J. Numer. Methods Engrg*., 50, pp 1523-1544.

Herrera I., New Formulation of Iterative Substructuring Methods without Lagrange Multipliers: Neumann-Neumann and FETI, NUMER METH PART D E 24(3) pp 845-878, 2008 (Published on line Sep 17, 2007) DOI 10.1002/num 20293.

Herrera I., Theory of Differential Equations in Discontinuous Piecewise-Defined-Functions, NUMER METH PART D E, 23(3), pp 597-639, 2007. DOI 10.1002/num 20182.

Herrera I., de la Cruz L.M., Rosas-Medina A., Non Overlapping Discretization Methods for Partial, Differential Equations. NUMER METH PART D E, 30: 1427-1454, 2014, DOI 10.1002/num 21852. (Open source)

Herrera I., Pinder G.F., 2012, Mathematical Modelling in Science and Engineering: An axiomatic approach, John Wiley, 243p.

Herrera I., Rosas-Medina A., 2013, The Derived-Vector Space Framework and Four General Purposes Massively Parallel DDM

Algorithms", EABE (Engineering Analysis with Boundary Elements), 37, pp-646-657.

Herrera I., Yates R.A., The Multipliers-Free Dual Primal Domain Decomposition Methods for Nonsymmetric Matrices" NUMER. METH. PART D. E. 27(5) pp. 1262-1289, 2011. (Published on line April 28, 2010) DOI 10.1002/num.20581.

Herrera I., Yates R.A., The Multipliers-free Domain Decomposition Methods, NUMER. METH. PART D. E. 26: 874-905 July 2010 (DOI 10.1002/num. 20462)

Herrera I., Yates R.A., The Multipliers-Free Dual Primal Domain Decomposition Methods for Nonsymmetric Matrices, NUMER. METH. PART D. E. 27(5) pp. 1262-1289, 2011. DOI 10.1002/Num. 20581.

Mandel J., Tezaur R., 1996, Convergence of a substructuring method with Lagrange multipliers. *Numer. Math,* 73, 4, 473-487, .

Mandel J., Dohrmann C.R., 2003, Convergence of a balancing domain decomposition by constraints and energy minimization, Numer. *Linear Algebra Appl.*, 10, 7, 639-659.

Mandel J., Dohrmann C.R., Tezaur R., 2005, *An algebraic theory for primal and dual substructuring methods by constraints*, *Appl. Numer. Math.*, 54, 167-193.

President's Information Technology Advisoty Committee: PITAC, Computational Science: Ensuring America´s Competitiveness, Report to the President June 2005. 104 p. www.nitrd.gow/pitac

Toselli A., Widlund O., 2005, Domain decomposition methods- Algorithms and Theory, Springer Series in Computational Mathematics, Springer-Verlag, Berlin, 450p.

Tephra fall at Tungurahua Volcano (Ecuador) – 1999-2014: An Example of Tephra Accumulation from a Long-lasting Eruptive Cycle

Jorge Bustillos A.[*], Jorge E. Romero, Liliana Troncoso and Alicia Guevara C.

Resumen

El volcán Tungurahua despertó en 1999 después de 75 años de quietud, y su actividad continua hasta el presente (2015). Luego de quince años de erupciones, casi 0.13 km³ de tefra han sido emitidos y depositados principalmente hacia el oeste y suroeste del volcán. Con tal de describir la actividad volcánica y comprender las implicanciones asociadas a las emisiones de tefra, hemos revisado su: 1) distribución, 2) cuantificación, 3) componentes y 4) dinámica. La mayoría de las erupciones han consistido en explosiones discretas, erupciones Strombolianas, interacciones hidrovolcánicas desencadenando erupciones Vulcanianas, un evento Subpliniano y fases de transición de estilo, lo que es apoyado por el análisis de componentes de la tefra. Las mayores descargas de tefra han ocurrido en 2001, 2006 y 2014. La tasa de descarga de tefra ha incrementado en casi 2.1 veces entre el período previo a 2006 y el período posterior a 2006. El Tungurahua representa una fuente continua de peligro geológico sobre las regiones adyacentes, pero también es un laboratorio natural para el estudio de erupciones de larga duración y el efecto que estas tienen.

Palabras clave: Tefra, erupciones explosivas, estilo eruptivo, tasa de descarga, volumen emitido, Tungurahua.

Abstract

Tungurahua volcano awoke in 1999 after 75 years of quiescence, and its activity continues at the time of writing (2015). After fifteen years of eruptions, roughly 0.13 km³ of tephra have been released and deposited mainly to the west and southwest of the volcano. In order to describe the activity and understand the implications associated to its tephra emissions, we review the: 1) their distribution, 2) quantification of ejecta, 3) their components and 4) eruption dynamics. Most of the eruptions have consisted of short-lived explosions, Strombolian eruptions, hydro-volcanic interactions triggering Vulcanian eruptions, one Subplinian event and transitional style phases, which is supported by analysis of tephra components. Major tephra fallouts occurred in 2001, 2006, and 2014. The rate of tephra discharge increased almost 2.1 times from the pre-2006 period to the post-2006 period. Tungurahua poses a continuing geological hazard across the adjacent regions, but also it is a natural laboratory for studying long-lasting eruptions and their effect.

Key words: Tephra, explosive eruptions, eruption style, discharge rate, eruptive volume, Tungurahua.

J. Bustillos A.[*]
L. Troncoso
Facultad de Geología
Minas, Petróleos y Ambiental
Carrera de Ingeniería en Geología
Universidad Central del Ecuador
Casilla 872 A
Quito, Ecuador
[*]Corresponding autor: jebustillos@uce.edu.ec

J. E. Romero
Departamento de Geología
Universidad de Atacama
Av. Copayapu 485
Copiapó, Chile

A. Guevara C.
Departamento de Metalurgia Extractiva
Escuela Politécnica Nacional
Ladrón de Guevara E11·253
Quito, Ecuador

Introduction

Reaching 5023 meters above sea level (asl), Tungurahua (01°28' S, 78°27' W) is a young andesitic volcano, located 140 km southeast of Quito, in the Ecuadorian Andes (Figure 1A). After 75 years of quiescence, Tungurahua awoke in 1999 with a small explosion, beginning an eruptive period extending to the present. Short stages of low-to-moderate explosive activity accompanied by tephra fall, lava emissions, pyroclastic density currents (PDCs), and lahars have characterized the volcano's behavior (Hall *et al.*, 1999; Le Pennec *et al.*, 2008; Hall *et al.*, 2013).

The Volcanic Ash Advisory Center (VAAC) issued around 8000 reports of tephra emissions from Tungurahua volcano between 1999 and 2013, indicating its high level of activity. Staff of the Geophysical Institute at the National Polytechnic School (IG-EPN) and the Institut de Recherche pour le Développement (IRD)

carried out field mapping, sedimentological analysis, and volumetric estimations of tephra from the 1999-2001, 2006, 2010, 2012 and 2013 eruptions (eg. Le Pennec *et al.*, 2004; Ruiz *et al.*, 2004; Troncoso *et al.*, 2006; Bustillos, 2010; Bustillos *et al.*, 2011; Le Pennec *et al.*, 2011; Eychenne *et al.*, 2012; Bustillos *et al.*, 2013; Bernard *et al.*, 2013; Eychenne *et al.*, 2013). Moreover, in 2007 IG-EPN deployed "ashmeters" in a systematic network for monitoring tephra fall (Bustillos, 2010; Bustillos y Mothes, 2011; Bernard, 2013).

Fifteen years after its re-awakening, Tungurahua continues to be restless and its activity has forced people to learn how to live with persistent eruptions. In this paper we present a chronology of the last 15 years of eruptive activity (1999-2014), with special emphasis on the distribution, characteristics and volume of tephra emissions, and their impact and importance.
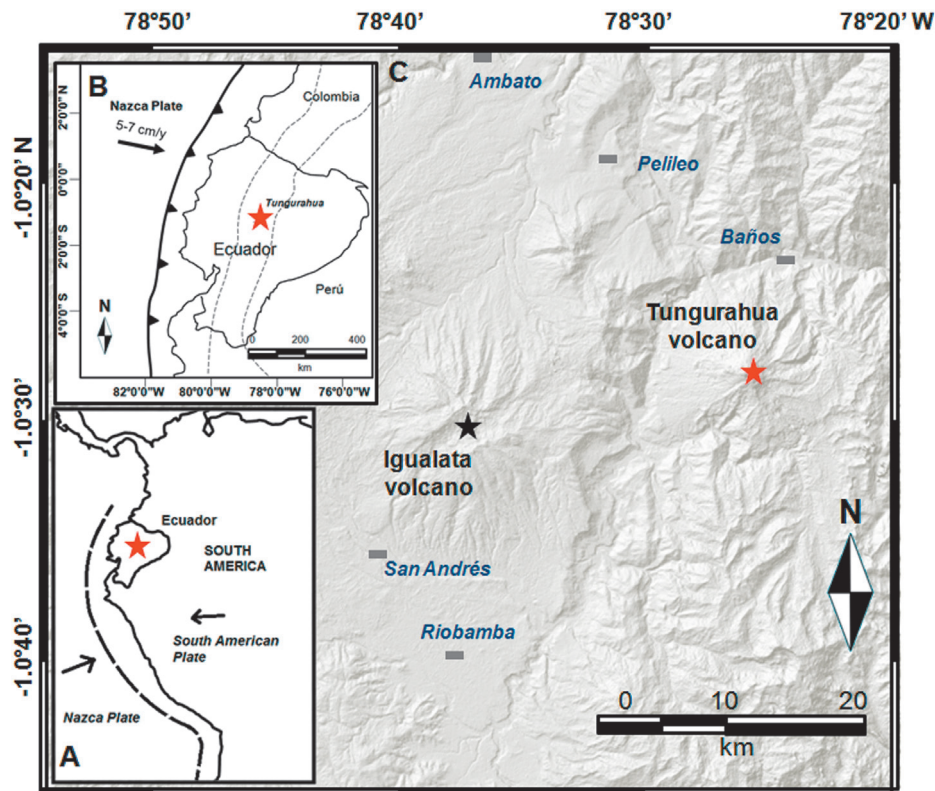

Figure 1. Location map of Tungurahua volcano. A: Location map of the study area in the context of South America. B: Tungurahua volcano in the geodynamic context. The Ecuadorian volcanic arc is represented by dotted lines. C: Main towns around the Tungurahua volcano.

Background of the volcano

The Tungurahua stratovolcano has a conical shape with flanks of 30° to 35° inclination, and a summit crater 500 m in diameter. The volcano was built on a basement of Paleozoic to Cretaceous metamorphic rocks in the Cordillera Real (Aspden *et al.*, 1994), locally intruded by granitic plutons of Paleozoic to Jurassic age (Litherland y Egüez, 1993). Two violent sector collapses 30,000 and 3000 years before present destroyed earlier volcanic structures and the present volcano is built upon their remnants (Hall *et al.*, 1999; Jaya, 2004; Molina *et al.*, 2005; Le Pennec *et al.*, 2006; Bustillos, 2008). Historical eruptions took place in 1641-1646, 1773-1781, 1886-1888, 1916-1918, leading up to the current 1999-present eruptive phase. Most of these eruptions were moderate to large in size, sufficient to achieve volcanic explosivity index (VEI) of 3 to 4 (Table 1). Eruption products during the history of the volcano range from andesite to dacite (SiO2 54-67% wt), but in historic times most have been andesitic (SiO2 ~58 % wt) (Hall *et al.*, 1999; Bustillos, 2008, Samaniego *et al.*, 2011).

Overview of the 1999-2014 eruptions

The Geophysical Institute has monitored the volcano since 1988 in cooperation with U.S. Geological Survey (USGS), IRD and other institutions (http://igepn.edu.ec/index.php/nosotros/patrocinadores). As a consequence of the robust IG-EPN monitoring network at Tungurahua, this Institute has provided detailed reports (http://igepn.edu.ec/index.php/tungurahua/informes-tungurahua), which document the various types of activity of the last fifteen years (Table 1). This activity can be divided into four eruptive stages (Figure 2A), as follows:

Phase I

This phase occurred between 1999 until 2005. Before the eruption onset, seismicity and fumaroles increased due to magmatic intrusion. A fluctuating eruption column of 6-12 km asl (above de sea level), reached a peak of intensity on December 6th (1999) with a height of 18 km asl (Le Pennec *et al.*, 2011). The activity included progressively

Table 1. Synthesis of the eruptive activity from 1999 to 2014 at Tungurahua volcano. Relevant volcanic phenomena are mentioned and the Volcanic Explosivity Index, VEI (Newall and Self, 1982) has been assessed using the volume of tephra emitted over each year and the highest eruption columns reported for these events.

Year	Lava flow	Tephra fall	Shockwave	Ballistic	PDC	Incandescence	Lahars	VEI
1999		X	X	X		X		1
2000		X					X	1
2001		X	X	X		X	X	2
2002		X	X	X		X	X	1
2003		X		X		X	X	1
2004		X	X	X		X	X	1
2005		X					X	1
2006	X	X	X	X	X	X	X	3
2007		X		X	X	X	X	1
2008		X			X		X	2
2009		X					X	1
2010	X	X	X	X	X	X	X	2
2011		X	X	X	X	X	X	1
2012		X	X	X	X	X	X	1
2013		X	X	X	X	X	X	2
2014	X	X	X	X	X	X	X	3

stronger steam emissions, tephra explosions (Figure 2B), releasing of incandescent blocks and shockwaves, followed by lava fountaining activity of Strombolian eruptions (Figure 2C) in 2002, 2003 and 2004, interpreted as the magma input, reservoir disruption, and ejection of low volumes of magma (Samaniego et al., 2011). Quiet periods were <3 months and were frequently intercalated with eruptions, which suggested repetitive intrusions of andesitic (58-59% wt SiO2) magma from depth at low rates (Samaniego et al., 2011). Eruptive activity during 2005 was almost totally absent.

Phase II

A detailed summary of this eruption period can be found in Steffke et al. (2010). Activity increased gradually from January to April 2006. From May to the first days of July strong explosions occurred, and were heard at a distance of 20 km and shock waves were felt and windows shook 10 to 15 km away from the volcano (Barba et al., 2006). Events of July 14th and August 16th produced severe PDCs (Figure 2D), followed by a lava effusion. Five people died as a consequence of these PDCs at Palictahua, 7 km south of Tungurahua´s summit. Details of the PDCs sedimentology are in Hall et al. (2013), Douilliet et al. (2013a, b) and Bernard et al. (2014). The 2006 eruptions were interpreted as a new, deep, hot, and volatile rich andesitic (58-59% wt SiO2) magma that entered a more evolved and degassed magma reservoir, and rapidly ascended to the surface (Samaniego et al., 2011; Eychenne et al., 2013; Myers et al., 2014). This eruption was classified as Subplinian.

Phase III

Subsequent to the explosive events of 2006, a third phase from 2007 to 2009 was characterized by reduced activity. Only small to moderate Strombolian events and a possible Vulcanian eruption occurred in 2007, February and August 2008, and the first half of 2009.

Phase IV

The latest phase has been occurring since 2010. PDCs from column collapse (sometimes immediately after the eruption) occurred in the first half of 2010, accompanied by eruption columns reaching 7 km above de crater level (acl) and the formation of a lava lake inside the crater signaled the ascent of magma. On May 28th, an explosion produced a column that rose 10 km (acl) into the atmosphere, and bombs 20 cm in diameter fell out to 5 km from the vent. On July 2010, the first reported purely-

Vulcanian event was seen (Bustillos, 2010) and by November 22th a new Vulcanian explosion ejected lapilli-sized fragments as far as 10 km from the vent (Bustillos, 2010). Myers et al (2014) suggested that the 2010 eruption was the result of a separate recharge and mixing magma events that occurred shortly before eruption. From February to April; August 18th-20th; and December 4th-16th, 2011 volcanic activity produced PDCs that coursed down all the flanks, but none of them affected populated areas. In 2013, Tungurahua erupted four times with mostly Strombolian activity lasting between 17 and 39 days (Vallejo et al., 2014). The largest eruption in 2013 took place on July 14th, with a 10 km high ash cloud and generation of PDCs. The year 2014 will be remembered for two major Vulcanian eruptions, one on February 1st, which was preceded by a short and striking volcanic tremor (VT) swarm plus several months of volcano deformation (Vallejo et al., 2014). The eruption column reached 14 km above the crater and PDCs sped down along eight valleys, reaching the zone of the main road at the base of the edifice in several locations (Douillet et al., 2014) (Figure 2E). The second eruption occurred on April 4th and consisted of a short explosion, following 48 h of notable increase in VT and low to moderate explosions, producing an eruption column that reached 10 km above the crater (J.E. Romero, pers. comm., August 20th, 2014). Lava flew down the west flank on April 10th and afterwards new Strombolian eruptions occurred in August 2014.

Tephra deposits

Overview of previous research

Most of the research on Tungurahua tephra deposits of 1999-2014 focused on their distribution (isopach, isomass maps) (Figure 3) and volume (eg. Le Pennec et al., 2004; Troncoso et al., 2006; Bustillos, 2010; Le Pennec et al., 2011; Eychenne et al., 2012; Bustillos et al., 2013; Bernard et al., 2013; Eychenne et al., 2013). A few studies described their sedimentological characteristics in the period 2006-2014 (eg. Eychenne and Le Pennec, 2012; Eychenne et al., 2012; Eychenne et al., 2013). Indirect methods for determining tephra discharge rates have been applied at Tungurahua using the models of thermal plumes (eg. Ruiz et al., 2004; Bustillos et al., 2011) and eruption mechanisms have also been studied (eg. Bustillos, 2010; Bustillos et al., 2013; Narvaez et al., 2014). Bustillos and Samaniego (2011) have processed the data of tephra volumes between 2001 and 2010 in order to obtain values of magnitude and

intensity for classifying these eruptions, using the scheme of Pyle (2000). These data are useful in tephra dispersal models, quantification of released materials and understanding of eruption dynamics.

Spatial distribution

At present, 11 isopach maps displaying the geographic distribution of the fallout deposits have been reconstructed (Figure 3). During the 15 years of activity, 70% of tephra fall affected areas west and west-southwest of the volcano (Figure 1c). Less than 10% of the tephra fell to the southwest or west-northwest, and less

than 5% fell in areas to the northeast or south southwest. An exceptional case of tephra distribution was observed during the February 1st, 2014 eruption, when fine ash fell more than 100 km to the north (Quito and Ibarra) and south (Cuenca and Loja). The most critical zone of tephra airfall deposition is an elliptical area west of the volcano and over the volcano's flanks, where total deposit thickness exceeded 10 cm. For the whole eruptive period and including the effects of wind erosion, sites like Palitahua and San Juan, 5 km from the crater, accumulated tephra thickness of 4 and 8 cm, respectively.
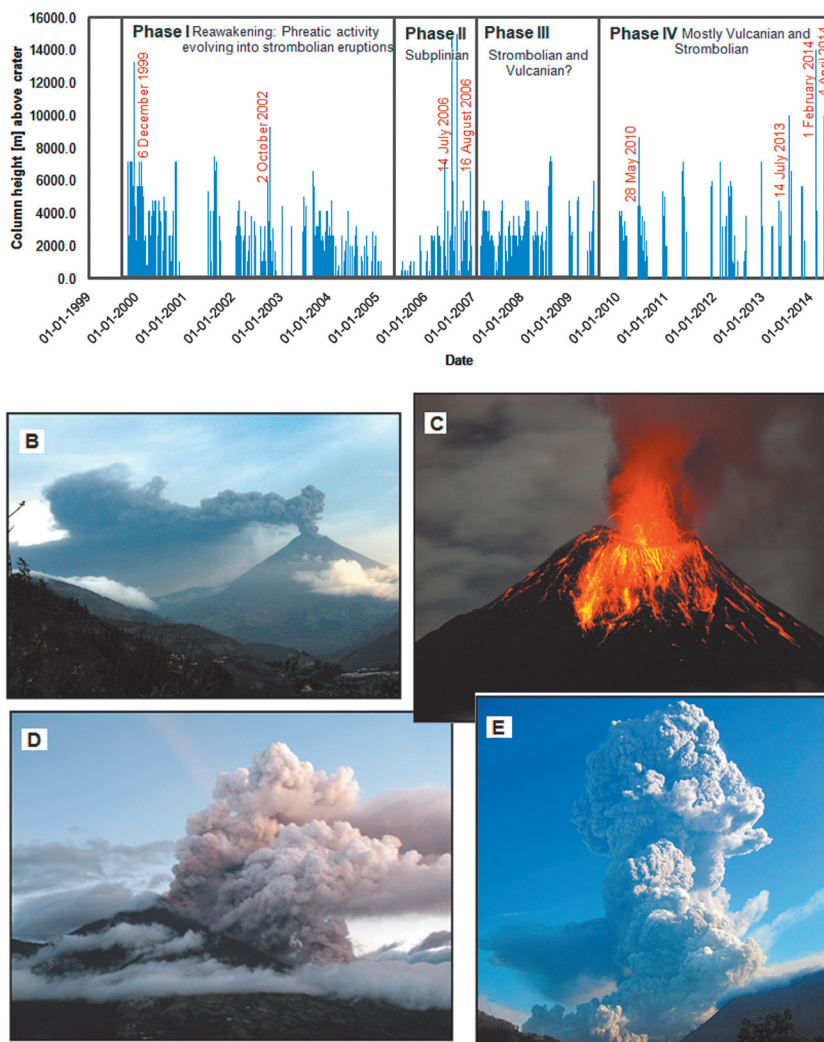

Figure 2. Chronology and phenomenology of the Tungurahua eruptions between 1999 and 2014. A: Eruption columns height vs. time. Column heights measured in use of geostationary satellite imagery and flight reports are provided by the VAAC (http://www.ssd.noaa.gov/VAAC/ARCH99/archive.html#TUNG). The four eruptive phases are distinguished and each most relevant eruption is mentioned. B: Low altitude (~1.0 km above the crater) tephra emissions forming an ash-loaded eruption plume. C: Typical Strombolian activity with discharge of metric-sized ballistic bombs. D: Explosive eruption on August 16th, 2006, with the formation of a PDC on the southwestern flank. E: Eruption column of February 1st, 2014. PDCs emplaced on all the flanks of the volcano.
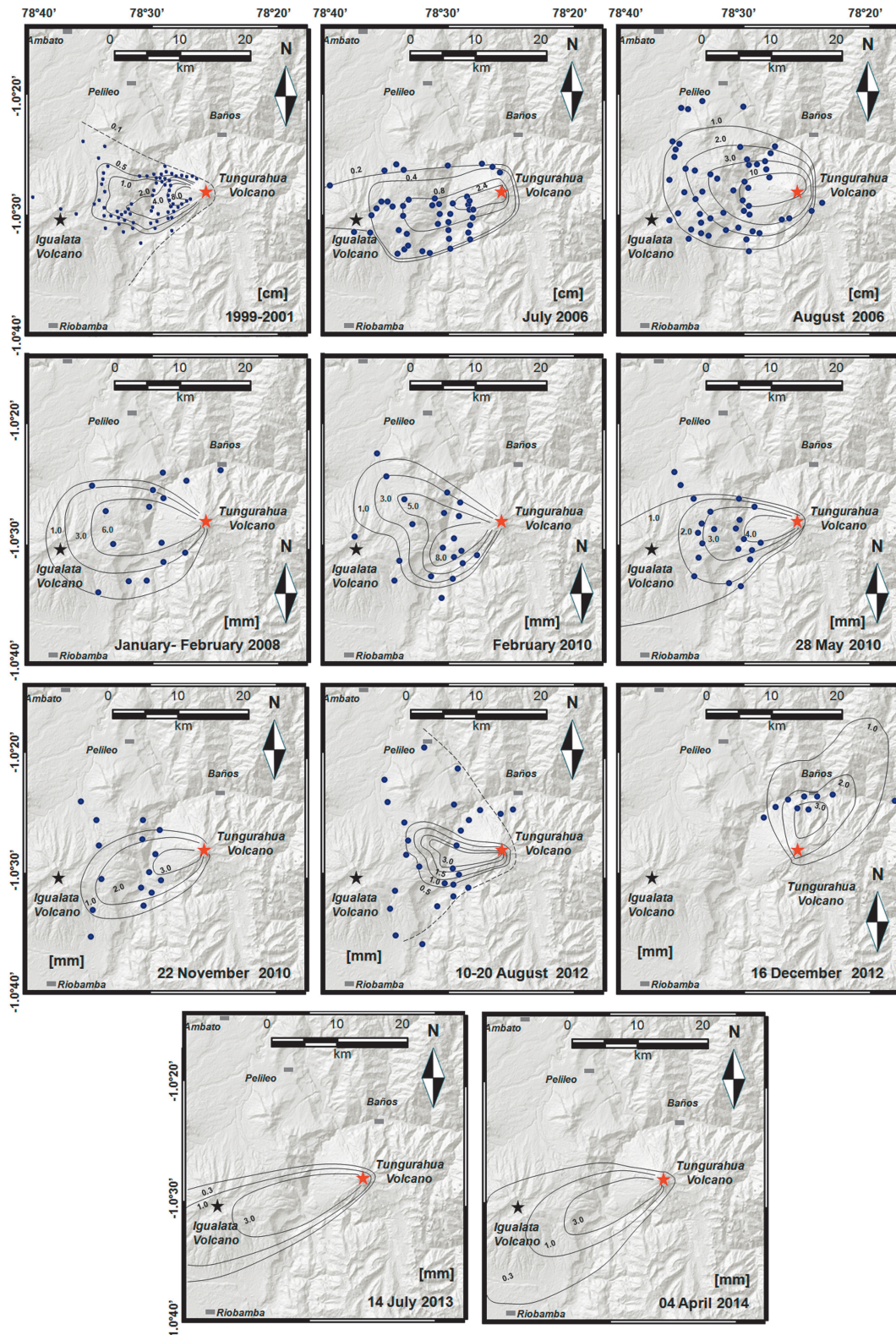
Figure 3. Isopach maps for the period 1999-2014 at Tungurahua volcano. Maps modified from Le Pennec *et al.* (2011), Troncoso *et al.* (2006), Bustillos (2010), Bernard *et al.* (2013) and unpublished material from the April 2014 eruption (J.E. Romero, pers. comm., August 20th, 2014). These maps have been drawn with the help of numerical modeling using Ash 3D code (see Schwaiger *et al.*, 2012). Blue circles represent the data points of thickness measurements.

Components and Grain size

During the period analyzed, components in tephra have consisted in juvenile scoriae (dark, light or reddish in color) (Figure 4A), with mainly Plagioclase (Pl) and Pyroxene (Px) crystals (Figure 4B); accessory lithics (mostly dark, dense and blocky) (Figure 4C); juvenile pumice, juvenile glass shards and tubes (Peleeʹs hairs and tears) (Figure 4D,E); aggregates (Pl and Px assemblages) (Figure 4F) and oxidized lithics (eg. Bustillos, 2010; Eychenne and Le Pennec, 2012; Eychenne *et al*., 2012; Eychenne *et al*., 2013; Bustillos *et al*., 2013; Narvaez *et al*., 2014). A subpopulation of grain sizes from -4 to 10 Phi (fine lapilli to very fine ash) within bimodal distributions, due to elutriation of material from PDCs, was reported (Eychenne *et al*., 2012).

The August 2006 eruption deposit consisted of six main classes of particles: 1) ragged, dark to brown andesitic scoriae; 2) light-toned, highly vesicular juvenile silicic (61.1-62.5 wt% SiO2) pumices; 3) euhedral Pl and Px irregularly coated free crystals; 4) dark-blocky, microcrystalline non-vesicular dense lithics; 6) assemblages of Pl and Px crystalline aggregates and 6) reddish subrounded, moderate vesicular scoriae (Eychenne *et al*. (2013).

The behavior of the 2010 eruption was studied thoroughly by Bustillos (2010). He interpreted the scarce lithic and crystal content, in addition with the dominantly Strombolian activity on January-February, as the transitional opening of the conduit. In contrast, the events of May 28th and November 22th produced highly vesicular fragments of hydrovolcanic origin, Pelee's tears, dense accessory andesitic lithics, scoriae and scarce free crystals consistent with Vulcanian eruptions. Most of the samples from the 2010 tephra fall deposits had grain sizes between 0 and 5 phi (from coarse to very fine ash), presenting unimodal distributions, and in a few cases bimodal distributions were observed in samples associated to fine ash input from co-ignimbrite fallout due to PDC elutriation (Bustillos, 2010).
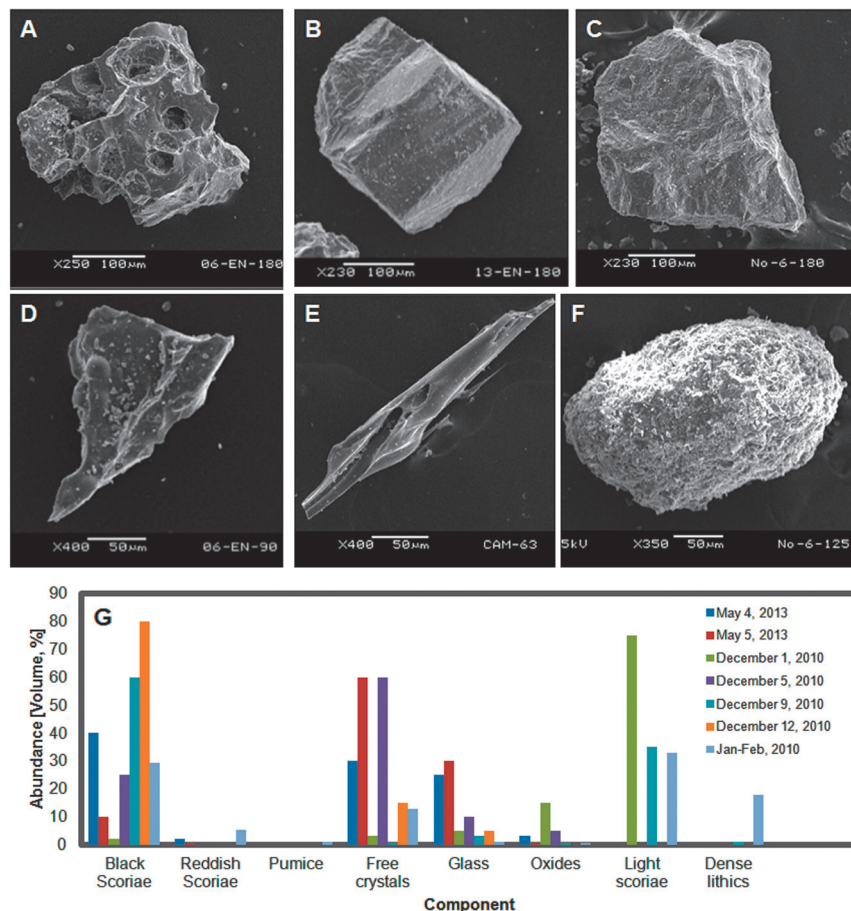

Figure 4. Components of the tephra fall deposits observed from 2006 to present. Views of Scanning Electron Microscopy (SEM) are presented for samples collected from deposits of the 2010 eruptions by Bustillos (2010). A: Scoria fragments. B: Free crystals. C: Lithics. D: Volcanic glass. E: Pele's tears-shaped volcanic glass. F: Aggregates. G: Variations of components for the 2010 and 2013 eruptions. Data from Bustillos (2010) and Bustillos *et al*. (2013).

The eruptions of May 4th and 5th, 2013 produced deposits consisting of: 1) blocky shaped black scoriae; 2) reddish sub-rounded to angular scoriae; 3) free anhedral crystals of Pl, Cpx and Opx; 4) volcanic glass with shard morphology; 5) Fe-Ti oxides; and 6) rare pumices with tabular an fibrous morphology (Bustillos *et al.*, 2013). Between May 4th to the 5th the abundance of black scoria decreased from 40 to 10 %; crystals increased from 30 to 60%, pumice particles became absent and appearance Pele's tears reflected a transition from a Vulcanian-dominated to an Strombolian style with lava fountaining. Samples of the March and July 2013 eruptions contained a large amount of oxidized rocks, free crystals, dense accessory lithics, and juvenile material (both pumice and scoria) revealing a Vulcanian mechanism. Pumice and scoria increased with time after the onset, suggesting an evolution from discrete explosions to an open-vent behavior (Narvaez *et al.*, 2014). Samples of March and July 2013 show mostly unimodal grain size distributions (Narvaez *et al.*, 2014; Figure 4G). Meanwhile, Douillet *et al.* (2014) have reported that variation in the components and particle rounding in the PDCs of 1st February 2014 eruption suggested in-situ abrasion depending on the flow path and type of blocks, which phenomena probably did not have affected the tephra fall grain size distribution of this last eruption. Also, early observation (February) of the mantling zones of singed vegetation indicated the impact of hot co-ignimbrite clouds. This aspect needs to be addressed in a near future. The latest eruptions of February and April are not yet described in terms of their deposits, and research on this matter is required.

Size and parameters of the eruptive activity

During Phase I (1999 to fall 2004) the volcano released nearby 25 x10^6 m³ of bulk tephra (Wright *et al.*, 2012). The events of July 14th and August 16th, 2006, (Phase II) were the largest recorded at Tungurahua in the entire eruptive cycle in progress, and released 42 and 26 x10^6 m³ of tephra fallout and PDCs, respectively (Troncoso *et al.*, 2006; Eychenne *et al.*, 2012; Hall *et al.*, 2013). Around 1.5 x10^6 m³ of tephra were produced in Phase III. After that, the largest volumes of tephra discharge during Phase IV occurred on July 14th, 2013 (calculated in 1.7 x10^6 m³); February 2014 with >8 x10^6 m³ (Vallejo *et al.*, 2014) and April 4th, 2014 that reached ~1.0 x10^6 m³ (J.E. Romero, pers. comm., August 20th, 2014). In summary, a total volume of 0.11 km³ in tephra fallout was released between 1999 and 2011 (Bustillos *et al.*, 2011), closing in 2014 near to 0.13 km³. This is ~25% of the minimum released tephra bulk volume, reported for the 2008 major Subplinian phase of Chaitén's eruption, of 0.5 km³ (Alfano *et al.*, 2012). The average rate of tephra discharge (Q) increased by more than two times from Phase I (Q ~ 8700 m³/day) to the period since 2006 (Phases II to IV) (Q ~ 19000 m³/day) (Figure 5A).

Following the approach of Walker (1980), the plot of tephra deposit area [km²] vs. thickness [cm] indicates that most of the tephra fall deposits are of Strombolian and Vulcanian types. In fact, a general summary of the thickness vs. area $^{1/2}$ of each fallout deposit has been plotted (Figure 5B). The August 2006, and 1999-2001 deposits are the largest and tend to be close to the field of the Subplinian and Plinian fallouts. In contrast, the November 2010 is the smallest deposit (Figure 5B).

In terms of magnitude and intensity, the major eruption of August 2006 was the largest in the entire period, reaching 3.7 and 9.0, respectively, on the Pyle (2000) scale which quantifies the power of eruptions, so it can be used in a global classification of these genetic events. Using this approach, Bustillos and Samaniego (2011) observed that: the eruptions of August 2001 are included in the field of "continuous ash clouds"; the eruptions of July 14th (2006), February 2008, May 28th (2010), November 22th (2010) and December 4th (2010) fall in the field of "other explosive eruptions" which refers to all explosive events smaller than Plinian or Subplinian; and, finally, the August 2006 major eruption is in the lower part of Plinian events (Figure 5C). Other eruptions have not been classified with this method due to lack of necessary data.

Variability, Impacts and opportunities from the study of tephra falls

These observations indicate that tephra falls at Tungurahua during the last fifteen years have been produced by different eruptive styles: short-lived explosions, Strombolian eruptions, hydro-volcanic interactions triggering Vulcanian eruptions, and one Subplinian event. Transitions between these eruptive styles have been commonly observed (specially from Vulcanian to Strombolian styles) during the 1999-2014 eruptions, as seen in the variations of tephra components and volcanic phenomena directly observed. While not studied herein, the characteristics (column height, duration, and dispersion of ash) of the February 2014 eruption are descriptive for a major Vulcanian eruption, similar to that on July 14th, 2006). This assumption must be supported with a
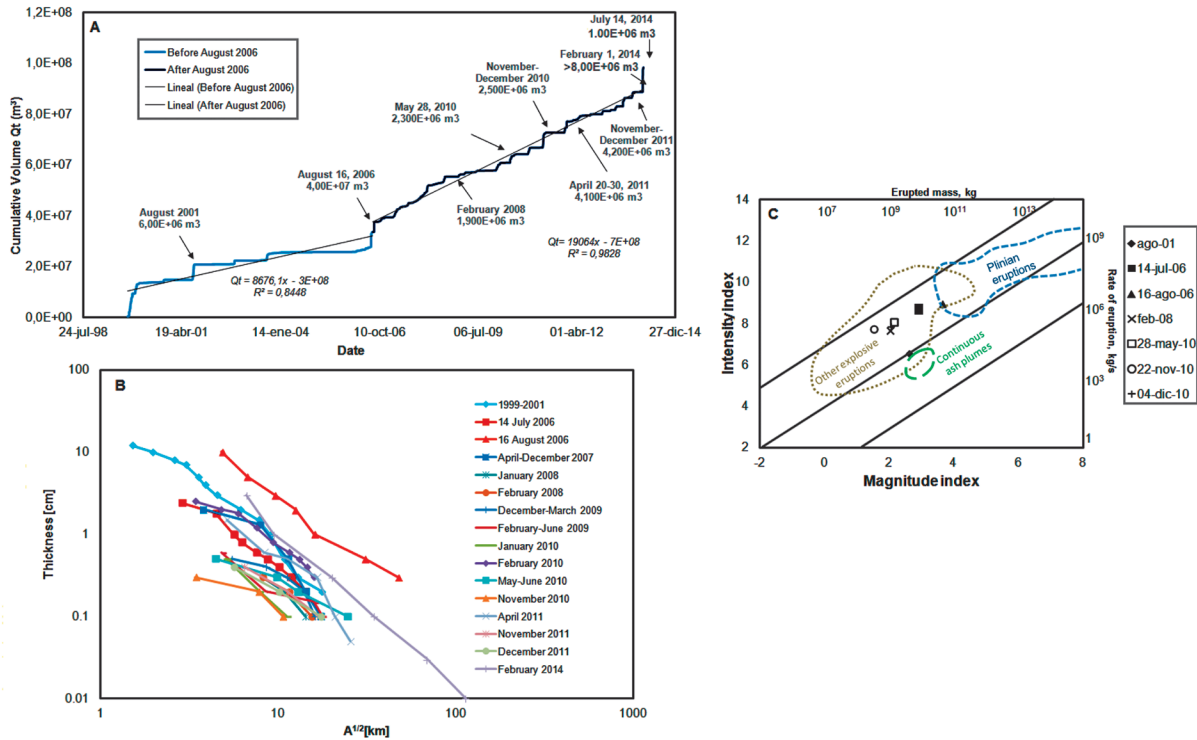
Figure 5. Size of the 1999-2014 eruptions at Tungurahua, A: Cumulative volume of the tephra fallout deposits since 1999, modified from Bustillos *et al*. (2011), Vallejo *et al*. (2014) and unpublished material (J.E. Romero, pers. comm., August 20th, 2014). B: Plot of area vs. thickness following the scheme developed by Pyle (1989) applied to theTungurahua tephra fall deposits. Based on the data from Jaya (2004), Bustillos *et al* (2014), Le Pennec *et al*. (2011), Troncoso *et al*. (2006), Bustillos (2010) and Bernard *et al*. (2013). C: Magnitude and intensity plot (Pyle, 2000) of the largest Tungurahua eruptions before 2014 (Modified from Bustillos and Samaniego, 2011). Areas contouring the different eruption types after Pyle (2000).

successful quantification of emitted materials. While the 1999-2001 deposits are close to the field of the Subplinian eruptions, this is an example of a cumulative tephra of several short-lived eruptions and doesn't represent a single high intensity eruption.

The eruptions of July and August 2006 and May 2010, produced PDCs, representing increased explosivity compared to the Strombolian events that characterized its behavior since the renewal of activity in 1999 (Myers *et al*., 2014). Throughout the events of May 28th and November 22th, 2010, February 4th, 2012, July 14th, 2013, February 1st and April 4th, 2014 a more recurrent and explosive dynamics is evident. This is supported by the increase in Q over time, which could be explained by 1) an increase in frequency of short-lived explosions and 2) recurrence of large-volume explosive events. As reported for recent 2006 and 2010 eruptions (eg. Samaniego *et al*., 2011; Eychenne *et al*., 2013; Myers *et al*., 2014), both short-lived and large-volume eruptive events may be caused by continuous ascent of small, and gas-rich magma batches.

Tephra falls have extensively affected the areas around the volcano (Figure 1c), and sites to the south and west have experienced severe damage to agriculture and infrastructures (eg. Le Pennec *et al*., 2004; Le Pennec *et al*., 2011). House roofs have collapsed under the weight of tephra in addition to the weight of rainwater, and also acidic rain has degraded infrastructures (Le Pennec *et al*., 2011). Close to the volcano in towns such as San Juan, Laurelpamba and Palitahua, which received more than 6 cm of tephra deposits, many houses experienced partial destruction of their roofs by the fall of bomb-sized (11 cm diameter) clasts in 2006. According to IG-EPN reports, rapid rainfall runoff and associated erosion of the pyroclastic deposits caused 795 lahar floods from 2000 to 2010. No fatalities have been reported as consequence of tephra fall, but PDCs killed five people in 2006. Sword-Daniels *et al* (2011) provide information of tephra impacts of Tungurahua eruptions on infrastructure and public services, including impacts on water supplies, wastewater, transportation and agriculture.

While the effects of volcanic ash in human health and life are well-known, stories of social resilience and adaptation are surprising and common at Tungurahua. Worldwide research projects, such as the Strengthening Resilience in Volcanic Areas (STREVA; http://streva.ac.uk/) or the European Commission for Humanitarian Aid (http://ec.europa.eu/index_es.htm) have been working in this area in order to understand the impacts associated with eruptions, help in emergencies, empower communities and local disaster response teams.

Goals of future projects should address the effect of tephra deposition in populated areas, unknown effects of tephra fall, especially on human health, agriculture, livestock and ecosystems. With the training of volcanologists in the use of quick tephra fallout forecast using tools as Ash3D (Schwaiger *et al*., 2014) it may be possible evaluating in near-real time tephra hazards at Tungurahua. We suggest that techniques like the analysis of ash microlite textures and the high-resolution mass analysis of tephra (Eychenne *et al*., 2013), could be extensively used at Tungurahua for the recent, post-2006 eruptive period, as used by Wright *et al*. (2012) for the 1999-2004 Tungurahua eruptions. Analysis of the ejecta of the entire eruptive cycle may contribute not only to understand the dynamics of the Tungurahua eruptions, but it also help improving the prediction of eruptions and increasing the knowledge on the interactions between tephra deposition and ecosystems. It is also recommended to develop interactive platforms (eg. Global Information System, GIS) that can combine tephra, lahar and PDC simulations with civil protection information for risk assessment and management.

Conclusions

The long-lasting eruptive cycle developed by Tungurahua volcano in the period 1999-2015 has consisted in eruptive styles varying from phreatic explosions until Subplinian eruptions, releasing 0.13 km^3 of tephra bulk volume. The 70% of tephra falls associated to these explosive eruptions have affected areas west and west-southwest of the volcano. This review has defined four clearly distinguishable eruptive phases during this period. The components of tephra falls have varied between eruptions reflecting these changes of eruption style: in fact, 1) tephras dominated by a variety of pumice and scoriae, free crystals and less amount of accidental or altered lithics are fed by violent explosive eruptions; 2) an increase in free crystals, decrease of highly

vesicular juveniles and the apparition of Pele's tears are indicators of open vent eruptions, mostly Strombolian in type and 3) deposits with abundance of dense accidental lithics and altered fragments in contrast to the juvenile materials, are most probably of Vulcanian origin. The variability in the components of tephra fall over the time indicates transitional behavior between these styles. The two largest eruptions at Tungurahua during this period of study where in August 2006 and February 2014 reaching a peak of VEI 3. A duplication in the tephra discharge rate since 2006 is noticeable and a increase in the frequency of Vulcanian eruptions with generation of PDCs is observed. By these reasons, to assess tephra fall hazard and impacts at Tungurahua region is mandatory and requires the implementation of a multidisciplinary effort.

Acknowledgements

References

Alfano F., Bonadonna C., Volentik A.C.M., Connor C.B., Wat, S.F.L., Pyle D.M., Connor L.J., 2011. Tephra stratigraphy and eruptive volume of the May, 2008, Chaitén eruption, Chile. *Bull. Volcanol.*, 73, 613-630.

Aspden J., Jemielita R., Litherland M., Bermudez R., Bolaños J., Pozo M., Viteri F., Celleri M., 1994. Geological and Metal Occurrence maps of the Northern Cordillera Real, Metamorphic Belts, Ecuador. British Geological Survey, 11. 1:500000.

Barba D., Arellano S., Ramón P., Mohes P., Alvarado A., Ruiz G., Troncoso L., 2006, Cronología de los Eventos Eruptivos de Julio y Agosto de 2006 del Volcán Tungurahua. in 6tas Jornadas en Ciencias de la Tierra of the Escuela Politécnica Nacional, 177-180, Quito, Ecuador. November.

Bernard B., 2013, Homemade ashmeter: a low-cost, high-efficiency solution to improve tephra field-data collection for

contemporary explosive eruptions. *Journal of Applied Volcanology*, 2, 1, 1–9.

Bernard B., Bustillos J., Wade B., Hidalgo S., 2013, Influence of the wind direction variability on the quantification of tephra fallouts: December 2012 and March 2013 Tungurahua eruptions. *Avances en ciencias e ingenierías*, 5, 1, A14-A21.

Bernard J., Kelfoun K., Le Pennec J.-L., Vallejo Vargas S., 2014, Pyroclastic flow erosion and bulking processes: comparing field-based vs. modeling results at Tungurahua volcano, Ecuador. *Bulletin of Volcanology*, 76, 9.

Bustillos J., 2008, Las Avalanchas de Escombros en el Sector del Volcán Tungurahua. Thesis. Escuela Politécnica Nacional-Quito, Ecuador, 151 p.

Bustillos J., Samaniego P., 2011, Volcán Tungurahua: Tamaño de las erupciones explosivas. 7 más Jornadas en Ciencias de la Tierra of the Escuela Politécnica Nacional, 4p, Quito, Ecuador. November 23-25.

Bustillos J., 2010, Transición del estilo eruptivo durante las erupciones andesíticas en sistema abierto: Contribución al estudio de los depósitos de ceniza del volcán Tungurahua". Master thesis, Nice Sophia Antipolis University, France, 48.

Bustillos J., Guevara A., Hidalgo S., 2013, Los depósitos de ceniza del 04 y 05 de Mayo 2013 en el volcán Tungurahua. *Pyroclastic Flow*, 3, 1, 1-8.

Bustillos J., Ruiz G., Le Pennec J.-L., 2011, Volcán Tungurahua: Cálculo indirecto de material sólido emitido (tefra). 7 más Jornadas en Ciencias de la Tierra of the Escuela Politécnica Nacional, 4p, Quito, Ecuador. November 23-25.

Bustillos J., Mothes P., 2010, Ash falls at Tungurahua volcano: implementation of systematic ash collection for quantifying accumulated volumes. 6th Cities On Volcanoes, Tenerife, Canary Island, Spain. May 3-June 4, 2010.

Bustillos J.E, Romero J.E., Guerrero G., 2014, New field data on the Guagua Pichincha (Ecuador) ~ 900AD Subplinian eruption and its eruptive parameters. *Pyroclastic Flow*, 4, 1, 1-4.

Douillet G.A., Pacheco D.A., Kueppers U., Letort J., Tsang-Hin-Sun È., Bustillos J., Hall M., Ramón P., Dingwell D.B., 2013a, Dune bedforms produced by dilute pyroclastic density currents from the August 2006 eruption of Tungurahua volcano, Ecuador. *Bull. Volcanol.,* DOI 10.1007/s00445-013-0762-x.

Douillet G.A., Tsang-Hin-Sun E., Kueppers U., Letort J., Pacheco D.A., Goldstein F., Von Aulock F., Lavallée Y., Hanson J.B., Bustillos J., Robin C., Ramón P., Hall M., Dingwel D.B., 2013b, Sedimentology and geomorphology of the deposits from the August 2006 pyroclastic density currents at Tungurahua volcano, Ecuador. *Bull. Volcanol.,* DOI 10.1007/s00445-013-0765-7

Douillet G.A., Bernard B., Vallejo S., Gonzalez J.A., Kueppers U., Ramón P., Yepes H., Hidalgo S., Hess K., Mothes P., 2014, Deposits from the 1 February 2014 eruption of Tungurahua volcano (Ecuador). Cities on Volcanoes 8, Jogja, Indonesia, 2p. September 9-13.

Eychenne J., Le Pennec J.-L., Troncoso L., Gouhier M., Nedelec J.-M., 2012, Causes and consequences of bimodal grain-size distribution of tephra fall deposited during the August 2006 Tungurahua eruption (Ecuador). *Bull. Volcanol.,* DOI 10.1007/s00445-011-0517-5.

Eyechenne J., Le Pennec J.L., 2012, Sigmoidal particle density distribution in a subplinian scoria fall deposit. *Bull. Volcanol.,* DOI 10.1007/s00445-012-0671-4.

Eychenne J., Le-Pennec J.L., Ramon P., Yepes H., 2013, Dynamics of explosive paroxysms at open-vent andesitic systems: High resolution mass distribution analyses of the 2006 Tungurahua fall deposit (Ecuador). *Earth Planet. Sci. Lett.,* 361, 343-355.

Hall M., Robin C., Beate B., Mothes P., Monzier M., 1999, Tungurahua Volcano, Ecuador: structure eruptive history and hazards. *J. Volcanol. Geotherm. Res.*, 91,1-21.

Hall M., Steele A.L., Mothes P.A., Ruiz M.C., 2013, Pyroclastic density currents (PDC) of the 16–17 August 2006 eruptions of Tungurahua volcano, Ecuador: Geophysical registry and characteristics. *J. Volcanol. Geotherm. Res.*, 265, 78-93.

Jaya D., 2004, El colapso del volcán Tungurahua en el Holoceno Superior: Análisis de estabilidad y dinamismos explosivos asociados. Thesis. Escuela Politécnica Nacional, Quito, Ecuador.

Le Pennec J-L., Jaya D., Samaniego P., Ramón P., Moreno Yánez S., Egred J., Van Der Plicht J., 2008, The AD 1300-1700 eruptive periods at Tungurahua volcano, Ecuador, revealed by historical narrative, stratigraphy and radiocarbon dating. *J. Volcanol. Geotherm. Res*., 176, 70-81.

Le Pennec J-L., Hall M., Robin C., Bartomioli E., 2006, Tungurahua Volcano, Late Holocene Activity. Field Guide, 4th Cities on Volcanoes. Quito-Ecuador, January.

Le Pennec J-L., Ruiz G., Mothes P., Hall M., Ramón P., 2004, Estimaciones del volumen global del depósito de ceniza de la erupción de agosto del 2001 del volcán Tungurahua. *Investigaciones en geociencias*, 1, 14-18.

Le Pennec J-L., Ruiz G., Ramón P., Palacios E., Mothes P., Yepes H., 2011, Impact of tephra fall in Andean communities: The influences of eruption size and weather conditions during the 1999-2001 activity of Tungurahua volcano. *J. Volcanol. Geotherm. Res*., 217-218, 91-103.

Litherland M., Egüez A., 1993, Mapa Geológico de la República del Ecuador, 1/1,000,000. British Geological Survey (Keyworth, Nottingham) and CODIGEM (Quito, Ecuador), Quito.

Molina I., Kumagai H., Le Pennec J.L., Hall M., 2005, Three-dimensional P-Wave velocity structure of Tungurahua volcano, Ecuador. *J. Volcanol. Geotherm. Res*., 147, 144-156.

Myers M.L., Geist D.J., Rowe M.C., Harpp K.S., Wallace P.J., Dufeck J., 2014, Replenishment of volatile-rich mafic magma into a degassed chamber drives mixing and eruption of Tungurahua volcano. *Bull. Volcanol*., DOI 10.1007/s00445-014-0872-0

Narvaez D., Bernard B., Hidalgo S., Leibrandt S., Le Pennec J.-L., Eyechenne J., Douillet G.A., 2014, Eruptive dynamics based on ash sequence analysis: the example of March and July 2013 eruptive phases at Tungurahua volcano, Ecuador. 8th Cities on Volcanoes, Jakarta, Indonesia. September 9-13.

Newhall C., Self S., 1982, The volcanic explosivity index (VEI): An estimate of explosive magnitude for historical volcanism. *J. Geophys. Res.,* 87, 1231-1238.

Pyle D.M., 1989, The thickness, volume and grainsize of tephra fall deposits *Bull. Volcanol.,* 51, 1-15.

Pyle D.M., 2000, Sizes of Volcanic Eruption. Encyclopedia of Volcanoes. Academy Press. Part II, pp 263-269. San Diego California.

Romero J.E. on the volume of the April 4th, 2014 tephra fall deposit (personal communication, August 20th, 2014).

Ruiz A.G., Le Pennec J.L., Palacios E., Hall M., Yepes H., 2006, Indirect estimation of ash fall volume deposited near Tungurahua volcano (Ecuador) from Oct. 1999 to Dec. 2004: in 4th Cities on Volcanoes, Quito, Ecuador. January.

Samaniego P., Le Pennec J.-L., Robin C., Hidalgo S., 2011, Petrological analysis of the pre-eruptive magmatic process prior to the 2006 explosive eruptions at Tungurahua volcano (Ecuador). *J. Volcanol. Geotherm. Res*., 199, 1–2, 69–84.

Steffke A., Fee D., Garces M., Harris A., 2010, Eruption chronologies, plume heights and eruption styles at Tungurahua volcano: Integrating remote sensing techniques and infrasound. *J. Volcanol. Geotherm. Res.*, 193, 143-160.

Schwaiger H.F., Denlinger R.P., Mastin L.G., 2012, Ash3d: A finite-volume, conservative numerical model for ash transport and tephra deposition, *J. Geophys. Res*., 117, B04204, doi:10.1029/2011JB008968.

Sword-Daniels V., Wardman J., Stewart C., Wilson T., Johnston D., Rossetto T., 2011, Infrastructure impacts, management and adaptations to eruptions at volcan Tungurahua, Ecuador, 1999-2010, GNS Science Report, 24, 73p.

Troncoso L., Le Pennec J-L., Jaya D., Valle A., Mothes P., Arrais S., 2006, Depósitos de caída de ceniza producidos durante las erupciones del volcán Tungurahua, 14 de julio y 16 de agosto de 2006. 6tas Jornadas en Ciencias de la Tierra of the Escuela Politécnica Nacional, 181-184, Quito, Ecuador. November.

Vallejo S., Naranjo F., Ramón P., Yépez H., Hidalgo S., Anzieta J., Bernard B., Narváez D., Mothes P., Doulliet G.A., 2014, The vulcanian eruption of February 1st, 2014 at Tungurahua Volcano, Ecuador. Cities on Volcanoes 8, Jogja, Indonesia, 2p. September 9-13.

Walker G.P.L., 1980, The Taupo pumice: product of the most powerful known (ultraplinian) eruption. *J. Volcanol. Geotherm. Res.,* 8, 69–94.

Wilson H.M.N., Cashman K.V., Mothes P.A., Hall M., Ruiz A.G., Le Pennec J.L., 2012, Estimating rates of decompression from textures of erupted ash particles produced by 1999–2006 eruptions of Tungurahua volcano, Ecuador. *Geology*, doi:10.1130/G32948.

The Mexican Meteor Network: A Preliminary Proposal

Guadalupe Cordero-Tercero*, Fernando Velázquez-Villegas, Carlos Francisco Vázquez-Hernández, José Luis Ramírez-Cruz, Alejandro Arévalo-Vieyra, Asahel Mendoza-San-Agustín and Fernando Camacho-Martínez

Resumen

El estudio de la entrada a la atmósfera terrestre de material asteroidal y cometario tiene importancia científica y social. La observación y estudio del impacto de meteoroides con nuestro planeta es una forma de estudiar geofísica y geología planetarias sin naves espaciales. En este artículo se muestran los avances de la instalación de la Red Mexicana de Meteoros (Citlalin Tlamina) cuyo objetivo, a mediano y largo plazo, es poder cubrir todo el territorio nacional con estaciones que nos permitan registrar la entrada de meteoroides a la atmósfera terrestre. Con esto se busca: a) estudiar en detalle la interacción meteoroide-atmósfera, b) determinar propiedades físicas de los impactores; c) analizar flujos y desviaciones del radiante de las lluvias de estrellas conocidas, d) encontrar o ratificar nuevas lluvias de estrellas; e) recuperar y estudiar meteoritas, f) estudiar la interacción de la onda de choque con el suelo mediante el análisis de sismogramas; g) informar en tiempo real (o casi) a las personas la ocurrencia de bólidos y fragmentación de meteoroides en la atmósfera, evitando el miedo hacia este tipo de fenómenos y servir de apoyo a Protección Civil y h) encontrar áreas de oportunidad que puedan hacer uso de las imágenes captadas por las cámaras (meteorología, migración de aves, etc.). En este trabajo se muestra el prototipo de la base que albergará las cámaras y cuyo propósito es protegerlas del medio ambiente, evitar la condensación dentro de los contenedores de las cámaras y mantenerlas a una temperatura inferior a los 25 °C.v.

Palabras clave: meteoro, meteorita, meteoroide, cuerpos pequeños, red de cámaras, Protección Civil.

Abstract

The study of asteroidal and cometary material entering into Earth's atmosphere has scientific and social importance. The observation and study of the impact of meteoroids with our planet is a way of studying geophysics and planetary geology without spaceships. This article describes the progress of the installation of the Mexican Meteor Network (Citlalin Tlamina). At medium and long term, the aim of this network is to cover the entire national territory with stations that allow us to record the entry of meteoroids into Earth's atmosphere. This seeks to: a) study the meteoroid-atmosphere interaction, b) determine impactor's physical properties; c) analyze flows and Radiant deviations of known meteor showers, d) find or ratify new meteor showers; e) recover and study meteorites, f) study the interaction of the shock wave with the ground by analyzing seismograms; g) report people in real time (or near) the occurrence of fireballs and fragmentation of meteoroids in the atmosphere, avoiding the fear of this phenomenon and provide support for Civil Protection, h) find areas of opportunity that can use the images captured by the cameras (weather, bird migration, etc.). In this paper, it is shown the prototype of the base to house the cameras whose purpose is to protect them from the environment, prevent condensation within the container and keep the cameras below 25 °C.

Key words: meteor, meteorite, meteoroid, small bodies, video network, Civil Protection.

G. Cordero-Tercero*
Departamento de Ciencias Espaciales
Instituto de Geofísica
Universidad Nacional Autónoma de México
Circuito de la Investigación Científica s/n
Ciudad Universitaria
Delegación Coyoacán, 04510
México D.F. México
*Corresponding autor: gcordero@geofisica.unam.mx

F. Velázquez-Villegas
C. F. Vázquez-Hernández
J. L. Ramírez-Cruz
A. Arévalo-Vieyra,
A. Mendoza-San-Agustín
F. Camacho-Martínez
Centro de Ingeniería Avanzada
Universidad Nacional Autónoma de México
Circuito de la Investigación Científica s/n
Ciudad Universitaria
Delegación Coyoacán, 04510
México D.F. México

Introduction

When a comet, asteroid or meteoroid collides with a planet several things can happen depending on the mass, velocity and composition of the object, if the planet or moon has an atmosphere or not, and the angle of impact. In airless bodies, like Mercury or the Moon, all objects that strike their surfaces produce impact craters whose sizes range from centimeters to hundreds and even thousands of kilometers across. In bodies with atmosphere, the encounter with a meteoroid or small body (asteroid or comet) can produce impact craters, meteorites, meteors and fragmentation of the original body, depending on the kinetic energy of the object.

Meteors, also called shooting stars, are bright trails in the sky produced by the heating and incandescence of micrometeorites and meteoroids in the terrestrial atmosphere. A meteoroid is asteroidal o cometary material whose size is between 2 mm and 1-10 meters long (Ceplecha *et al*., 1998; Rubin and Grossman, 2010). These objects generally evaporate at heights between 80 and 120 km (Glass, 1982). Objects of less than 2 mm are known as micrometeorites (Hutchinson, 2004). If the brightness of the meteor outshines the planet Venus (magnitude - 4), the phenomenon is called bolide or fireball (Trigo-Rodríguez *et al*., 2005). Objects between 0.05 mm and 20 cm in diameter produce meteors (Ceplecha *et al*., 1998) while objects larger than 1 m usually produce fireballs whose shine last from a second up to 5-10 seconds (Shumilov *et al*., 2003; Trigo-Rodríguez *et al*., 2005).

If a meteoroid, or a fragment of it, survives atmospheric ablation and can be recovered on the ground, that piece is called a meteorite. Meteorites can be classified according to their materials or according to their origin. Following the first criterion, they fall into one of three types: iron (iron-nickel), stone (silicates) and stony-iron (iron, nickel and silicates) (Weisber, 2006). According to their origin, meteorites are classified into two groups; differentiated and undifferentiated meteorites. Each one of these groups has subdivisions. Undifferentiated meteorites can be chondrites (which in turn are divided into 5 types) and primitive achondrites. Differentiated meteorites are divided into achondrites, iron meteorites and stony-iron meteorites (Cervantes, 2009). The study of meteorites has been and will be very important for understanding the physical and chemical conditions that existed inside the primitive solar nebula, to estimate the age of formation of the solar system and to model the interiors of planets and moons (Hutchinson, 2004; Taylor 2001; Pater and Lissauer, 2001).

The impact velocity of a meteoroid or a small body with another planetary body depends on the escape velocity of the latter, its heliocentric orbital velocity and velocity of the impactor at the heliocentric distance of the impacted body. For Earth, the minimum speed of impact is the escape velocity 11.2 km / s, and the maximum is 72.8 km / s. When meteoroids and asteroids up to a few tens of meters in diameter interact with the Earth's atmosphere, they slow down as they go into more dense layers. The friction between a meteoroid (or asteroid or comet) and air, heat the object up to the material is ablated. The aerodynamic pressure of the atmosphere on small asteroids or meteoroids can be greater or equal to their internal strength; in this case the object fragment suddenly in the atmosphere producing shock waves.

The fragmentation of the object is not immediate; the pressure wave must be transmitted into the body. It occurs fairly quickly because the propagation velocity of such waves is between 2930 m s^{-1} and 5110 m s^{-1}, even 6260 m s^{-1} in iron meteorites (Flynn *et al*., 1999). At first, the fragments have the same shock wave, but as they separate laterally, more space is among them until each fragment acquires its own shock wave. When this sudden separation occurs it is said that the object explodes (Melosh, 1989; Hills and Goda, 1993).

When the object that is broken is tens of meters long, its fragments may hit the ground with enough kinetic energy to create several impact craters (Passey and Melosh, 1980). On our planet there are around a dozen of such structures, which are known as fields of craters.

During the XX and XXI centuries, a series of events showed the importance of collisions between planets and minor planets (comets and asteroids). On Earth, we can mention three interesting events: Tunguska, Curuça and Chelyabinsk. On the morning of June 30, 1908, an object of between 50 and 100 m suddenly broken at a height of 5-10 km with an energy of 10-50 Mt TNT (Svetsov and Shuvalov, 2008). The blast completely destroyed the material so none impact crater was formed, but the shock wave produced during the fragmentation had the enough energy to break down trees inside an area of 2150 km^2 (Farinella *et al*., 2001). That same shock wave produced an earthquake of magnitude 4.7 (Ben-Menahem, 1975). A similar phenomenon, the Curuça event,

occurred in the Brazilian Amazon on August 13, 1930 (Bailey *et al*., 1995; Reza *et al.*, 2004). This event did not created impact craters, at least not recognizable currently but the energy of the explosion was much more modest than Tunguska's, probably some few kilotons of TNT. It occurred in a sparsely populated area around the Curuça river, near the border between Brazil and Peru. At this point, it is important to emphasize that this event is known thanks to a catholic missionary who arrived at the scene a few days after, and made a report that was published in the Vatican newspaper in 1931 (Cordero and Poveda, 2011). A more recent event occurred on 15 February, 2013 on Chelyabinsk region, Russia. It is estimated that a rocky (chondritic) asteroid of about 19.8 m in diameter with an initial kinetic energy between 470 and 590 kT entered into the Earth's atmosphere where it suffered a couple of fragmentations above 27 km altitude. The shock wave, produced by the explosion of this asteroid in the atmosphere, caused cracks in walls and broken windows. Shattered glasses hurt more than one thousand and five hundred persons (Popova *et al*., 2013).

On February 10, 2010, near the border between Puebla and Hidalgo States, Mexico, people heard an explosion that alarmed the population. Some kilometers away, some persons observed a bolide. This event may have been the sudden fragmentation of an object in the atmosphere. It is estimated that the explosion could have released an energy of a few kilotons. While studying this event we realized the social value of alerting the population about such phenomena because it cause great fear and can represent many hours of lost work for members of Civil Protection (Cordero *et al*., 2011). On February 22, 2011 another fireball was observed in Mexico, this time near the border between Aguascalientes and Zacatecas. This last event reaffirmed the need for a continuous monitoring system of meteors and fireballs.

There are several ways to detect the entry of meteoroids and small bodies in the Earth's atmosphere: naked eye, photographs, videos, radar, lidar and infrasound. Putting aside the observations with the naked eye, which is obviously the oldest technique (Yang, *et al*., 2005), systematic observations of meteors using cameras have been conducted since the 1950s. The first observations were made in Czechoslovakia, and then by three other camera networks in Europe, USA and Canada (Oberst, 1998). The next step was the use of networks of video cameras that allow monitoring the sky in a more systematic

way, among such networks are the European meteor video observation network (EDMON) and the IMO Video Meteor Network that include networks in several European countries. There are also the Spanish Meteor Network (SPMN) (Trigo-Rodríguez *et al*., 2004) and the Fireball Recovery and Interplanetary Observation Network (Fripon), this one is a 100 camera network established on France. In America there is the North American All-Sky Camera Network with stations in Canada, United States of America and one station in Mexico (Hermosillo).

Currently, we are working to have the Mexican Meteor Network whose informal name is Citlalin Tlamina (« meteor » in nahuatl language). With this network, we want to a) Determine values of meteoroid's parameters to be used in numerical modeling of the dynamics of these objects through Earth's atmosphere, b) determine the conditions under which seismic waves are created due to the shock wave that is produced by the fragmentation of a meteoroid in the atmosphere; c) understand the coupling of atmospheric shock wave with the ground, and the information that can be obtained about height and energy of the explosion, d) know the region meteoroids come from (main belt asteroids, Earth's neighborhood, etc.); e) extrapolate meteoroid trajectory to retrieve meteorites, f) study meteorites, g) study known and probable meteor showers ; h) comunicate the entry of large meteoroids to Civil Protection to help them to mange the situation with people and retrieving of meteorites or space debris, and i) find areas of opportunity, looking for researches interested in our data to study weather, complex phenomena, etc.

Problem Statement

Buil (1994) gives a series of recommendations to choose the most suitable photographic equipment and lenses to observe meteors. After looking for some options, we decided to use the equipment that José María Madiedo-Gil and Josep Trigo-Rodríguez recommended to us. They work in the Spanish Meteor Network (SPMN) and they have used several types of cameras and lenses to observe meteors since 2004 (Trigo *et al*., 2004). So to set up the Mexican Meteor Network, we acquired WAT-902 H2 Ultimate (EIA) cameras and lenses with an image size of 1/3 "and a focal length 0f 0.3 to 8 mm because this equipment has been very useful to observe meteors due to its efficiency (Figure 1) (Madiedo and Trigo, 2008; Madiedo *et al*., 2009; Madiedo *et al*., 2010; Madiedo *et al*., 2013). Once we have this equipment, the next action was to design a base to protect the

cameras. For this purpose, a monitoring station was designed with five cameras to the horizon in 360° and one camera towards the zenith. We chose to form a station with 6 cameras because, during previous observation campaigns, we realized that 4 cameras were not enough to cover the entire free sky. According to our observations, we needed 6 cameras to get it. The fields of vision of these 6 cameras overlap a bit, but this, far from being a problem is an advantage as it is likely that a meteor can be seen by two or more cameras at each station. Conditions of high temperature and humidity were considered in our design. The aim was then design the mechanical interface of the monitoring station used to observe meteors and fireballs entering the Earth's atmosphere.

The requirements for the interface were: a) To protect cameras from the environment, b) to allow free vision, c) to keep the operation temperature of the cameras (about 25°C), d) to keep the relative humidity and temperature around the cameras in a specific range to avoid condensation (75% of relative humidity, a temperature of 25°C), e) to allow elevation of the cameras between 40° and 50°, f) low cost, and g) low maintenance. At first, it was thought to use the cameras to observe meteors at night, but in the near future the base will be modify to perform daytime observations. No other factors were considered, but more constraints can be regarded according to how the system works.

Methodology

We generated some conceptual solutions for each requirement. After evaluating, the following solutions were selected because of their simplicity, low cost and easy manufacture:

In order to protect the cameras from the environment, acrylic cages were used, because it is a low cost and simple manufacture material

(Figure 2). Another solution, perhaps more aesthetic, was to use a dome made of acrylic, but it was about 3 times more expensive and more difficult to solve the problem of condensation inside.

To have an adequate view, the front face of each cage was made of glass.

In order to keep a functional temperature for the cameras, they were attached to an aluminum plate that dissipates heat. Besides, this plate is cooled by a fan that produces forced convection (Figure 3). Also we implemented over the cages a cover of reflective material to reduce heating because of Sun light. The first option was to implement an environmental conditioning system but, once again, the cost was the main issue.

Silica gel was used to absorb humidity and to avoid condensation inside cages. The mass quantity of silica that is necessary to absorb humidity inside the cage is 15 mg. To prevent ingress of water vapor, joints between the acrylic cages and glass were sealed with silicone, and joints between acrylic cages and their metal base were sealed placing a plastic seal and silicone. We thought to use an electric air dryer system but it was more complicated for maintenance.

We implemented round rails and hinges to allow camera elevation (Figure 4).

To manage the video signal from the cameras, we use a frame grabber of EPIX (PIXCI SV5). Each camera is connected to a single PC to prevent interference of signals from two or more cameras.

To get data, we use UFOCapture software which allows further adjustments than the software attached to PIXCI SV5 grabbers. At the moment, all data is stored in internal

Figure 1. Camera and lens used in the Mexican Meteor Network.

disks of each PC, then this information is down into an external disk. After that, videos are classified (clouds, rain, lightning, insects, etc.) or deleted (if they lack of scientific interest). We only analyzed videos of meteors.

First design and preliminary results

The monitoring station designed has: a) Individual compartments or cages for each camera, b) humidity cages that contain silica gel, c) individual and independent elevation of each horizontal camera, and d) cooling system

(Figure 5). This arrangement allows to move and provide maintenance of each camera independently (Figure 6).

First meteor shower report.

The eta aquarids is an annual meteor shower due to the entry of Halley comet particles into Earth´s atmosphere. These particles ablate totally in the atmosphere at the same time they produce easily detectable meteors. The maximum flow of the fall of these particles occurred this year on the morning of May 6th.
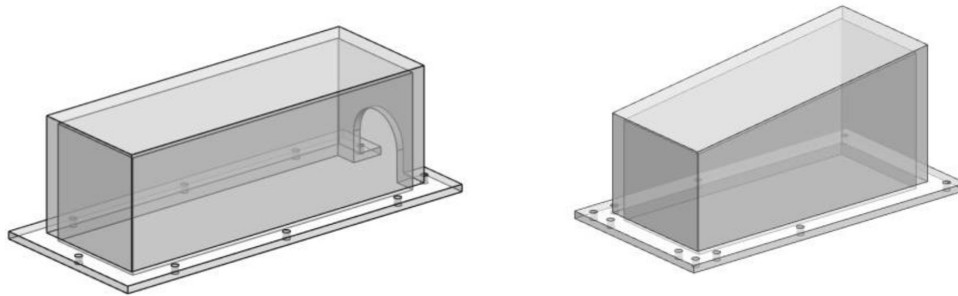
Figure 2. Cages to protect cameras.
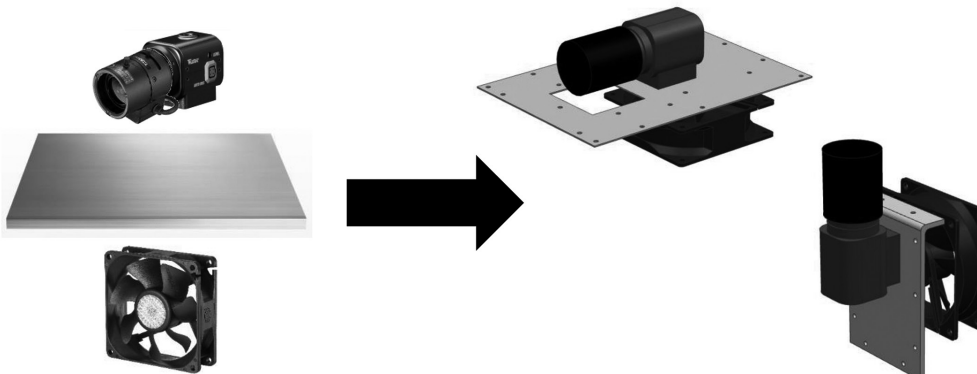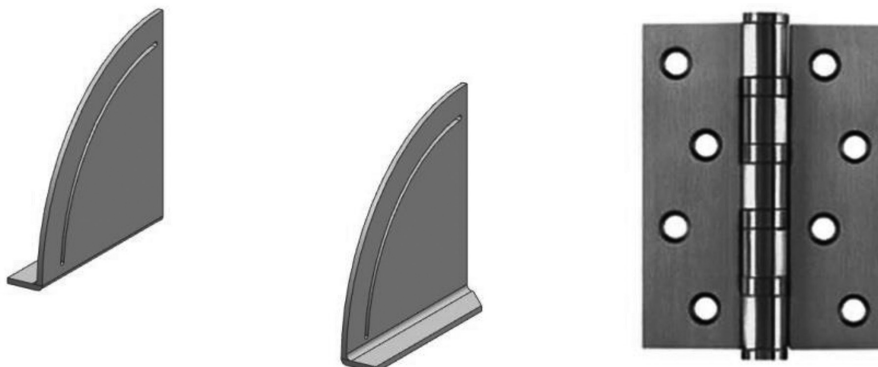

Figure 3. Cameras Platform.

Figure 4. Round rails and hinges.

Taking the advantage of this event, we used the instrument described above. We put the first station of the Mexican Meteor Network (Citlalin Tlamina) on the roof of the Institute of Geophysics at UNAM (Universidad Nacional Autónoma de México) in Mexico City to observe these meteors on the night of May 6th (Fig. 7). Due to weather conditions, we recorded only two meteors, one of them is shown in the Figure 8. To obtain this figure, we use the Maxim DL software. Since that day, we have made a series of night observations. This has allowed us to realize about the strengths and weaknesses of the design, and it has shown us the direction of future work.
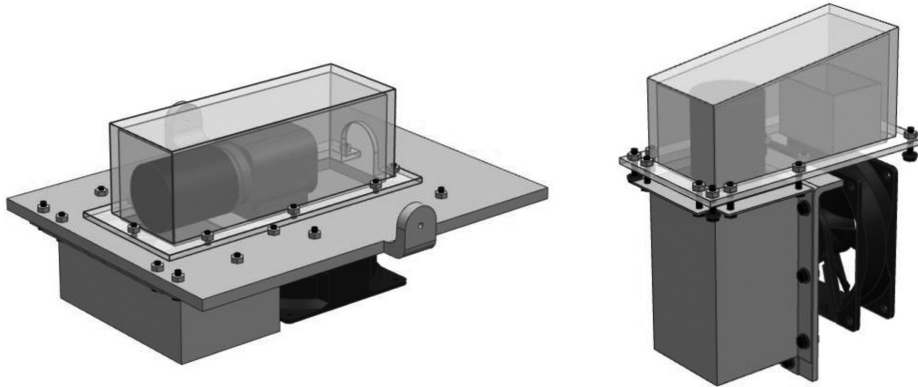
Figure 5. Final arrangement for the vertical and horizontal cameras.
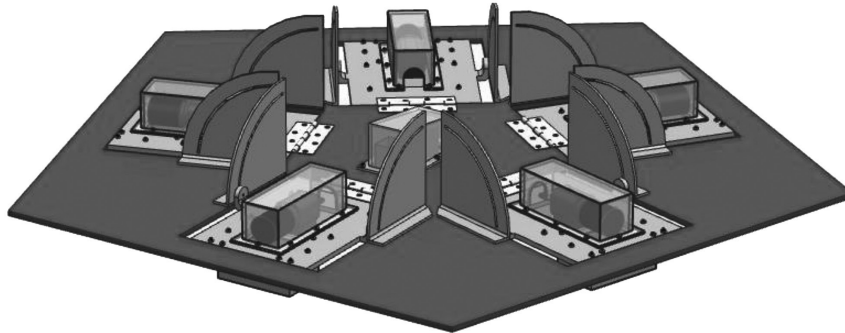
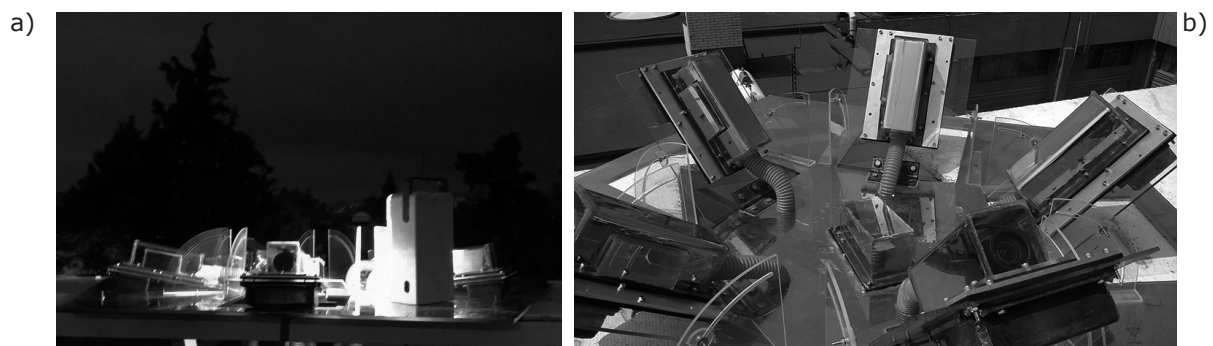**Figure 6.** Final design and layout of cameras.

a)

b)

Figure 7. a) View of the first station of Citlalin Tlamina the night of May 6, 2015, b) approach to the base.

Figure 8. Image of an eta aquarids meteor (trace indicated by the white arrow).

2014/09/18 07:03:55.8 0285   00039 V00008+009 UFOCaptureV2

Conclusions.

The monitoring station design protects the cameras from environment, ensuring their correct operation and allowing the observation of meteors and fireballs produced by meteoroids and small asteroids that enter into the Earth's atmosphere. The covers of reflective material used over the acrylic cages improve their durability despite the sun light. The fans and the silica gel maintain the environment inside the cages in adequate conditions for the cameras performance. It should be mentioned that our main constraint was cost and, as a consequence of that, the station needs to be monitored as regularly as possible in order to decide when to change the acrylic cages or to add or replace the silica gel.

The cost of the monitoring station is very low, because of the low cost materials used and its simple configuration.

The monitoring stations could be located almost anywhere due to cameras are completely isolated from the external environment, avoiding inclement weather inside the cages.

The design is being tested since May 6, 2015, day when we observed the eta Aquarids. On this occasion only two meteors were recorded because bad weather conditions (very cloudy sky). In the coming months, the current base will be improved to solve some problems and a new base will be design based on experience.

References

Ben-Menahem A., 1975, Source Parameters of the Siberian Explosion of June 30, 1908, from Analysis and Synthesis of Seismic Signals at Four Stations. *Phys. Earth Planet. Int.*, 11, 1-35.

Buil C., 1994, Meteors, in *The Observer's Guide to Astronomy*. P. Martinez (Ed.), Vol. 2., 1st ed. Cambridge University Press, 632-711.

Ceplecha Z, Borovička J., Elford W.G., Revelle D.O., Hawkes R.L., Porubčan V., Šimek M., 1998, Meteor Phenomena and Bodies. *Space Science Reviews*, 84, 327-471.

Cervantes de la Cruz K.E., 2009, Estudio petrológico de los condros de las meteoritas

condríticas mexicanas Cuartaparte, Cosina, y Nuevo Mercurio: origen y evolución de dichas estructuras. Ph. D. Thesis. México, UNAM, 6-7.

Cordero G., Cervantes de la Cruz K., Gómez E., 2011, The bolide of February 10, 2010: Observations in Hidalgo and Puebla, Mexico. *Geofísica Internacional*, 50-1, 23-30.

Cordero G., Poveda A., 2011, Curuça 1930: A probable mini-Tunguska? *Planetary and Space Science*, 59, 10-16.

Farinella P., Foschini L., Froeschlé Ch., Gonczi R., Jopek T.J., Longo G., Michel P., 2001, Probable asteroidal origin of the Tunguska cosmic body. *Astronomy and Astrophysics*, 377, 1081-1097.

Flynn G.J., Klöck W., Krompholz R., 1999, Speed of sound, elastic and shear modulus measurements on meteorites: implications for cratering and disruption of asteroids. *LPSC XXX*. 1073.pdf.

Glass B.P., 1982, Introduction to planetary geology. EEUU, Cambridge, 469 pp.

Hills J.G., Goda M.P., 1993, The Fragmentation of Small Asteroids in the Atmosphere. *The Astronomical Journal*, 05, 1114-1144.

Hutchinson R., 2004, Meteorites. A petrologic, chemical and isotopic synthesis. Cambridge, EEUU 524 pp.

Madiedo J.M., Trigo-Rodríguez J.M., 2008, Multi-station video orbits of minor meteor showers. *Earth Moon Planet*, 102, 133-139.

Madiedo J.M., Trigo-Rodríguez J.M., Alonso J., Zamorano J., Ocaña F., Docobo J.A., Pujols P., Lacruz J., 2009, The Spanish Meteor Network (SPMN): full coverage of the Iberian Peninsula by mean of high-sensitivity CCD video devices. *European Planetary Science Congress Abstracts*, Vol. 4.

Madiedo J.M., Trigo-Rodríguez J.M., Ortiz J.L., Morales N., 2010, Robotic systems for meteor observing and Moon impact flashes detection in Spain. *Advances in Astronomy*, 5 pp.

Madiedo J.M., Trigo-Rodriguez J.M., Konovalova N., Ortiz J.L., Castro-Tirado A.J., Alonso-Azcárarte J., Lacruz J., Cabrera-Caño J., 2013, Orbit, emission spectrum, and photometric analysis of two flickering sporadic fireballs.

Astronomy and Astrophysics, 555, A149, 8 pp.

Melosh J., 1989, Impact Cratering. A geologic process. Oxford, EEUU, 256 pp.

Oberst J., Molau S., Heinlein D., Gritzner C., Schindler M., Spurny P., Ceplecha Z., Rendtel J., Betlem H., 1998, The "European Fireball Network": Current status and future prospects. *Meteoritics & Planetary Sciences*, 33, 49-56.

Passey Q.R., Melosh H.J., 1980, Effects of atmospheric breakup on crater field formation. *Icarus*, 42, 211-233.

Pater de I., Lissauer J.J., 2001, Planetary sciences. Reino Unido, Cambridge, Capítulo 8, pp. 307-330.

Popova Olga P., *et al*., 2013, Chelyabinsk airburst, damage assessment, meteorite recovery, and characterization. *Science*, 342, 29 November, 1069-1073.

Rubin A.E., Grossman J.N., 2010, Meteorite and meteoroid:New comprehensive definitions. *Meteorotics & Planetary Sciences*, 45, no. 1, 114-122.

Shumilov O.I., Kasatkina E.A., Tereshchenko E.D., Kulichkov S.N., Vasil'ev A.N., 2003, Detection of Infrasound from the Vitim Bolide on September 24, 2002. *JETP Letters*, 77, no. 2, 115-117.

Svetsov V., Shuvalov V., 2008, Tunguska Catastrophe of 30 June 1908. In Catastrophic Events Caused by Cosmic Objects., V. Adushkin e I. Nemchinov (eds.) Springer, Países Bajos, pp. 227-266.

Taylor S.R., 2001, Solar system evolution. A new perspective. Reino Unido, Cambridge. Capítulo 6, pp. 105-161.

Trigo-Rodríguez J.M., Castro-Tirado A.J., Llorca J., Fabregat J., Martínez V.J., Reglero V., Jelínek M., Kubánek P., Mateo T., de Ugarte Postigo A., 2004, The development of the Spanish fireball network using a new all-sky CCD system. *Earth, Moon, and Planets*, 95, 553-567.

Trigo-Rodríguez J.M., Llorca J., Docobo J.A., Blanco-Lanza S., Rodríguez-Baquero O.A., 2005, Bólidos: Cómo estudiarlos y distinguirlos de otros fenómenos luminosos. *Astronomía*. 75, 68-77.

Weisber M.K., McCoy T.J., Krot A.N., 2006, Systematics and evaluation of meteorite classification. In *Meteorites and the Early Solar System II*, D.S. Lauretta and H.Y. McSween Jr. (eds.) University of Arizona Press, Tucson, 19-52.

Yang H-J., Park Ch., Park M-G., 2005, Analysis of historical meteor and meteor shower records: Korea, China and Japan. *Icarus*, 175, 215-225.

Differences in Epicentral Location of Mexican Earthquakes between Local and Global Catalogs: An update

Vala Hjörleifsdóttir*, Shri Krishna Singh and Allen Husker

Resumen

Las diferencias en las localizaciones epicentrales entre catálogos locales y globales para sismos ocurridos en la zona de subducción mexicana fueron, primeramente, observados en 1980, con base en unos cuantos eventos bien estudiados. En este escrito se comparan las localizaciones de dos catágolos locales; (1) un catálogo reciente de alta precisión para la zona de Guerrero y (2) el catálogo del Servicio Sismológico Nacional (SSN), contra el catálogo global del United States Geological Service (USGS). Encontramos que en promedio las localizaciones epicentrales reportadas en los catálogos globales, para sismos de magnitudes mayores a 5, generados en la zona de subducción mexicana, se encuentran 26 km en dirección N54ºE comparados con los reportados en catálogos locales. Investigamos cómo el error varía para diferentes tipos de sismos en Guerrero y cómo éstos mismos varían a lo largo de la trinchera, desde el estado de Jalisco hasta Chiapas. En promedio, las diferencias son mayores para sismos inversos ocurridos cerca de la trinchera y para eventos ocurridos en Michoacán. Las diferencias son mayores en promedio para eventos de magnitud mayor. Existe una compensación entre la distancia a la trinchera y el tiempo, lo cual indica una baja resolución para estos parámetros, debido a la falta de estaciones ubicadas en el Océano Pacífico. Las diferencias entre las localizaciones pueden ser atribuidas a un modelo sistemático en la estructura de velocidad para el manto, consistente con trayectorias rápidas al noreste y trayectorias lentas relativas al suroeste.

Palabras clave: Sismicidad, zona de subducción mexicana, localización epicentral.

Abstract

Differences in epicentral locations between local and global catalogs for earthquakes in the Mexican subduction zone were first observed to be biased in the 1980s, based on a few well studied events. In this study we compare locations between two local catalogs; (1) a recent high precision catalog of events in the state of Guerrero and (2) the catalog of the Servicio Sismológico Nacional (SSN), to the global catalog of the United States Geological Service (USGS). We find that on average epicentral locations in the global catalog of earthquakes larger than M 5 in the Mexican subduction zone are 26 km towards N54°E of those in the local catalogs. We investigate how the errors vary for different types of earthquakes in Guerrero, and how they vary along the trench, from the state of Jalisco to the state of Chiapas. The average differences are largest for thrust events occurring close to the trench, and for events in Michoacán. The differences are greater on average for large earthquakes than for small. There is a trade-off between the distance from the trench and timing, suggesting a poor resolution of these parameters, due to the lack of stations the Pacific Ocean. We attribute the differences in locations to systematic patterns in the velocity structure of the mantle, with consistently fast paths to the northeast and relatively slow paths towards the southwest.

Key words: seismicity, mexican subduction zone, earthquake location.

V. Hjörleifsdóttir*
S. Krishna Singh
A. Husker
Instituto de Geofísica
Universidad Nacional Autónoma de México
Circuito de la Investigación Científica s/n
Ciudad Universitaria
Delegación Coyoacán, 04510
México D.F. México
*Corresponding autor: vala@geofisica.unam.mx

Introduction

In the immediate aftermath of an earthquake, the location of the hypocenter helps identifying regions most affected by the event and its tsunamigenic potential, until fault slip distributions (obtained from analysis of seismic waveforms), as well as aftershock locations, become available. However, locating large earthquakes quickly from local data is often difficult as the duration of the P wave can be similar to or larger than the separation between the P and S waves, which can lead to large errors in S-wave picks. For this reason, hypocenters obtained from teleseismic data, if accurate, can be helpful for quick identification of regions severely affected by an earthquake.

In the early 1980s it was observed that earthquakes in the Mexican subduction zone were systematically mislocated in global catalogs, such as the PDE and ISC catalogs (Singh *et al*. 1980, Havskov *et al*. 1983). A comparison of hypocenter locations obtained by carefully analyzing locally recorded data, to those obtained from teleseismic data, showed that the mislocation was typically about 35 km towards N 35° - 45E° (Singh & Lermo, 1985). Due to the short distance from trench to shore in this area, about 80 km, this error is sufficient that earthquakes occurring offshore, with significant tsunamigenic potential, will appear as occurring inland, with capability of generating only a very small tsunami. This systematic difference in location also may affect seismotectonic studies based on global catalogs.

A possible explanation for the difference in location, put forward in the initial studies, is that waves traveling towards the northeast are speeded up on the ray segment going through the relatively fast downgoing plate. However, recent studies have shown that the subducting plate is nearly flat for a large distance from the trench (e.g. Suárez *et al*., 1990, Singh & Pardo 1993, Pérez-Campos *et al*., 2008, Husker & Davis 2009) along a large segment of the subduction zone, and therefore the near-vertical rays travel only a very short distance inside the plate.

Earthquakes breaking the Middle America Subduction Zone occur on the edge of the Pacific Ocean, a vast expanse in which there are relatively few seismic stations. This causes an uneven distribution in azimuths of stations recording earthquakes in this zone, with almost all seismometers situated on land areas towards the east and the north, and relatively few in the ocean to the west and to the south.

In this paper we repeat the studies from the 1980s, comparing the locations of earthquakes in modern global catalogs to those obtained from detailed studies of regional seismicity, and update the results and the interpretation.

Data

We use hypocenter locations from three catalogs; (1) From Pacheco & Singh, 2010 (which we will refer to as PS2010), (2) From the National Earthquake Information Center of the United States Geological Survey (NEIC of USGS), (3) From the Mexican National Seismological Service (spanish: Servicio Sismológico Nacional, referred to as SSN).

The PS2010 catalog was obtained by detailed analysis of earthquakes in the state of Guerrero. The earthquakes were relocated using data from permanent and portable broadband stations and accelerometers in the region, and only the best located events entered the catalog. Earthquakes were kept for which the hypocenter locations had an RMS error below 1 second and (except for a few moderate sized earthquakes at the edge of the state of Guerrero) where at least one digital station was at a distance less than the focal depth. The formal errors in location for these events are ~5 km or less. The 1D velocity model used for the locations is modified from Iglesias *et al*. (2001).

The second catalog is the global earthquake catalog of the National Earthquake Information Center (NEIC) of the United States Geological Survey (USGS). The earthquake hypocenters reported in this catalog are based on arrival times of phases observed at local to teleseismic distances, together with a 1D velocity model AK135 (Kenneth *et al*., 1995).

The third catalog is that of the SSN. This catalog includes earthquakes in Mexico and surrounding areas and uses phase arrival times recorded by the SSN network. The seismic network has a station density that varies significantly between different regions of the country and as a result the quality of the locations can vary significantly between them. In the densest part (in the state of Guerrero) the inter-station distance is on the order of 50 km, but it increases to several hundreds of kilometers in the northern part of the country. The velocity model used by the SSN for the locations is based on the Jeffreys & Bullen (1940) model, but has been modified in order to obtain smaller residuals in the locations.

Method

In this study we compare the locations of the global USGS catalog to two local catalogs; 1) PS2010 that contains only earthquakes in Guerrero and 2) SSN that contains earthquakes along the Mexican subduction zone from Jalisco to Chiapas. We are interested in the bias or systematic error in the locations, i.e. the average mislocation between the catalogs. This value can potentially be subtracted from the teleseismic location to get a very quick, "corrected estimate" of the hypocenter.

We calculate the difference in location between the two estimates as the vector **x** pointing from the location in the local catalog (PS2010 or SSN), towards the location in the global USGS catalog, $\mathbf{x_i}=(x_i,y_i)$ where x_i and y_i are the distance in kilometers along longitude and latitude respectively, for event i in the catalogs. To estimate the average error in location we calculate the vector sum of all the vectors, and dividing by the number of elements: $(x_{ave},y_{ave})=1/N \; Sum(\; (x_i,y_i))$. As the average is sometimes dominated by outliers, we also calculate the median difference as the vector $(x_{median},y_{median})= (median(x_i),median(y_i))$.

Results

Earthquakes in Guerrero

First we associate events in the PS2010 and USGS catalogs, by looking for the events in the USGS catalog that occur within 10 seconds of those in the PS2010 catalog. This did not lead to any erroneously associated events to earthquakes outside the study area. There are 8 earthquakes in the PS2010 catalog that are not in the USGS catalog (number 2, 5, 17, 18, 32, 45, 47, 127), that could not be associated. The unassociated events all have magnitudes M <= 4.2, and are not expected to necessarily be observed on a global scale. A total of 121 events are common to both catalogs. The earthquakes in the PS2010 catalog were divided into five groups by its authors, depending on their location and focal mechanisms; 1) shallow thrust events, 2) normal faulting and 3) steeply dipping thrust events in the down-going plate, 4) upper plate events and 5) unusual events, mostly strike slip in the upper plate. We compare the locations of the events in the different groups to those of the USGS. The differences in location between the two catalogs are shown as a vectors on a map (Figure 1) and on a polar plot (Figure 2) for the five types of events (Figures 1 and 2, a-e) and for all events together (Figures 1 and 2, f).

The hypocenter locations of the thrust events obtained by USGS are mostly towards the NE of the PS2010 locations, although there are also a few event locations in the opposite direction. The average difference in location is 12.5 km towards N72°E, and the median is 17.3 km towards N66°E. Events occurring under the coast have smaller differences in locations than those closer to the trench, but both in the same direction. This leads to a closer clustering in space of the USGS locations.

The normal faulting events have over all smaller errors than the thrust events, but they are all in the same direction, leading to an average that is larger than that of the thrust events, or: 25 km towards N57°E, and a median of 22 km towards N51°E.

The steeply dipping thrust events have a large scatter in location differences (some towards NE and others towards SW), leading to a small average error of 13 km towards N92°E and median of 7 km towards N85°E. There are errors of close to 40 km both in directions NE and SW. The events in the upper plate, all close to Acapulco, have errors smaller than 30 km. The unusual events also have a large scatter, with four events having differences in locations on the order of 10 km, whereas the other three all have errors of 32-55 km. All the average and median differences in locations are listed in Table 1.

Table 1. Average and median length and angle of vector pointing from USGS epicenter location toward PS2010 epicenter, for the different types of events defined in the PS2010 catalog.

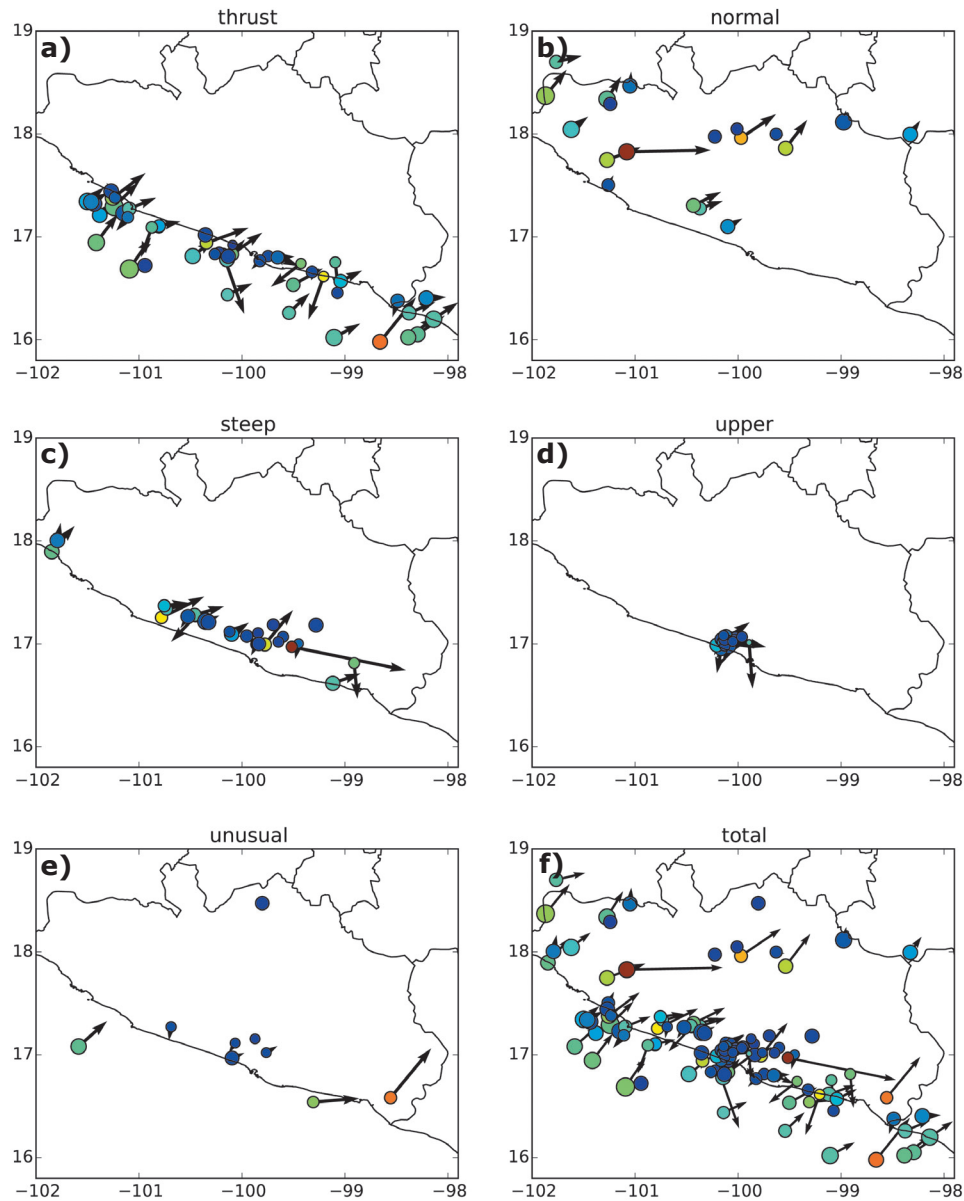| Event Type	Average Length [km]	Average Angle [NºE]	Median Length [km]	Median Angle [NºE]
Thrust	12.5	72.2	17.2	66.2
Normal	24.5	56.5	21.7	50.5
Steep Thrust	13.2	91.8	6.7	85.2
Upper Plate	6.7	143.3	5.8	149.0
Unusual	13.9	61.5	10.2	64.8
Total	12.8	75.0	11.2	67.4

Figure 1. Location difference between events in the PS2010 catalog and the USGS catalog, for 5 different types of earthquakes; a) shallow thrust events, b) normal faulting and c) steeply dipping thrust events in the downgoing plate, d) upper plate events and e) unusual events, mostly strike slip in the upper plate, as well as f) all events together. The arrow points from the PS2010 location to the USGS location. The color of the circle is proportional to the distance between the two locations (the length of the arrow) and the size of the circle is a function of the size of the event. (See Figure 2 for a definition of colores).

Table 2. Average and Median length and angle of vector pointing from USGS epicenter location toward SSN epicenter, for the different segments along the Mexican subduction zone.

Event Type	Average Length [km]	Average Angle [NºE]	Median Length [km]	Median Angle [NºE]
Jalisco-Colima	21.4	62.1	20.6	64.1
Michoacán	33.4	41.6	33.9	42.8
Guerrero	19.6	45.1	16.7	41.5
Oaxaca	27.3	44.4	27.4	55.6
Chiapas	30.8	66.4	31.2	69.3
Total	25.8	53.6	26.1	57.6

The total difference in locations is dominated by the shallowly dipping thrusts and the normal faulting events, as they are relatively more numerous, and shows a striking pattern principally towards the NE and to a lesser extent towards SW, with an average and median differences in location of 13 km towards N75°E and 11 km towards N67°E, respectively. We find that the scatter in location errors is much larger in the trench perpendicular direction, than the trench parallel direction, indicating that the locations are better determined in the latter than the previous.

Effect of magnitude

It is notable that for the thrust events in Figure 2, the error in location appears to be larger for the larger events. This is somewhat counter intuitive, as one would expect smaller events to be more to locate due to their lower signal to noise ratio, and therefore that the errors would be larger. Viewing the distance between the PS2010 and USGS epicenter locations as a function of magnitude (Figure 3), it is evident that the smaller events have a large scatter, ranging from 0-60 km, whereas for events larger than M~5.5 the distance is between 15 and 40 km, and for the three largest events, with 6.5 < M < 7.0, the distance is between 35 and 40 km.
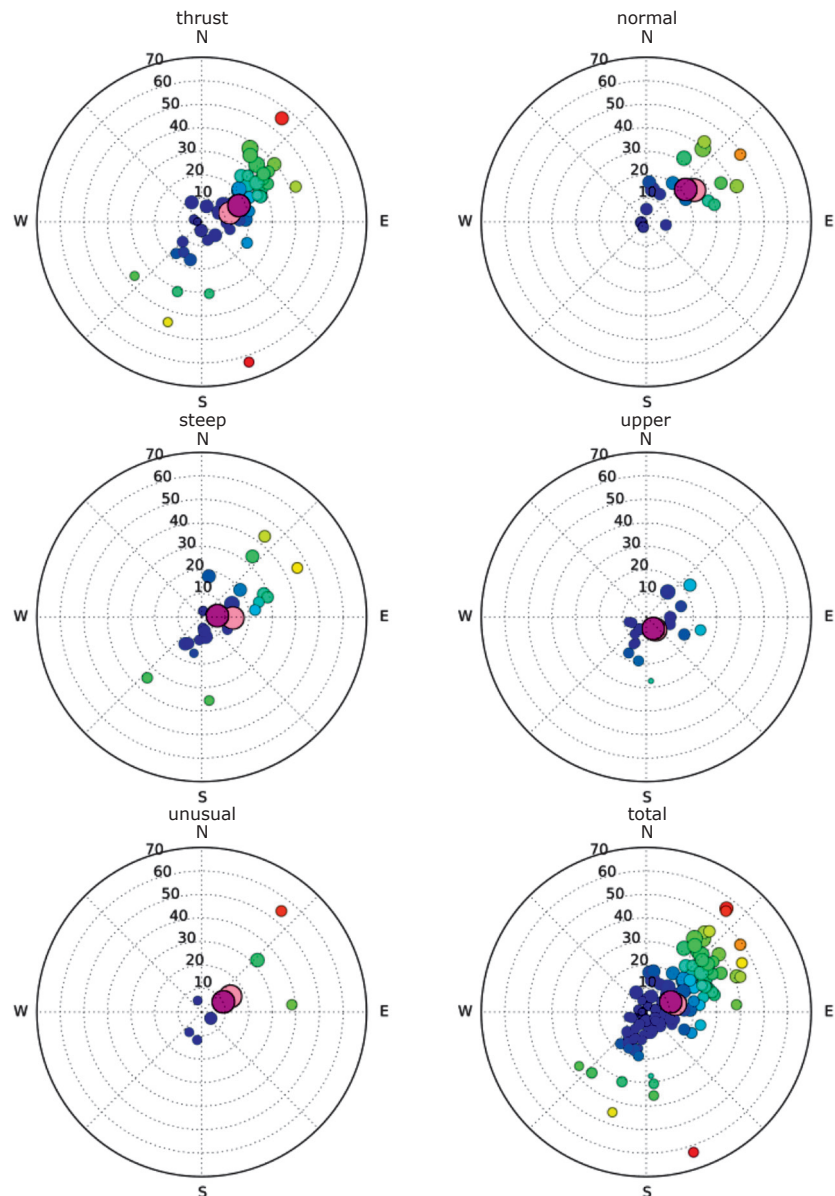

Figure 2. Distance and azimuth from the epicenter in the PS2010 catalog to the one in the USGS catalog, for earthquakes occurring in five different tectonic settings. The subplots, colors and sizes of circles are the same as in the previous figure, except the light pink large circle indicates the mean difference in location, and the large, dark pink circle shows the median difference in location.
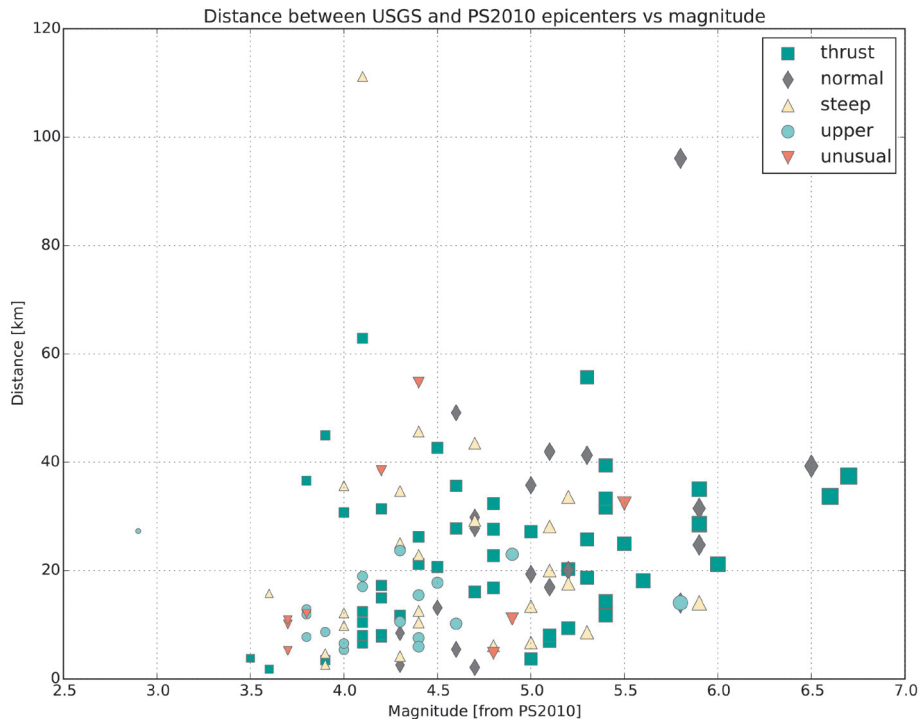
Figure 3. Distance between event location in the PS2010 catalog and the USGS catalog, for earthquakes occurring in five different tectonic settings, as a function of the magnitude of the event. Sizes of symbols represent the size of the event and colors refer to type of event.

Variations with time

It is plausible that the difference in epicenter locations between the PS2010 and USGS catalogs depend on the quantity and distribution of stations available at the time of the event, and as a consequence, could vary over time. We analyzed the difference in locations as a function of time. Although both the local SSN network in Mexico, as well as the global network have changed during this time, this does not seem to have affected the errors in locations, with the possible exception of the steeply dipping thrust events, of which several were detected during the MASE experiment carried out in the period 2005-2007 (Pérez-Campos *et al*., 2008), and all have small differences in locations.

Trade off between location and origin time differences

Due to the asymmetry in distribution of stations, there is a possibility for tradeoff between event location and origin time. We find that most events have differences in origin time between the USGS and PS2010 catalogs of -3 to 2 seconds (Figure 4), with a few exceptions, and for this group of events,

there is no strong correlation with difference in epicenter location. Of the 121 events, a total of 11 have timing errors of 2 seconds or more, and all of these have errors in location of 30 km or more. The events with relatively large origin time differences are mostly larger thrust events located closer to the trench, although there are three normal faulting events, and one of each of steeply dipping thrusts and unusual earthquakes in this group as well.

Earthquakes along the Mexican subduction zone

In the previous section we have seen how earthquake locations, as determined by a global network, are systematically offset from those determined by careful analysis of well-recorded earthquakes in Guerrero. The geometry of the subducting slab in Guerrero is unusual in the sense that once the slab gets to a depth of about 40 km, at a distance of 150 km from the trench, it flattens out, and remains so until reaching a distance of about 290 km from the trench (Pardo & Suarez, 1995; Pérez Campos *et al*., 2008; Husker & Davis, 2009). If we suppose that the difference in epicenter locations observed in this study is due to the downgoing rays interacting with the subducting
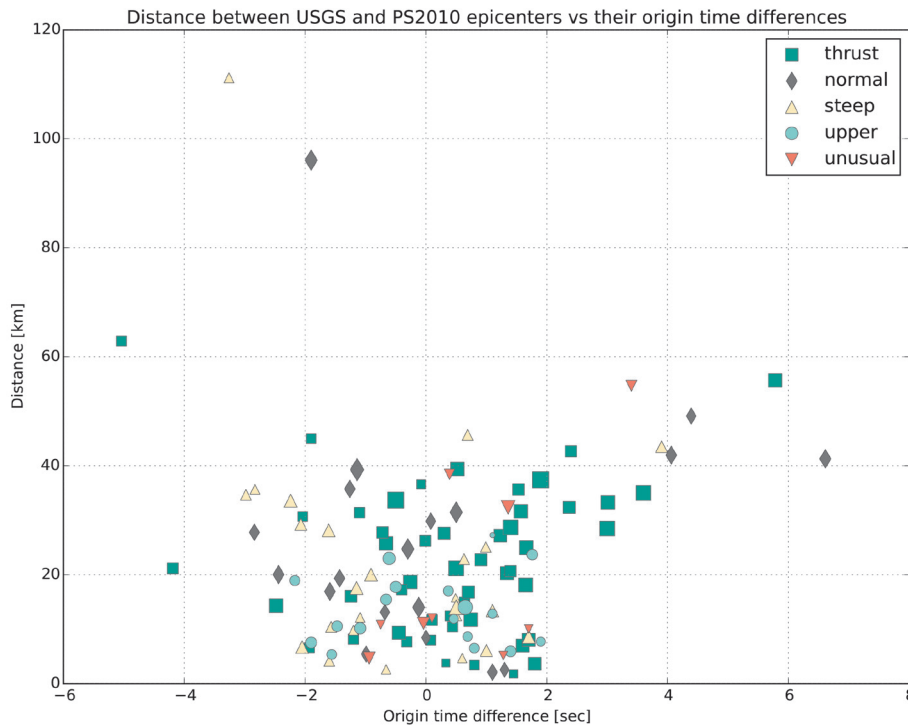
Figure 4. Distance between event location in the PS2010 catalog and the USGS catalog, for earthquakes occurring in five different tectonic settings, as a function of differences in hypocentral time. Sizes of symbols represent the size of the event and colors refer to type of event.

slab, we would expect that the difference in epicenter location would vary along the trench, reflecting the dip of the slab. A larger dip would lead to longer segments of the raypaths within the fast slab, and therefore larger travel time anomalies and consequently larger differences in epicenter locations between local and global data. In this section we look for such a variation.

We compare epicenter locations from the NEIC/USGS catalog used in the previous sections, to locations obtained using data from the local SSN network. Again we associate events in the two catalogs. In this case there are many events that are only in one catalog, and those are discarded. The associated catalog contains 6266 events, registered in the period between 2000 and 2014, of magnitudes ranging from 3.2 to 7.6. As we are mainly interested in the location differences for larger events in the subduction zone, we limit ourselves to the 272 events with M ≥ 5.0 and depths ≤ 40 km. It is to be kept in mind that for these two catalogs the interpretation of the difference in epicenter location is not as straight forward as for the previous two, given that in this case there may be significant errors in both locations. We divide

the subduction zone, from the west to east, in sections as determined by the states (joining the first two); Jalisco-Colima, Michoacán, Guerrero, Oaxaca and Chiapas.

As in the previous section, the differences in epicentral location between the two catalogs are shown as vectors on a map (Figure 5) and on a polar plot (Figure 6), now for the five different regions (Figures 5 and 6, a-e) and for the whole subduction zone (Figures 5 and 6, f). The differences in epicenter location between the two catalogs in Jalisco-Colima (Figure 5) show a very consistent pattern, with differences reaching values of up to 80 km, with a very consistent direction, slightly more eastward than seen for Guerrero in the previous section. The average difference is 21 km, at an angle of N62°E.

Offshore Michoacán the differences are larger, but have a smaller variability and are consistently towards the north-east, with an average difference of 33 km at an angle of N42°E. The USGS location is towards the shore of the SSN location for all events. Events closer to the trench have a larger difference in locations than events near the coast.
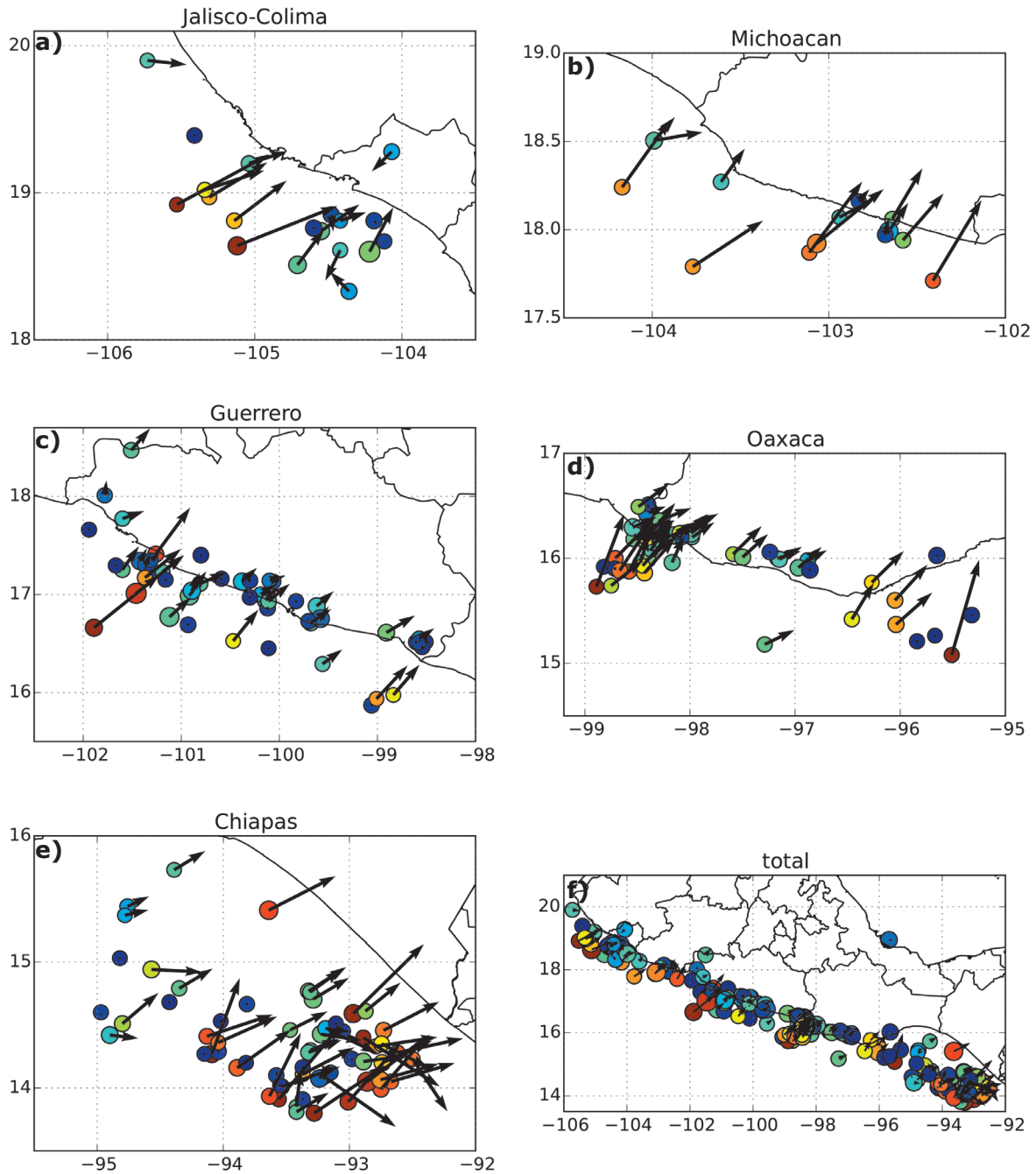
Figure 5. Location difference between events in the SSN catalog and the USGS catalog, for 5 different regions; a) Jalisco-Colima, b) Michoacán c) Guerrero, d) Oaxaca and e) Chiapas, as well as f) all events together. The arrow points from the SSN location to the USGS location. The color of the circle indicates the distance between the two locations and the size of the circle is proportional to the size of the event.

The pattern in Guerrero is similar to that of Michoacán, with a smaller average error, or 20 km towards N45°E. The largest error, of close to 80 km, is observed for an event very close to the trench, also studied in the previous section. The average error is substantially larger than obtained for the same region in the previous section.

Figure 6. Distance and azimuth from the epicenter in the SSN catalog to the one in the USGS catalog, for earthquakes occurring in five different regions. The subplots, colors and sizes of circles are the same as in the previous figure, except the light pink large circle indicates the mean difference in location, and the large, dark pink circle shows the median difference in location.
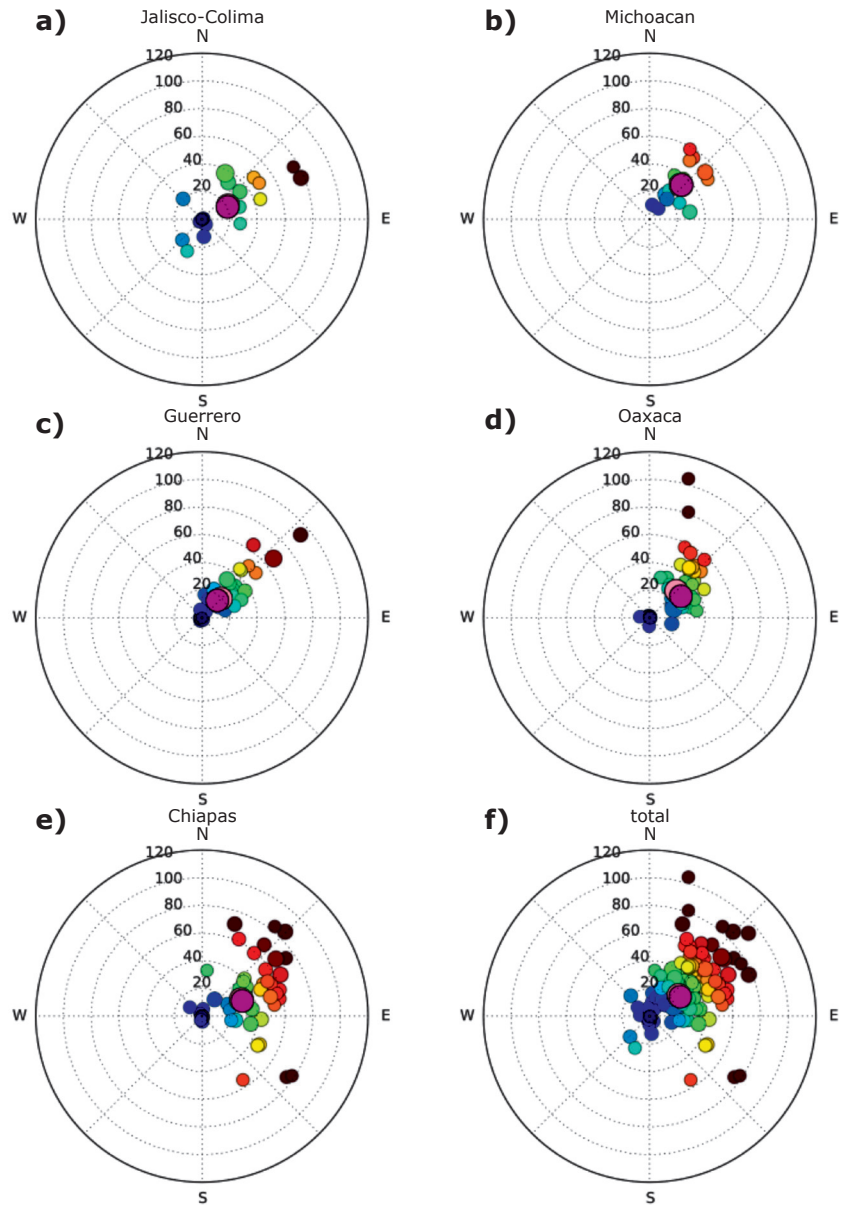
The earthquakes in Oaxaca split into three groups. The first group clusters around the rupture zone of the 2012 Ometepec-Pinotepa Nacional earthquake. There are a large number of events in this cluster, with similar differences in locations. As seen in other regions, the differences in locations for events closer to the trench are larger than those for events closer to the coast. In central Oaxaca there is a group of earthquakes, located just onshore, with smaller differences in locations. In eastern Oaxaca there are more events far offshore with a relatively indecisive pattern, with one earthquake with a difference in location of more than 100 km right next to earthquakes with differences smaller than 10 km. We reanalyzed

the very anomalous event, and confirmed that S-P time differences observed on the SSN network stations were consistent with the SSN location.

The events in Chiapas occur mostly in the aftershock zone of the 2012 Guatemala earthquake. These events have relatively large errors, with two dominant directions, towards NE and SE, overlapping. Here it is useful to keep in mind that these events are further from the core of the SSN network than other events in this study, and it is therefore probable that a substantial part of the differences in SSN locations and USGS locations for these events may be due to errors in the SSN location.

In summary, we find that there are differences in average mislocations for the various regions. The average errors are larger in Michocán, and smallest in Guerrero. However, we also notice that in Michoacán (Figure 5b), there are relatively more earthquakes closer to the trench, where we do see larger errors in the whole subduction zone, compared to the area closer to the coast where there is an abundance of earthquakes in Guerrero (Figure 5c). We therefore conclude that the bulk of the variation of the difference in location along the coast is not from interaction with the fast slab, but rather an effect of varying location perpendicular to the trench.

Effect of Magnitude

When comparing the USGS and PS2010 catalogs, we found that for events in Guerrero, the difference in epicenter location was larger for larger earthquakes. Analyzing the difference in location as a function of magnitude (Figure 7) between the USGS and SSN catalogs, we find that the trend is not as clear as was seen in the previous section. However, for events with M > 6.0, it is uncommon that the difference is smaller than ~20 km, and for about half those events, the difference is larger than ~40 km, again suggesting an increase in error with magnitude. It should also be mentioned, that when including the whole associated catalog, with events of magnitudes 3.2 to 7.6, the errors were not so systematic and average errors were on the order of 5 km. On the contrary, while analyzing the differences in locations from different agencies for events in the 70s and 80s Singh & Lermo, (1985), found that the difference does not increase with magnitude, rather the opposite. We attribute this change, from then to now, to the very different station coverage and data quality.

Differences in event time

For the events in Guerrero studied in the previous section, we found that there was a trade-off between the difference in epicenter location and the origin time difference between the two catalogs. For the events studied in this section, we find an even stronger pattern (Figure 8). In general, the difference in location is smallest for events with an USGS determined event time of 0-5 seconds later than the SSN event time. This is true for events in all regions, except for Chiapas, where there is a relatively larger scatter. A difference in time of 10 seconds is observed for the event in Oaxaca that has a difference in location of more than 100 km. Similarly to the previous section, we find that the events that have the largest

positive differences in time are on average closer to the trench.

Discussion

In the previous sections we observed that there is a systematic bias in hypocenter locations for events on the subduction interface in Mexico, with hypocenters obtained from teleseismic seismograms located 10-40 km towards the north-east from hypocenters from obtained from local seismograms. As this is true for both very well located earthquakes in Guerrero, as well as for events in the local SSN catalog located along the whole subduction zone from Jalisco to Chiapas, we deduce that the bulk of the difference comes from bias in the teleseismic locations, rather than the locations based on local data.

The SSN, PS2010 and USGS all use different 1D velocity models for locating the events. We suppose that the main source of error in location is that the 1D models used are not representative of the velocity along the trajectories between the events and the stations, and that the velocity may be different for the same event but different stations, due to lateral heterogeneities. Lateral heterogeneities that are of opposite sign in opposite directions have the largest effect on the locations.

There are two possible locations of the velocity anomalies that translate into travel time anomalies and therefore location errors; 1) near the source and 2) in the deep mantle along the trajectories of the rays. To discriminate between these two sources of error several observations are to be kept in mind. First, the errors are larger for shallow thrust events close to the trench. Second, the error is larger for larger events. Third, the station distribution is very uneven in azimuth, with most of the global network towards the north and east (in North-America, North-Asia and Europe), with few and noisy island stations towards the south and west. Fourth, the errors are consistent all along the trench, with large errors both where the slab is relatively steep (Jalisco, Chiapas) and where it is flat (Guerrero).

In order to investigate further the ray coverage for events of different sizes within the Mexican subduction zone used by the USGS for the event location determination, we show the ray coverage for four earthquakes of M 7.2, 6.4, 4.8 and 3.9 occurring in the western Guerrero region in April/May of 2014 (Figure 9). The color of the ray is determined by the residual ($t_{observed} - t_{predicted}$) for each path, where $t_{predicted}$ is the travel time calculated between
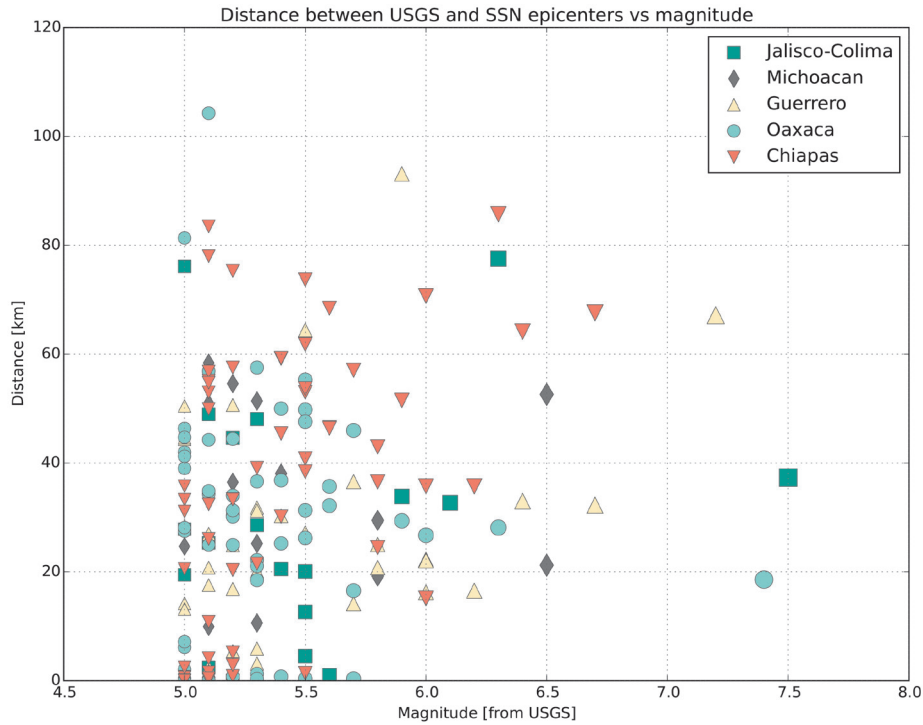
Figure 7 Distance between event location in the SSN catalog and the USGS catalog, for earthquakes occurring in five different regions, as a function of time of occurrence. Sizes of symbols represent the size of the event and colors refer to type of event.
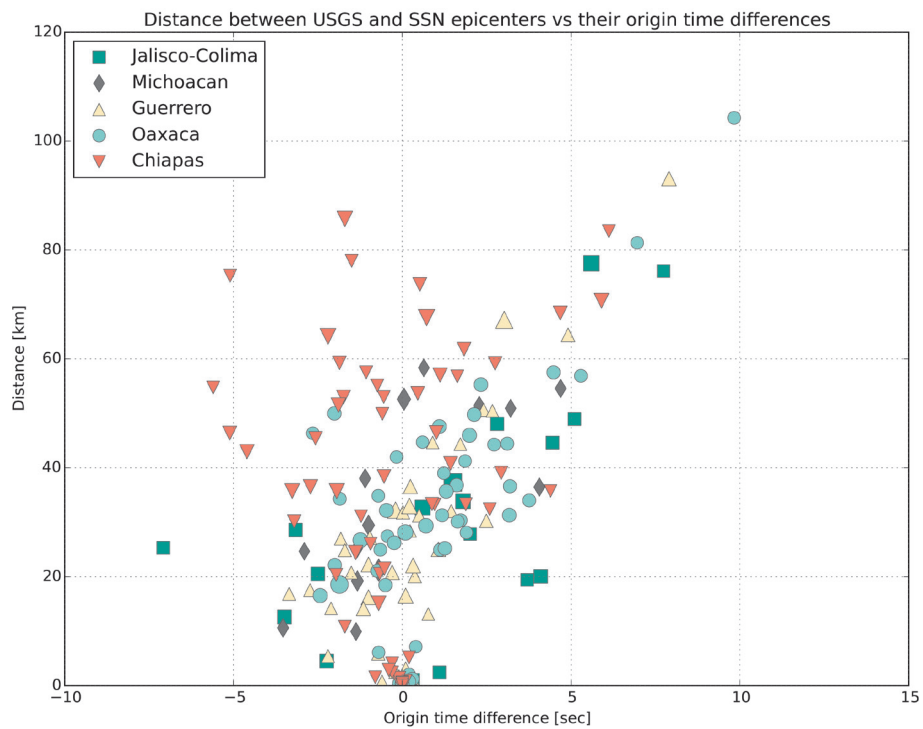

Figure 8. Distance between event location in the SSN catalog and the USGS catalog, for earthquakes occurring in five different regions, as a function of differences in hypocentral time. Sizes of symbols represent the size of the event and colors refer to type of event.

the USGS location and each station for a 1D Earth model.

The azimuthal coverage for the largest event is relatively even, and P-waves are reported on several stations in the Pacific Ocean, including Wake Island (WAKE), Fiji (MSVF) and two stations in Hawaii (KIP and POHA). Furthermore, PKP_{df} waves are reported on stations in Australia (COEN, WRAB, FORT and NWAO). The second largest event is observed at much more stations, or a total of 724 phases.

Of these, several (MLOD, HSSD, AIND, POHA, MLOA, HUAD, OPA, HON, KIP, KEKH and MSVF) are located in the Pacific Ocean. Core phases from 45 stations are used for the location. The two smallest events are not observed on any stations in the Pacific and have azimuth gaps of almost 200°. For all events we see slower than predicted (red) paths to the NW and SE, whereas paths to the NE and SW are faster (blue) or similar to predicted. However, the delays observed in opposite directions are generally similar.
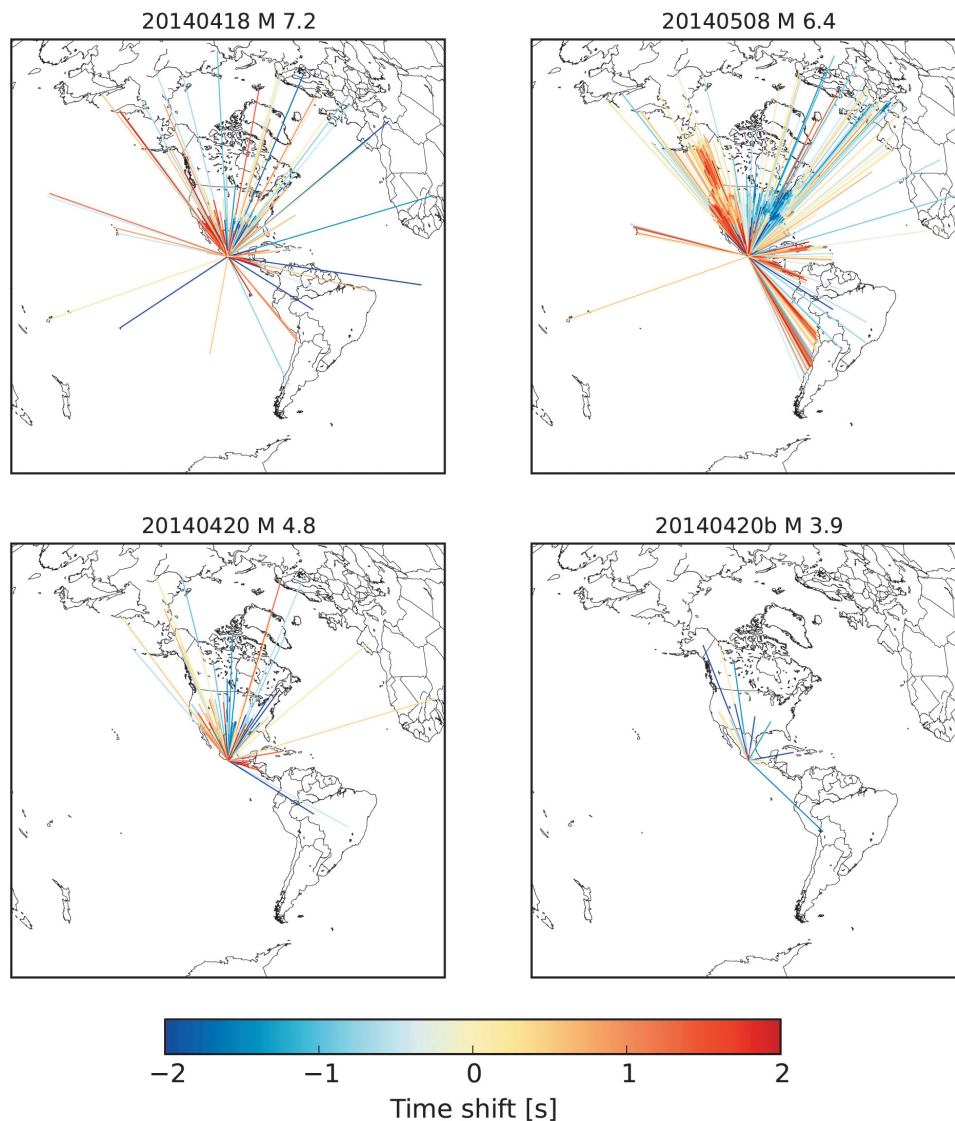

Figure 9. Delay times as reported by USGS/NEIC, for their best fit location. The four different events is the April 18th, 2014, 14:27:25, Papanoa earthquake, and three of its aftershocks; M 6.4, 2014-05-08, 17:00:15, M 4.8, 2014-04-20, 12:40:36, M 3.9 2014-04-20b, 07:42:49.

Residuals calculated for the SSN location (Figure 10) are very different. All the paths between NW and SE (going clockwise) are too fast, whereas paths going in the opposite directions are relatively slower. For the M 4.8 event, all the paths are too fast, but almost equally fast in all directions.

The length and angle (east of north) of the vector pointing from the SSN location towards the USGS locations of the four events, listed in order of magnitude, from largest to smallest, are; (67 km, N40°E), (33 km, N57°E), (15 km, N45°E) and (4 km, N180°E) respectively. The location reported by the SSN for the April 18th event is significantly different to that obtained from careful analysis of particle motion at several close stations, 17.375N, 101.055W (UNAM Seismolog Group , 2015). The USGS hypocenter is 9 km N74°E of this location. This event was particularly emergent, which may have caused different parts of the emergent P-wave to be picked at different stations, depending on their noise level, causing the mislocation.

In summary we find that as the duration of the event increases and as more distant stations, as well as stations in the Pacific are added, the difference in the location increases. For the 2014 Papanoa mainshock, the increased difference is a combination of; (1) an error in the SSN location, which is more difficult to estimate due to a lack of S-waves uncontaminated by late arriving P-waves, and (2) a bias due to the 3D structure along the rays.

Global tomography models (e.g. Kustowski *et al*., 2008) show that in the deep mantle there is a relatively fast zone towards the northeast of the study area, whereas there is a relatively slower zone (the Pacific superplume) towards the southwest. The interaction of rays with these zones would speed rays towards the northeast and slow rays towards the southwest. Consequently they would appear originating from a source further towards the northeast than the true location.

Conclusions

We have analyzed the differences in hypocenter locations of earthquakes in Mexico, between the USGS catalog which is principally based on globally observed travel times and two catalogs obtained from locally observed travel times; the PS2010 and SSN catalogs. The former contains 132 very well located earthquakes in the Guerrero segment of the subduction zone, and the latter is comprised of almost 40000 earthquakes in all of the Mexican territory, that

do not adhere to as strict criteria in quality of locations as the PS2010 catalog.

We find that the average distance from hypocenter locations of earthquakes larger than M 5 in the Mexican subduction zone in the global catalogs is 26 km towards N54°E of those in the local catalogs. We find that the magnitude and angle of the mislocation varies, by a small amount, along the coast. This value can be used for a very approximate correction of the USGS hypocenter, for early response purposes. The largest average errors of 33 km, are observed in Michoacán, and the smallest in Guerrero, where they are only 20 km on average. The average angle ranges from N42°E in Michoacán to N66°E in Chiapas.

The errors are found to be larger for shallowly dipping thrust events close to the trench, and smaller for steeply dipping thrust events, occurring inland. The errors are due to lateral variations in mantle structure that is asymmetric with respect to the Mexican subduction zone coastline. The errors seem to be exaggerated by using stations at large distances, and hence they may be larger for earthquakes of larger magnitudes.

Acknowledgements

References

Havskov J., Singh S.K., Nava E., Dominguez T., Rodriguez M., 1983, Playa Azul, Michoacán, Mexico earthquake of 25 October, 1981 (Ms = 7.3), *Bull. Seism. Soc.*, 73, 2, 449-458.

Husker A., Davis P.M., 2009, Tomography and thermal state of the Cocos plate subduction beneath Mexico City, *Journal of Geophysical Research*, 114, (B04306), doi:10.1029/2008JB006039.

Iglesias A., Cruz-Atienza V.M., Shapiro N.M., Singh S.K., Pacheco J.F., 2001, Crustal structure of south-central Mexico, estimated from the inversion of surface-wave dispersion curves using genetic and simulated annealing algorithms, *Geofísica Internacional*, 40, 3, 181-190.
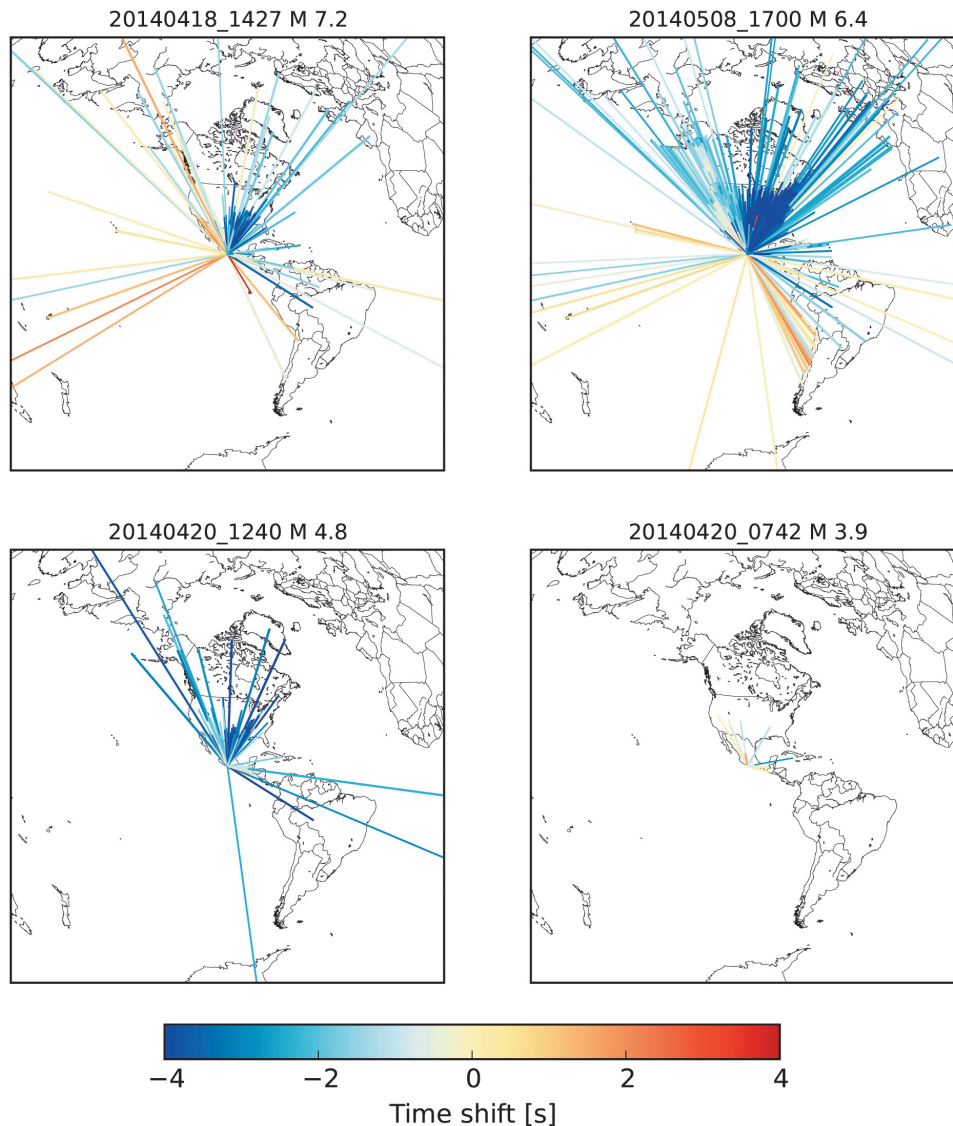
Figure 10. Same as Figure 9, except with delay times as would have been calculated by the USGS for the hypocenter reported by the SSN. Note that, the colorbar has a larger range.

Jeffreys H., Bullen K.E., 1940, Seismological Tables, British Association Seismological Committee, London.

Kennett B.L.N., Engdahl E.R., Buland R., 1995, Constraints on seismic velocities in the Earth from traveltimes, *Geophysical Journal International,* 122, 108-124, doi:10.1111/j.1365-246X.1995.tb03540.x

Kustowski B., Ekström G., Dziewoński A.M., 2008, Anisotropic shear-wave velocity structure of the Earth's mantle: A global model, *Journal of Geophysical Research*, 113, (B06306), doi:10.1029/2007JB005169.

Pacheco J., Singh S.K., 2010, Seismicity and state of stress in Guerrero segment of the Mexican subduction zone, *Journal of Geophysical Research,* 115, (B01301), doi:10.1029/2009JB006453.

Pardo M., Suárez G., 1995, Shape of the subducted Rivera and Cocos plates in southern Mexico: Seismic and tectonic implications. *Journal of Geophysical Research*, 100, (B7), 12.357-12373, doi:10.1029/95JB00919.

Pérez-Campos X., Kim Y., Husker A., Davis P., Clayton R., Iglesias A., Pacheco J.,

Singh S.K., Manea V., Gurnis M., 2008, Horizontal subduction and truncation of the Cocos Plate beneath central Mexico, *Geophysical Research Letters*, *35* (L18308), doi:10.1029/2008GL035127.

Singh S.K., Havskov J., McNally K., Ponce L., Hearn T., Vassiliou M., 1980, The Oaxaca, Mexico, earthquake of 29 November 1978: A preliminary report on aftershocks, *Science,* 207, (4436), 1211-1213, doi:10.1126/science.207.4436.1211.

Singh S.K., Lermo J., 1985, Mislocations of Mexican earthquakes as reported in international bulletins, *Geofísica Internacional*, 24, 2, 333-351.

Singh S.K., Pardo M., 1993, Geometry of the Benioff zone and state of stress in the overriding plate in Central Mexico, *Geophysical Research Letters*, 20, 14, 1483-1486, doi: 10.1029/93GL01310.

Suárez G., Monfret T., Wittlinger G., David C., 1990, Geometry of subduction and depth of the seismogenic zone in the Guerrero gap, Mexico, *Nature*, 345, 336-338, doi: 10.1038/345336a.

UNAM Seismology group, 2015, Papanoa, Mexico earthquake, of 18 April 2014 (Mw 7.2), *Geofísica Internacional*, 54, 4, 289-298